Synthesis and Characterisation of a Bifunctional Chelator for Gallium-68 Radiopharmaceuticals

A thesis submitted to the Faculty of Science, Monash University in partial fulfilment of the requirements for the degree of Bachelor of Science (Honours)

Patrick Robert William James Davey

School of Chemistry, Monash University

October 2018

Supervisor: Dr. Brett Paterson

Table of Contents

Acknowledgements

Firstly, to Dr. Brett Paterson: thank you for your insight and vision, and for granting me the freedom to make my own way this year. Your guidance, direction and unyielding support has been invaluable to me, and to this project.

To the technical staff downstairs, Dr. Boujemaa Moubaraki, Dr George Khairallah, Dr. Peter Nichols and Scott Blundell: thank you for your assistance and conversation. Thank you also to Dr. Craig Forsyth for collecting and solving X-ray crystal data. To other academic staff who have helped me through the years at Monash University, I owe you a great deal of gratitude and thanks as well.

To friends old and new: you have kept me on track and my head level for the bulk of this year and your humour and kindness is very much appreciated. Thank you to the other Honours students, especially Cormac, for your insight, humour and level-headedness.

To Mum and Heath: there were weeks without contact and I haven't seen you as much as I would have liked in the past nine months, but thank you for the long-distance, long-term support. I would not have made it here without you.

Lastly, to Cait and Sam: thank you for being my rocks this year. I am lucky to know you both and have felt so incredibly supported and loved throughout the ups, downs and in-betweens that this year has thrown at me. I love you both dearly.

Abbreviations

β^+	positron particle
β^-	beta electron
BFC	bifunctional chelator
Boc	*tert*-butoxycarbonyl
Boc-ON	2-(*tert*-butoxycarbonyloxyimino)-2-phenylacetonitrile
Cen	centroid
COSY	^{1}H-^{1}H correlated spectroscopy
cps	counts per second
CT	X-ray computed tomography
CTC	2-chlorotrityl chloride
d	doublet
DATA	(6-pentanoic acid)-6-(amino)methyl-1,4-diazepinetriacetate
DCC	*N,N'*-dicyclohexylcarbodiimide
DCM	dichloromethane
DCU	dicyclohexylurea
dd	doublet of doublets
DFO	desferrioxamine-B
diBocTACN	1,4,7-triazacyclononane-1,4-dicarboxylic acid di-*tert*-butyl ester
DIPEA	*N,N*-diisopropylethylamine
DMAP	4-dimethylaminopyridine
DMF	*N,N'*-dimethylformamide
DOTA	1,4,7,10-tetraazacyclododecane-1,4,7,10-tetraacetic acid
EC	electron capture
ESI	electrospray ionisation

FDG	fluorodeoxyglucose
HBED-CC	*N,N'*-bis-[2-hydroxy-5-(carboxyethyl)benzyl]ethylenediamine-*N,N'*-diacetic acid
HMBC	^{1}H-^{13}C heteronuclear multiple-bond correlation
HRMS	high resolution mass spectrometry
HSQC	^{1}H-^{13}C heteronuclear single quantum correlation
K_{sp}	solubility product constant
LRMS	low resolution mass spectrometry
m	multiplet
MRI	magnetic resonance imaging
MS	mass spectrometry
NOTA	1,4,7-triazacyclononane-1,4,7-triacetic acid
NOTP	1,4,7-triazacyclononane-1,4,7-tri(methylenephosphonic acid)
PCTA	3,6,9,15-tetraazabicyclo[9.3.1]pentadeca-1(15),11,13-triene-3,6,9,-triacetic acid
PET	positron emission tomography
pK_a	-log acid dissociation constant
ppm	parts per million
PSMA	prostate specific membrane antigen
RCY	radiochemical yield
RP-HPLC	reverse-phase high-performance liquid chromatography
s	singlet
S_N2	nucleophilic substitution (bimolecular)
SPECT	single-photon emission computed tomography
SPPS	solid-phase peptide synthesis
SPS	solid-phase synthesis

SSR	somatostatin receptor
t	triplet
$t_{1/2}$	half-life
TACN	1,4,7-triazacyclononane
TFA	trifluoroacetic acid
TIPS	triisopropylsilane
TLC	thin-layer chromatography
TMSBr	bromotrimethylsilane
TRAP	1,4,7-triazacyclononane-1,4,7-tri(methylenephosphinic acid)

List of Figures

List of Tables

List of Schemes

Abstract

Currently, ^{68}Ga-labeled 1,4,7,10-tetraazacyclododecane-tetraacetic acid (DOTA)-peptides are the most widely used class of ^{68}Ga radiotracers for PET, although DOTA is not optimal for ^{68}Ga complexation. The utility of the smaller 1,4,7-triazacyclononane-based chelators (e.g. tri-acetic acid NOTA, tri-phosphonic acid NOTP and tri-phosphinic acid TRAP) for Ga^{3+} has been known for some time, with bifunctional derivatives forming Ga^{3+} complexes with higher kinetic stability and higher radiochemical yields than DOTA-based systems. The synthesis of NOTA, TRAP, NOTP and similar chelators has been shown to work using solid-phase techniques, which seeks to minimise the disadvantages present in solution-based chemistry. Herein, the development of two approaches for the synthesis of **H_3L^1**, a macrocyclic bifunctional chelator bearing phosphonic and carboxylic acid pendant arms, is described: one in solution and one using solid-phase synthesis.

In solution, the syntheses of several intermediate species were successfully completed. Characterisation was primarily undertaken using ^{1}H, ^{13}C{^{1}H}, ^{19}F{^{1}H} and 2D (COSY, HSQC and HMBC) nuclear magnetic resonance spectroscopy and mass spectrometry. Good to high yields were obtained for the majority of reactions. The di-ethyl phosphonate intermediate was the successfully synthesised in solution, however there were issues with selectivity using solid-phase synthesis. A mixture of the mono- and di-substituted species was present after several synthetic modifications. The X-ray crystal structure of the neutral, distorted octahedral complex [Ga(NOTP)] is also reported. The complex was formed under ambient conditions in water. NOTP coordinates to the metal through the three nitrogen atoms of the macrocycle and three deprotonated phosphonate OH groups. Two discrete enantiomers, Δλλλ-SSS and Λδδδ-RRR, are present as a racemate in the unit cell. A high radiochemical yield (>95%) and an apparent molar activity of 0.5 MBq/nmol was obtained for [^{68}Ga][Ga(NOTP]], as determined by radio-HPLC.

1 Introduction and Background

1.1 Metals in Medicinal Inorganic Chemistry

Metal ions are required for many critical functions in humans. Four main group (Na, K, Mg, and Ca) and ten transition (V, Cr, Mn, Fe, Co, Ni, Cu, Zn, Mo, and Cd) metals are currently known to be required for normal biological functioning in humans.[1] A lack of key metal ions can lead to disease. Well-known examples include anaemia arising from iron deficiency, heart disease in infants owing to copper deficiency, and growth retardation caused by a lack of zinc.[2] Metals have played a role in medicine for centuries. Medicinal inorganic chemistry is a relatively recent derivative of bioinorganic chemistry, located at the interface between inorganic chemistry and medicine. Among other topics, medicinal inorganic chemistry encompasses chelation therapy, enzyme inhibition, metal sequestration, metal-based drugs, and diagnostic and therapeutic radiopharmaceuticals.[3] The origins of the field can be traced back to the development of the platinum-based anticancer drug, Cisplatin, in the 1960s by Rosenberg and co-workers.[4] Since then, the field has expanded exponentially, exemplified by the number of comprehensive reviews and books that have been published in the area, as well as the number of metal compounds and complexes in clinical use (**Table 1.1**).[5]

Table 1.1: Examples of metal complexes and compounds in clinical use (adapted from Ronconi *et al.*).[6]

Compound (brand name)	Function
Active complexes	
cis-$[PtCl_2(NH_3)_2]$ (Cisplatin)	Anticancer
$[Gd(DTPA)(H_2O)]^{2-}$ (Magnevist)	Extracellular contrast agent for MRI
$[^{99m}Tc][Tc(CNCH_2C(CH_3)_2OCH_3)_6]^+$ (Cardiolite)	Myocardial imaging
Cyanocobalamin (Co^{3+}; vitamin B_{12})	Coenzyme
Active metals	
Li_2CO_3	Prophylaxis for bipolar disorders
$La_2(CO_3)_3$ (Foznol)	Chronic renal failure
Bi^{3+} citrate (De-Nol)	Antibacterial, antiulcer
$CaCO_3$	Antacid
$Na_2[Fe^{2+}(CN)_5(NO)]\cdot 2H_2O$ (Nipride)	Hypotensive
p-xylyl-bicyclam·8HCl (AMD3100)	Anti-HIV

The popularity of metal radioisotopes and complexes in nuclear medicine has also greatly contributed to this growth. For example, technetium(I) sestamibi (brand name Cardiolite), is used in nuclear imaging to image heart muscle (**Figure 1.1**).[7] In biological systems, metal cations are complexed to biomolecules and play diverse roles in biological processes: as electron carriers, catalytic groups at the active site of enzymes, stabilisers of the tertiary structure of polynucleotides and proteins, and oxygen carriers.[8]

a) b)

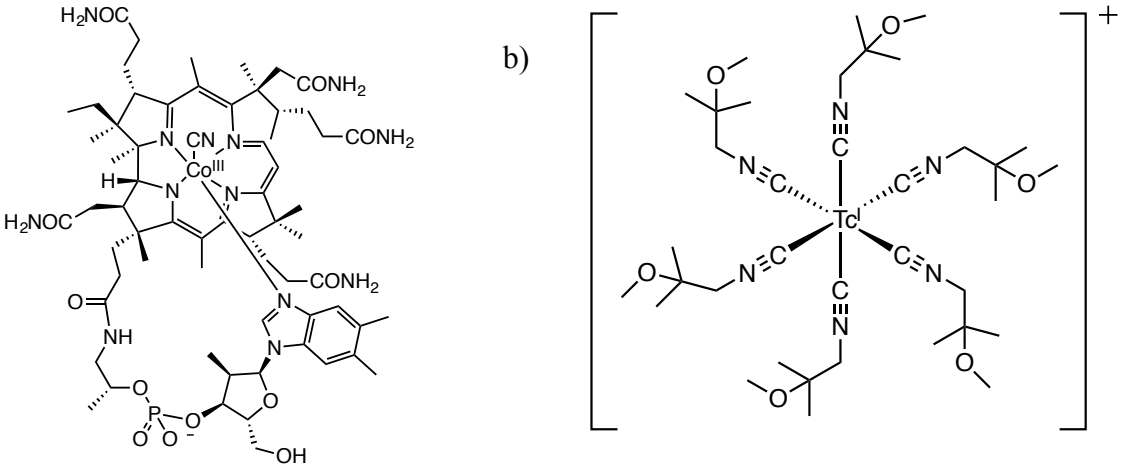

Figure 1.1: Biologically relevant coordination complexes a) the synthetically produced form of Vitamin B_{12}, cyanocobalamin, incorporating Co^{3+} and b) Cardiolite, a technetium(I) complex used to image the myocardium (heart muscle).

Coordination complexes are comprised of an electron-deficient metal cation and neutral or anionic ligands. The field of medicinal inorganic chemistry utilises the principles of coordination chemistry and complex formation to design metal-based compounds that exhibit biological effects. Metal ions may be introduced into biological systems either for therapeutic benefit or as diagnostic aids. The biological effects of metal-based pharmaceuticals can be modulated by varying the ligands and coordination environment around the metal. Apart from serving the traditional roles of modifying metal reactivity, thermodynamic stability and kinetic inertness of the resulting complexes, ligands can alter the bioavailability of metal ions, can protect tissues and organ systems from toxic metal ions, or can assist in targeting specific sites for diagnosis and therapy in, for example, nuclear medicine applications.[9]

1.2 Radiometals and Nuclear Medicine

Nuclear medicine is the branch of medicine that deals with the use of radioactive substances, called radiopharmaceuticals, in the diagnosis and treatment of disease. Radioactive isotopes that can be utilised for these purposes are shown in **Figure 1.2**.[10] Therapeutic nuclear medicine makes use of radioisotopes that emit high energy ionising radiation, such as α particles, Auger electrons, and β electrons (β^-) near sites of diseased tissue or tumours *in vivo*.[11] Diagnostic nuclear imaging is the process by which γ radiation is used to construct a projection of radioisotope intensity showing the areas of radioisotope accumulation within the body following detection by an external scanner. Nuclear medicine imaging usually provides information on functional processes, which can be complementary to the anatomical imaging provided by X-ray computed tomography (CT) or magnetic resonance imaging (MRI).[12]

1	2	3	4	5	6	7	8	9	10	11	12	13	14	15	16	17	18
1 H																	2 He
3 Li	4 Be											5 B	6 C β^+	7 N β^+	8 O β^+	9 F β^+	10 Ne
11 Na	12 Mg											13 Al	14 Si	15 P T	16 S	17 Cl	18 Ar
19 K	20 Ca	21 Sc β^+T	22 Ti	23 V	24 Cr	25 Mn β^+	26 Fe β^+	27 Co β^+	28 Ni β^+	29 Cu β^+T	30 Zn	31 Ga γβ^+T	32 Ge	33 As β^+	34 Se γ	35 Br β^+T	36 Kr γ
37 Rb β^+	38 Sr β^+T	39 Y β^+T	40 Zr β^+	41 Nb β^+	42 Mo	43 Tc γβ^+	44 Ru γ	45 Rh T	46 Pd	47 Ag T	48 Cd	49 In γ	50 Sn T	51 Sb	52 Te	53 I γβ^+T	54 Xe γ
55 Cs	56 Ba	57 La	72 Hf	73 Ta γ	74 W	75 Re T	76 Os	77 Ir	78 Pt γT	79 Au T	80 Hg T	81 Tl γ	82 Pb T	83 Bi T	84 Po	85 At T	86 Rn
87 Fr	88 Ra T	89 Ac T															

		58 Ce	59 Pr	60 Nd	61 Pm	62 Sm T	63 Eu	64 Gd	65 Tb T	66 Dy	67 Ho T	68 Er	69 Tm	70 Yb	71 Lu T		
		90 Th T	91 Pa	92 U	93 Np	94 Pu	95 Am	96 Cm	97 Bk	98 Cf	99 Es	100 Fm	101 Md	102 No	103 Lr		

Figure 1.2: Periodic table highlighting (shaded) elements with use or potential use as diagnostic and/or therapeutic radioisotopes in nuclear medicine. Main uses identified by: γ (SPECT), β^+ (PET) and T (therapy using β^-, α or Auger electron-emitting radioisotopes) (adapted from Blower).[10]

1.2.1 Single-Photon Emission Computed Tomography and Positron Emission Tomography

The non-invasive molecular imaging techniques, positron emission tomography (PET) and single-photon emission computed tomography (SPECT), utilise radioisotopes to image disease states *in vivo*. PET radiotracers emit γ radiation indirectly. As the radioisotope decays, positrons (β^+) are emitted, which annihilate with electrons up to a few millimetres away from the site of emission, causing two γ photons to be emitted 180° from one another.[13] SPECT radiotracers, in contrast, emit γ radiation directly.[12] SPECT imaging has historically been the more widely used imaging technique, mostly due to the availability of the ^{99m}Tc radioisotope (half-life ($t_{1/2}$) = 6 h) from the ^{99}Mo/^{99m}Tc generator, available to hospitals and pathology centres globally.[7] SPECT is by far the cheaper technique, with overall lower costs and longer-lived radioisotopes. However PET offers higher resolution and sensitivity, which means that the images generated are of a higher quality and clinicians can gain a more accurate understanding of the disease state they are imaging.[14]

The availability of PET has historically been limited because of the need for cyclotron-produced radioisotopes such as ^{18}F for use in imaging agents, for example [^{18}F]fluorodeoxyglucose ([^{18}F]FDG) (**Figure 1.3**).[15] [^{18}F]-FDG is a glucose analogue and contains a covalent ^{18}F-C bond in its structure, which allows for imaging of sites where there is an abnormally high sugar uptake (e.g. in tumour cells and associated metastases) in the body. PET scans are increasingly combined with anatomical imaging techniques such as CT and MRI to correlate functional data with anatomical information.

a)

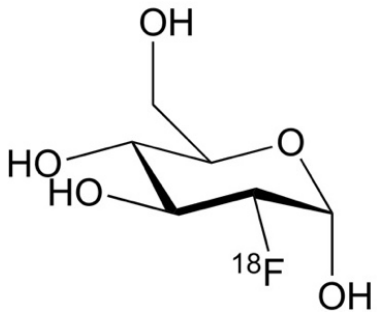

b)

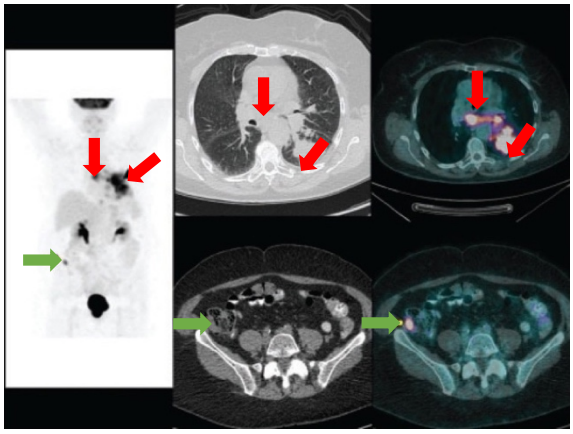

Figure 1.3: PET scans utilise [^{18}F]FDG to image malignancies. a) [^{18}F]FDG b) A 73-year-old woman with non-small cell lung carcinoma. PET maximum intensity projection (MIP) image (left panel), CT images (middle panels) and combined images (right panels), highlighting the primary tumour (green arrow) and metastases (red arrows). Adapted from Almuhaideb *et al.*[16]

The relatively high cost of running and maintaining cyclotron facilities, however, necessitated a move towards generator-based radioisotope production methods. Additionally, the success of the ^{99}Mo/^{99m}Tc generator for SPECT imaging spurred interest in the development of generator-produced radioisotopes suitable for PET. Compared to cyclotrons, generators do not require: special premises with large radiation shielding equipment; highly qualified personnel for the maintenance of specialised equipment and; a large consumption of energy. Generator-produced radioisotopes such as ^{68}Ga have become a viable alternative to their cyclotron-produced analogues, such as ^{18}F, for PET imaging.

1.3 Gallium Radiopharmaceuticals for PET Imaging

1.3.1 Radioisotopes of Gallium and ^{68}Ga Production

Currently, 30 different isotopes of gallium are known, of which several are radioactive (**Table 1.2**).[9] ^{66}Ga and ^{67}Ga are cyclotron produced, and ^{67}Ga has been used historically in SPECT imaging. ^{68}Ga is a positron emitter with a half-life of 68 min. ^{68}Ga is produced by the ^{68}Ge/^{68}Ga generator, which can be stored on-site in hospitals.[17] A generator is a self-contained system housing a parent/daughter radioisotope mixture. In the ^{68}Ge/^{68}Ga generator, ^{68}Ge is

immobilised on a column filled with inorganic, organic or mixed matrices where it spontaneously decays to ^{68}Ga. Most ^{68}Ge/^{68}Ga generators use acidic eluent (e.g. 0.1 M HCl) to elute either [^{68}Ga]$GaCl_3$, [^{68}Ga][$GaCl_4$]$^-$ or [^{68}Ga][$Ga(OH_2)_6$]$^{3+}$.[18] The long half-life of the ^{68}Ge parent ($t_{1/2}$ = 270.95 d) means that a generator has a working life of up to one year depending on the initial activity (*cf.* 14 d for the ^{99}Mo/^{99m}Tc generator).[19]

Table 1.2: Decay properties of three gallium radioisotopes. EC = electron capture.

Isotope	$t_{1/2}$	Decay mode	E (keV)	Production method
^{66}Ga	9.5 h	β^+ (56 %) EC (44 %)	β^+, 4150, 935	Cyclotron, ^{63}Cu(α,n)^{66}Ga
^{67}Ga	78.2 h	EC (100 %)	γ, 93, 184, 300	Cyclotron, ^{68}Zn(p,2n)^{67}Ga
^{68}Ga	68 min	β^+ (90 %) EC (10 %)	β^+, 1880	^{68}Ge/^{68}Ga generator

^{68}Ga decays to the stable isotope ^{68}Zn *via* β^+ emission and electron capture (EC) (**Figure 1.4**). The useful 68 min half-life allows patients to be scanned in clinics quickly, minimising wait times and radiation exposure to both patients and personnel. ^{68}Ga also allows for repetitive examinations due to the relatively low radiation exposure.[17] ^{68}Ga has a maximum β^+ energy of 1880 keV, an average β^+ energy of 890 keV and annihilation radiation of 511 keV.[17] This provides an adequate level of radioactivity for high resolution PET images.

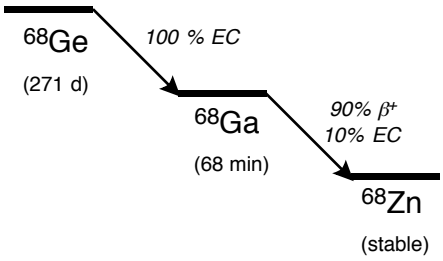

Figure 1.4: Decay scheme for ^{68}Ga from its parent isotope ^{68}Ge to the stable daughter isotope ^{68}Zn.

1.3.2 Gallium Chemistry

Gallium is a semi-metallic group 13 element. The chemistry of gallium in physiological systems is dominated by its trivalent oxidation state, Ga^{3+}. Lower oxidation states of gallium are known

but are generally unstable in water.[20] With its high charge and small ionic radius (0.62 Å), Ga^{3+} is classified as a hard Lewis acid. Due to this, Ga^{3+} will generally coordinate preferentially to hard Lewis bases, such as nitrogen and oxygen donor atoms. In aqueous solutions, the 'free ion' is octahedrally coordinated to six water molecules, forming $[Ga(OH_2)_6]^{3+}$. Ga^{3+} is readily hydrolysed at pH >3 forming insoluble $Ga(OH)_3$. Radiolabelling at pH values of between 3 and 7 is difficult due to the low solubility of the $Ga(OH)_3$ precipitate (K_{sp} = 7.28 x 10^{-36}).[21] The precipitate is amphoteric, meaning that it will re-dissolve at pH >7 forming $[Ga(OH)_4]^-$.[22] The solution and coordination chemistries of Ga^{3+} are somewhat similar to Al^{3+} and In^{3+}, and are very similar to high-spin Fe^{3+} (**Table 1.3**).[7] With similar electronegativites, ionisation potentials and electron affinities, gallium is expected to follow many of the same chemical pathways as Fe^{3+} in the body.

Table 1.3. Chemical parameters for Ga^{3+}, high-spin Fe^{3+}, Al^{3+} and In^{3+}.

Parameter, *units*	Ga^{3+}	Fe^{3+} HS	Al^{3+}	In^{3+}
Ionic radius (octahedral), *Å*[23]	0.62	0.65	0.54	0.80
Ionic radius (tetrahedral), *Å*[23]	0.47	0.49	0.39	0.62
Ionisation potential (4th), *eV*[24]	64	55	120	54
Electron affinity (3rd ionisation potential), *eV*[24]	30.71	30.65	28.45	28.03
Absolute hardness (Pearson), *eV*[24]	17	12.08	45.77	13
Electronegativity (Pauling), *Pauling units*[25]	1.81	1.83	1.61	1.78
Metal-oxygen bond dissociation energy, *kJ mol*$^{-1}$[26]	353.5	390.4	511	320.1
1st metal-hydroxide formation constant, *log* K_1[27]	11.4	11.81	9.01	10.0

Indeed, the biochemical chelation and protein binding similarities between Ga^{3+} and high-spin Fe^{3+} are likely causative of physiological Ga^{3+} activity. Tissue distribution studies have shown that the majority of unbound, administered Ga^{3+} binds to iron-transporting proteins such as transferrin, lactoferrin and ferritin.[28] However, differences in reduction potential (unlike Fe^{3+}, Ga^{3+} will not be reduced under physiological conditions) mean that Ga^{3+} does not compete with Fe^{2+} containing molecules, such as heme, in the body.[26]

1.3.3 ^{68}Ga Radiopharmaceuticals

To apply metallic radioisotopes to specific biological applications, ligands are used to influence the biodistribution and pharmacokinetics *in vivo*. In addition, chelators can be used that form complexes with high thermodynamic and kinetic stability to avoid transmetallation and hydrolysis of the radiometal. Chelators can also be covalently linked to a targeting vector biomolecule, such as a peptide or antibody, to improve selectivity to disease states *in vivo*. Two examples of successfully applied ^{68}Ga radiopharmaceuticals used in PET imaging for the diagnosis of disease are [^{68}Ga]Ga-DOTA-TATE (neuroendocrine cancers)[14] and [^{68}Ga]Ga-HBED-CC-PSMA (prostate cancers) (**Figure 1.5**).[29] [^{68}Ga]Ga-DOTA-TATE is comprised of a macrocyclic chelator, DOTA (1,4,7,10-tetraazacyclododecane-*N*,*N'*,*N''*,*N'''*-tetraacetic acid), covalently linked to an eight amino acid peptide octreotate. Octreotate is a somatostatin analogue, which targets and binds to somatostatin receptors (SSRs).[30] SSRs are well-known to be over-expressed in neuroendocrine tumours, which allows [^{68}Ga]Ga-DOTA-TATE to image these malignancies *via* PET imaging.

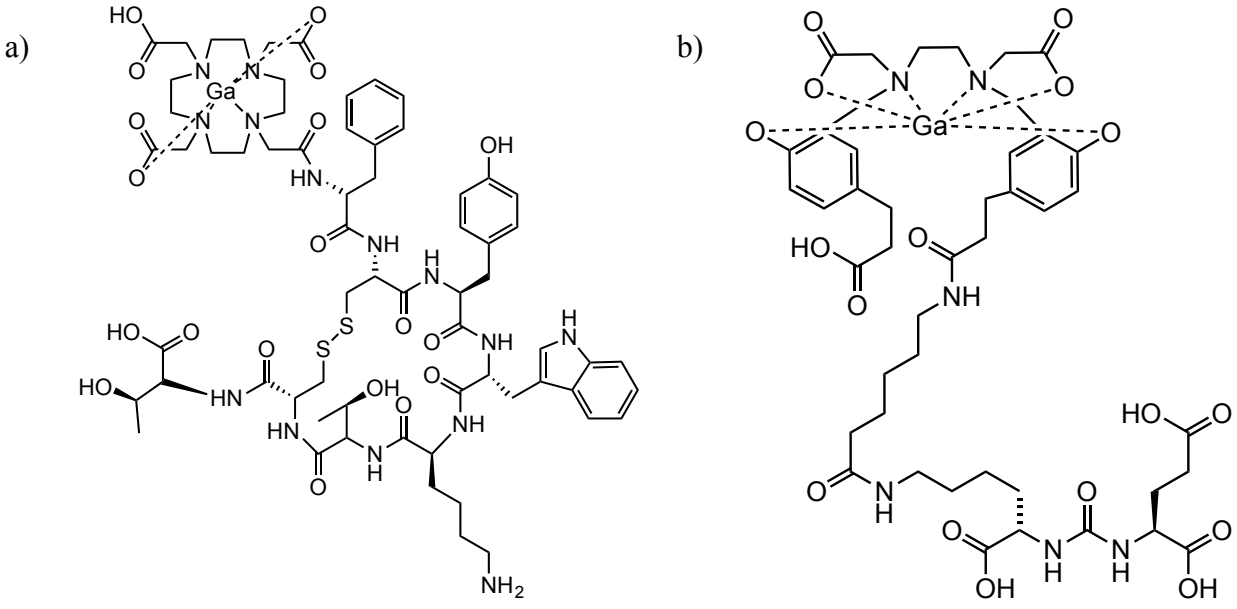

Figure 1.5: Clinically used ^{68}Ga Radiopharmaceuticals. a) [^{68}Ga]Ga-DOTA-TATE and b) [^{68}Ga]Ga-HBED-CC-PSMA.

DOTA is a tetraazamacrocyclic chelator providing a N_4O_2 coordination environment for the Ga^{3+} ion. [^{68}Ga]Ga-HBED-CC-PSMA is comprised of the acyclic chelator, HBED-CC (*N,N'*-bis-[2-hydroxy-5-(carboxyethyl)benzyl]ethylenediamine-*N,N*'-diacetic acid), and the prostate-specific membrane antigen (PSMA) inhibitor Glu-urea-Lys. PSMA is a membrane-type zinc protease expressed by nearly all prostate cancers, which Glu-urea-Lys can selectively target. This allows [^{68}Ga]Ga-HBED-CC-PSMA to image prostate tumours using PET.[29]

Although these radiopharmaceuticals are currently very successful clinically, their syntheses do have drawbacks. The synthesis of [^{68}Ga]Ga-DOTA-TATE requires heating to between 80 – 100 °C to overcome the high energy of activation barrier and to ensure adequate chelation of Ga^{3+} within the timeframe allowed by the relatively short half-life of 68 min.[31] At room temperature, the synthesis of [^{68}Ga]Ga-HBED-CC-PSMA produces multiple geometric isomers (in addition to the optical isomers) of the [^{68}Ga]Ga-HBED-CC complex.[29] Heating the reaction favours formation of the thermodynamically preferred species. Speciation of HBED-CC complexes has been postulated to be caused by the rapid association/dissociation of the phenolic oxygen ligands.[32]

Clinical radiosyntheses of both radiopharmaceuticals takes 5 – 20 min at pH 3 – 5, followed by post-synthetic purification and work-up to remove impurities and unreacted ^{68}Ga.[33] These reaction conditions are not ideal for the development of novel ^{68}Ga radiopharmaceuticals. They add process complexity, limit molar activity (the measured radioactivity per gram of radiopharmaceutical), and the heat and low pH may damage the vector biomolecule. The ideal synthesis should be a one-step procedure, matching the simplicity of the long-established ^{99m}Tc radiolabelling protocols.[33] Low chelator concentrations are required, so as to avoid saturating receptors of interest with non-radioactive substances and the disruption of normal physiological processes. Additionally, the radiolabelling of the chelator

should reach completion (>95 %) at room temperature and neutral pH quickly (<5 min).[32] An investigation into new chelators that can quantitatively coordinate $^{68}Ga^{3+}$ at room temperature, near neutral pH and low concentration of the ligand is therefore warranted.

1.4 Ga^{3+} Chelators

Over the past two decades, several chelators have been developed in an attempt to circumvent the limitations of both DOTA and HBED in biomolecule radiolabelling.[32, 34] These include both macrocyclic and acyclic chelators. Chelators that have been investigated include those derived from triazamacrocycles (e.g. 1,4,7-triazacyclononane-1,4,7-acetic acid, NOTA),[35] pyridyl-substituted DOTA tetraazamacrocycles (e.g. PCTA),[36] the acyclic siderophore desferrioxamine-B (DFO),[37] a substituted pyridine carboxylate-based acyclic chelator (DEDPA),[38] 6-amino-1,4-diazepanes with *N*-substituted acetates (e.g. DATA),[39] and 1,4,7-triazacyclononane (TACN) chelators incorporating phosphonic (NOTP) and phosphinic (TRAP) functional groups (**Figure 1.6**).[40]

Interest in TACN-based chelators has been spurred on by the particularly attractive coordination properties TACN derivatives possess for Ga^{3+} complexation. They form highly thermodynamically stable complexes with Ga^{3+} that are kinetically inert and rigid, due to the hard donor atoms often employed (O and N) and the pre-formed geometries imparted by the chelators.[41] Additionally, the radiolabelling properties of these chelators with $^{68}Ga^{3+}$ can be adjusted by modifying the substituent pendant functional groups attached to the TACN core.[42]

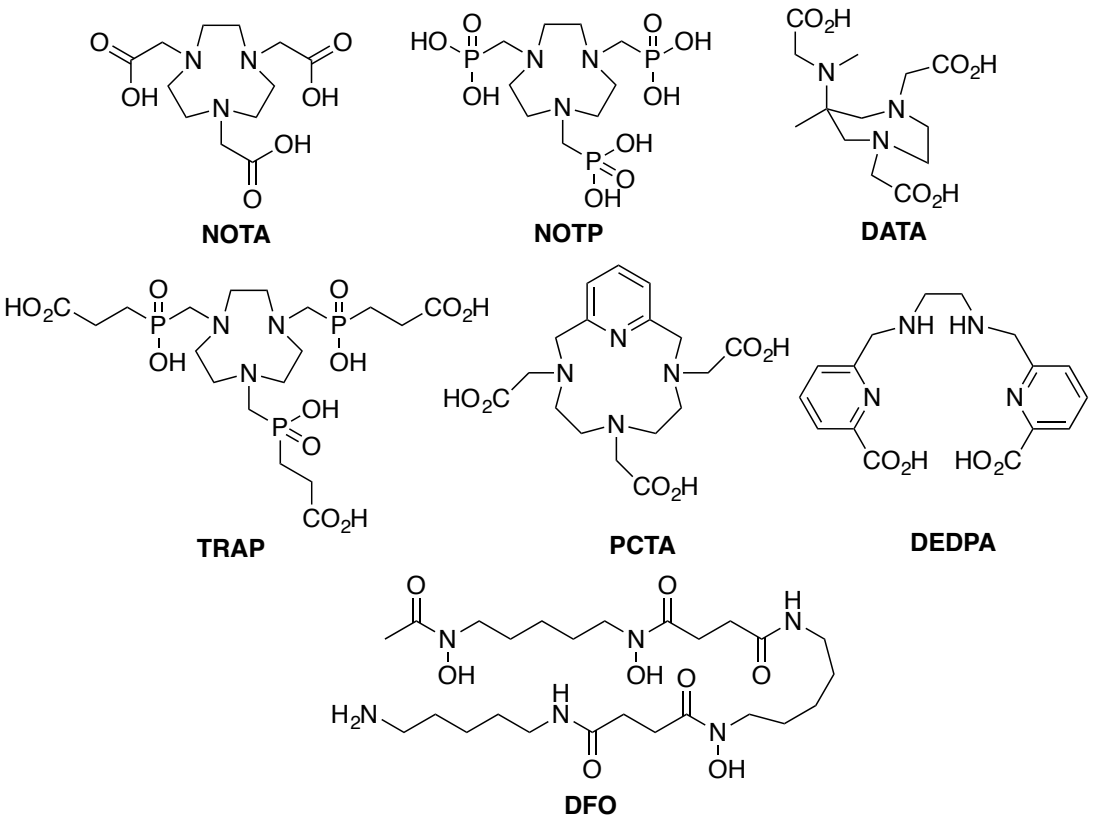

Figure 1.6: Examples of acyclic and macrocyclic chelators for Ga^{3+}.

1.4.1 TACN-Based Chelators for Ga^{3+}

The Ga^{3+} complex of the TACN-based chelator NOTA is known to have a higher kinetic stability than its DOTA counterpart.[43] This has been largely attributed to the size of the cavity of the TACN derivative (a nine-membered triazamacrocycle) being more ideally suited to the size of the Ga^{3+} cation than DOTA (a twelve-membered triazamacrocycle).[44] NOTA, NOTP and TRAP all form six-coordinate complexes with Ga^{3+}. They are known to be highly rigid (due to the preformed geometry offered by the macrocycle), kinetically inert and thermodynamically stable due in part to the macrocyclic effect (stability constants log $K_1 > 26$, **Table 1.4**),[45] which encompasses entropic gain from a pre-organised structure around metal ions. [32]

Table 1.4: Proton and Ga^{3+} affinity constants of example Ga^{3+} chelators.

Chelator	log K_a	log K_1
NOTA[46]	13.17, 5.74, 3.22, 1.96	29.63
NOTP[47]	11.7, 9.1, 7.5, 5.8, 3.1, 0.9	-
TRAP[48]	11.48, 5.44, 4.84, 4.23, 3.45, 1.66	26.24
DFO[49]	10.79, 9.55, 8.96, 8.32	28.65
DOTA[50]	11.74, 9.76, 4.68, 4.11, 2.37	26.05

In the case of [Ga(NOTA)], the X-ray crystal structure of the complex indicates that the distorted octahedral coordination environment contains three deprotonated carboxyl groups.[51] [Ga(TRAP)] has been shown to exhibit a similar coordination environment to [Ga(NOTA)], with deprotonated phosphonic acids contributing the O_3 donor atoms. Solution-based studies of [Ga(NOTP)] have provided insight into the binding mode of the Ga^{3+} ion.[40b, 45] It was proposed that upon coordination, one of the hydroxyl groups from each phosphonic acid group in NOTP deprotonates.

The radiolabelling properties of these chelators with $^{68}Ga^{3+}$ have been investigated. TRAP was shown to quantitatively incorporate $^{68}Ga^{3+}$ at a reduced ligand concentration (up to 10-fold less) compared with DOTA and NOTA at 25 °C and pH 6.5.[40b] The incorporation of phosphinic acid groups into the TACN macrocycle allowed for more efficient binding than that of NOTA due to the lower pK_a value of phosphinic acids when compared to carboxylic acids. The incorporation of phosphinate groups has allowed $^{68}Ga^{3+}$ labelling in acidic conditions (< pH 2), where generation of insoluble $Ga(OH)_3$ can be avoided.[52] Phosphonate-containing ligands such as NOTP have been shown to chelate $^{68}Ga^{3+}$ at room temperature and neutral pH. The binding efficiencies of NOTP, NOTA and TRAP were determined from the radiochemical yields. Radiochemical yield (RCY) is defined as the amount of radioactivity in the product expressed as a percent of related starting radioactivity used in the corresponding synthesis, and is dependent on pH, temperature and concentration.[53] Complexes of NOTP bound to $^{68}Ga^{3+}$ produced higher RCY than both NOTA and TRAP at pH 6.5 and 25 °C.[32] The utility of these

chelators for radiopharmaceutical applications relies on the synthetic chemist's ability to synthesise bifunctional derivatives that can be covalently tethered to targeting biomolecules, such as peptides and antibodies.

1.4.2 Bifunctional Chelating Strategies

Bifunctional chelators (BFC) are molecules that serve the dual purpose of binding a radiometal forming a stable complex, whilst leaving a functional group for bioconjugation to a biologically active vector molecule.[42] Carboxylic acids, primary amines, azides and thiols are popular functional groups in this regard.[42] Attachment of the vector can occur using different methods, with isothiocyanate-amine thiourea formation, amide formation, maleimide-thiol Michael addition, activated ester-amine amide formation, and Cu^{+}-catalysed cycloadditions being popular choices (**Figure 1.7**).

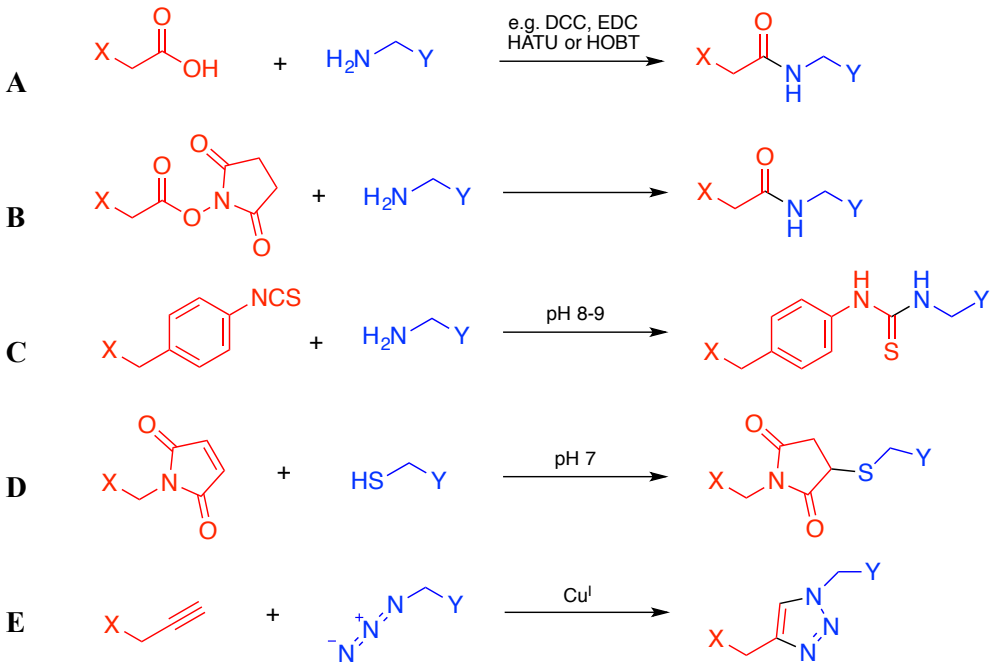

Figure 1.7: Examples of bioconjugation reactions for attachment of bifunctional chelators to biomolecules. X = chelator; Y = biomolecule. (A) standard amide bond formation between a carboxylic acid and a primary amine with coupling reagents; (B) peptide coupling reaction between an activated ester of *N*-hydroxysuccinimide and a primary amine; (C) reaction between an isothiocyanate and a primary amine to form a thiourea bond; (D) reaction between a maleimide and a thiol to form a thioether; and (E) standard Cu^{I}-catalysed azide-alkyne 1,3-dipolar cycloaddition. Adapted from Price *et al.*[9]

Additionally, modifying the linker connecting the BFC and biomolecule has been shown to alter properties such as the overall charge, the solubility of the radiopharmaceutical in aqueous solutions, as well as the pharmacokinetic and biodistribution patterns of the conjugate.[54]

1.5 Project Aims

The aim of this project is to synthesise and characterise a TACN-based BFC, **H_3L^1**, that possesses both phosphonate and carboxylate functional groups, as well as a site for bioconjugation. The synthesis will be conducted using both solution and solid-phase synthesis techniques. Elucidation of solid-state structures and radiolabelling of **H_3L^1** with $^{68}Ga^{3+}$ will allow for comparison with current TACN-based BFC agents.

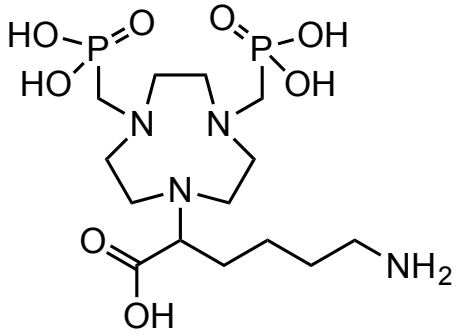

Figure 1.8: A novel bifunctional chelator, **H_3L^1**.

Aims

1. Develop synthetic routes to synthesise **H_3L^1** in solution and using solid-phase synthesis;
2. Fully characterise **H_3L^1** using both spectroscopic and analytical methods, as well as the resulting non-radioactive Ga^{3+} and radioactive $^{68}Ga^{3+}$ complexes; and
3. Synthesise and characterise the solid-state structure of the [Ga**L^1**] and [Ga(NOTP)] complexes and compare both with structurally-analogous complexes, namely [Ga(NOTA)].

2 Results and Discussion – Solution-Phase Synthesis

2.1 Synthetic Planning for Solution-Phase Synthesis

The retrosynthetic analysis for **H_3L^1** is outlined in **Scheme 2.1**. The first planned step was the protection of the carboxylic acid of **1** using benzyl alcohol. Reaction of di-*tert*-butyl ester TACN (diBocTACN) was introduced under basic conditions to afford compound **3**. Subsequent deprotection of the Boc groups and neutralisation would afford the trifluoroacetate salt **4** and free base **5**. The free base **5** could then be functionalised using triethylphosphite and paraformaldehyde, resulting in the protected phosphonate **6**. Cleavage of the phthalimide protecting group using hydrazine monohydrate would introduce the primary amine on **7**. Catalytic hydrogenation using a palladium catalyst would produce the carboxylic acid **8**, and cleavage of the ethyl groups on the methylene phosphonate groups using bromotrimethylsilane (TMSBr) would result in the final target product **H_3L^1**.

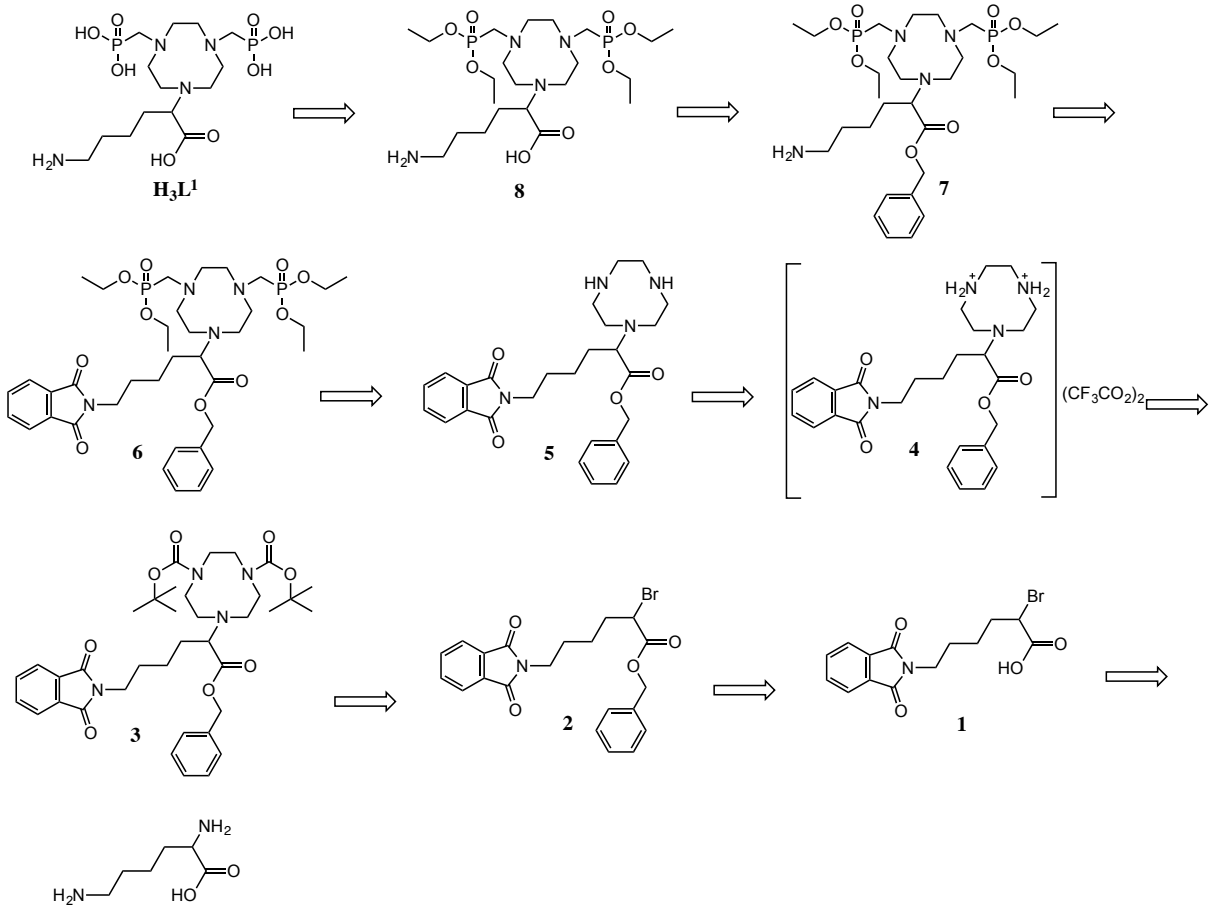

Scheme 2.1: Retrosynthetic analysis of **H_3L^1**.

2.2 Synthetic Chemistry and Characterisation of Compounds

2.2.1 Synthesis and Characterisation of Bromoacid 1

Synthesis of **1** involved amine protection with phthalimide, diazotisation and bromination of L-lysine monohydrochloride (**Scheme 2.2**). The one-pot reaction is known to result in products with high enantiomeric excess (ee), however the ee of compound **1** was not determined.[55]

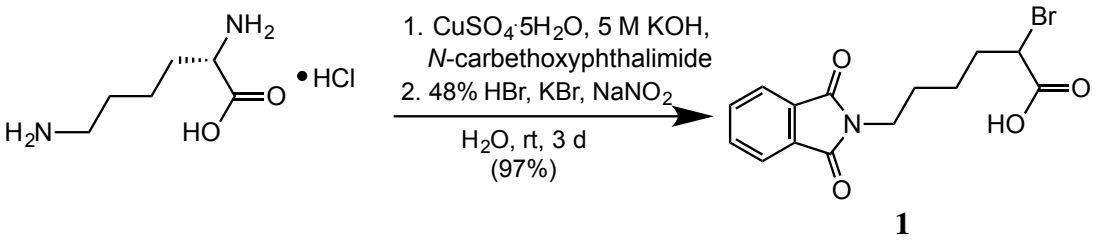

1

Scheme 2.2: L-lysine amine protection, diazotisation and bromination reaction scheme to afford compound **1**.

Copper sulfate pentahydrate was reacted with L-lysine monohydrochloride in a 1:2 ratio in water to protect the α-amino group. Coordination complexes of Cu^{2+} with diamino carboxylic acids such as the amino acids ornithine and lysine are known to form *via* the α-NH_2 group and carboxylate oxygen, which leaves a primary amine free to react (**Figure 2.1**).[56]

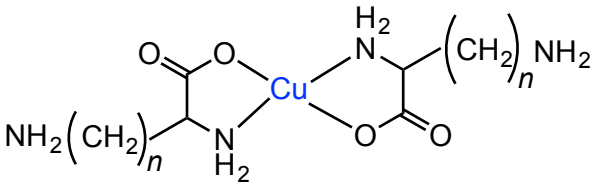

Figure 2.1: Cu^{2+} chelate complexes of ornithine (n = 3) and lysine (n = 4) enable protection of α-amino groups.

N-carbethoxyphthalimide was added whilst maintaining the pH between 9 – 10 using 5 M aqueous KOH because the reaction produces H^+, and the amine required basic pH in order to react with the phthalimide. The solution was then acidified using 48% hydrobromic acid to pH 0.4 to decomplex the Cu^{2+} ion. Finally, potassium bromide and sodium nitrite were added to facilitate the diazotisation/bromination process *via* the *in situ* formation of nitrous acid.

Studies have shown that diazotisation/bromination may be catalysed by Cu^{2+} salts in a Sandmeyer-like reaction, which may be occurring in the formation of compound **1**.[57] The characterisation of compound **1** was achieved through nuclear magnetic resonance (NMR) spectroscopy, electrospray ionisation (ESI) mass spectrometry (MS) and infrared (IR) spectroscopy. By using 2D NMR heteronuclear correlation experiments, proton and carbon chemical shifts for compound **1** were fully assigned (**Figure 2.2**).

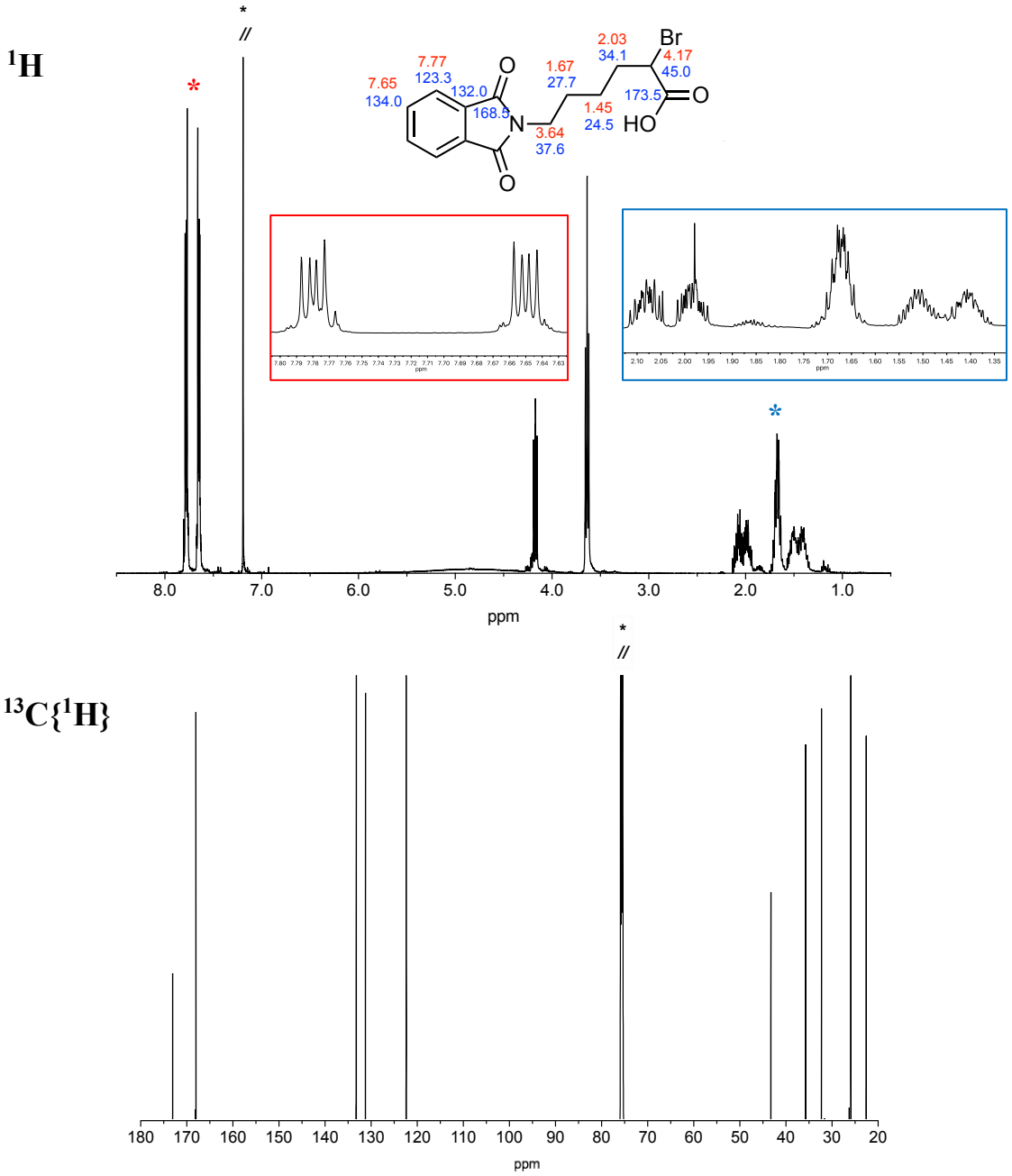

Figure 2.2: ^{1}H (top, red assignments) and $^{13}C\{^{1}H\}$ (bottom, blue assignments) NMR spectra of **1** in $CDCl_3$. The residual solvent peak and solvent impurities are marked with black asterisks. Insets: partial ^{1}H spectra showing AA'BB' splitting of phthalimide protons (red) and diastereotopic protons (blue).

Chiral molecules such as L-lysine and its derivatives are known to contain diastereotopic protons. The diastereotopic CH_2 protons in **1** (δ = 1.45, 1.67 and 2.03 ppm) show complex multiplet splitting patterns in the ^1H NMR spectrum, indicating that they are in different chemical environments. The benzylic protons in the phthalimide benzyl group exhibited second-order spectral profiles and magnetic inequivalence in an AA'BB' (*o*-dichlorobenzene type) spin system.[58] In such a system, each A proton is coupled differently to the B and B' protons. Additionally, the AA'BB' pattern is complex because the coupling constant J_{AB} (J = 7.56 Hz, *ortho* coupling) is much larger than $J_{AB'}$ (J = 3.33 Hz, *meta* coupling). The spectrum consists of two identical 8-line half spectra, each symmetrical about its midpoint. As an example of the processes involved in assigning chemical shifts using 2D heteronuclear correlation, the assignment of the ^1H and $^{13}C\{^1H\}$ spectra of **1** using the heteronuclear single quantum correlation (HSQC) and heteronuclear multiple-bond correlation (HMBC) spectra is shown in **Figure 2.3**.

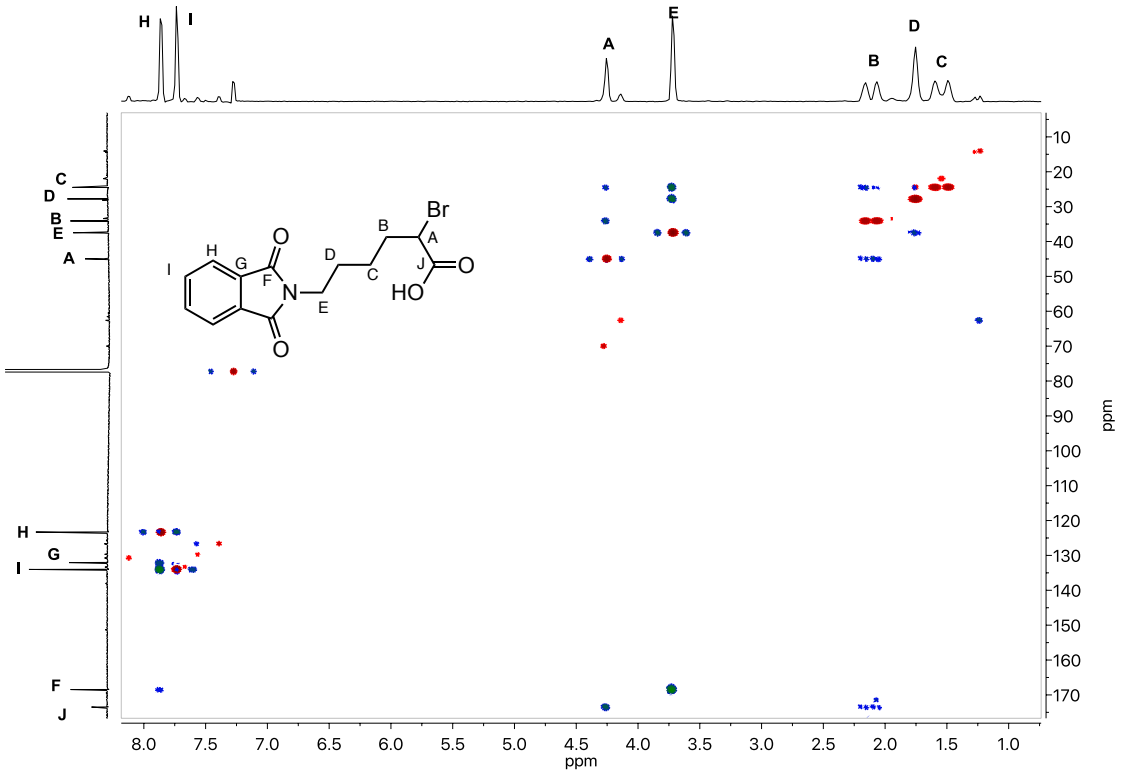

Figure 2.3: HSQC (red) and HMBC (blue) overlaid NMR spectra of compound **1**. By considering chemical shifts and through-bond correlations, ^1H and ^{13}C shifts can be assigned to each nucleus present.

The ^{1}H-^{1}H correlated spectroscopy (COSY) spectrum was also used to assign chemical shifts. The same logic was used to assign the ^{1}H and ^{13}C spectra of all compounds in this project. The aromatic region of the ^{1}H NMR spectrum contains two multiplets at 7.65 and 7.77 ppm corresponding to the four protons in the phthalimide group. The integration of these peaks showed that two protons were in each environment. This was confirmed by the COSY spectrum, which indicated that the two peaks were correlated. The peak at 4.17 ppm was assigned to the single proton on the carbon adjacent to the bromine atom. In the COSY, this peak correlated to the 2.03 ppm protons on the adjacent methylene carbon. The same method of assignment was made for the other methylene protons, culminating at the singlet observed at 3.64 ppm. The carboxylic acid O*H* hydrogen was not observed in the ^{1}H spectrum, most likely due to intermolecular chemical exchange.

The ^{13}C{^{1}H} spectrum was assigned using the HSQC and HMBC spectra. The aromatic carbon signals were observed at 123.3, 132.1 and 134.0 ppm. The phthalimide carbonyl and carboxylic acid carbon signals were downfield at 168.5 and 173.5 ppm, and were coupling to the ^{1}H signals at 3.64 and 4.17 ppm in the HMBC spectrum, respectively. The signals at 24.5, 27.7 and 34.1 ppm were assigned to the carbons in the alkyl chain through correlations in the HSQC spectrum.

Mass spectrometry was also used to characterise **1**. The ESI mass spectrum of **1** showed two peaks at *m/z* = 338.0041 and 340.0020, which are characteristic of the presence of the naturally-occurring isotopes ^{79}Br (51 %) and ^{81}Br (49 %).

2.2.2 Synthesis and Characterisation of Benzyl Ester 2

The carboxylic acid of **1** was protected as a benzyl ester *via* the Steglich esterification (**Scheme 2.3**).

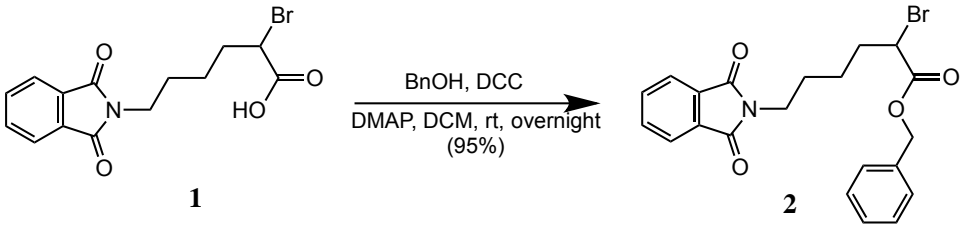

Scheme 2.3: Steglich esterification of **1** forming a benzyl ester.

The Steglich esterification is the reaction between a carboxylic acid and an alcohol in the presence of dicyclohexylcarbodiimide (DCC) and catalytic amounts of 4-dimethylaminopyridine (DMAP) to form an ester. The reaction utilises DCC as a coupling reagent, which first reacts with the carboxylic acid **1** forming a more reactive *O*-acylisourea intermediate in DCM. DMAP acts as a nucleophile and reacts with the *O*-acylisourea leading to a highly reactive amide and eliminating dicyclohexylurea (DCU). Without the addition of DMAP, it has been shown that undesirable side-products may form.[59] Subsequent nucleophilic attack of benzyl alcohol produces the ester **2**, whilst DMAP is regenerated (**Scheme 2.4**). Following overnight stirring at room temperature, the product was purified by silica chromatography and produced a yield of 95 %. Ester **2** was characterised by ^{1}H and $^{13}C\{^{1}H\}$ NMR spectroscopy (**Figure 2.4**).

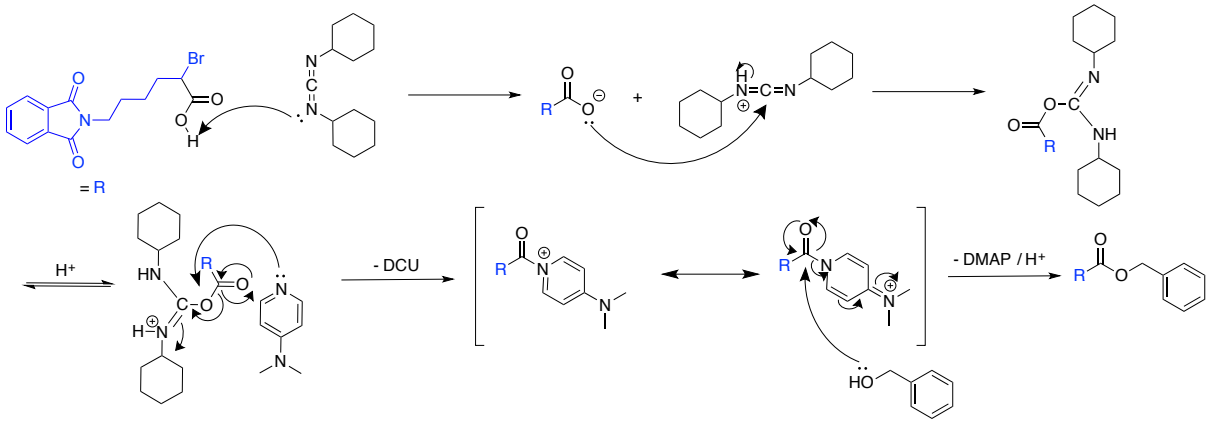

Scheme 2.4: Mechanism of the Steglich esterification of **1**.

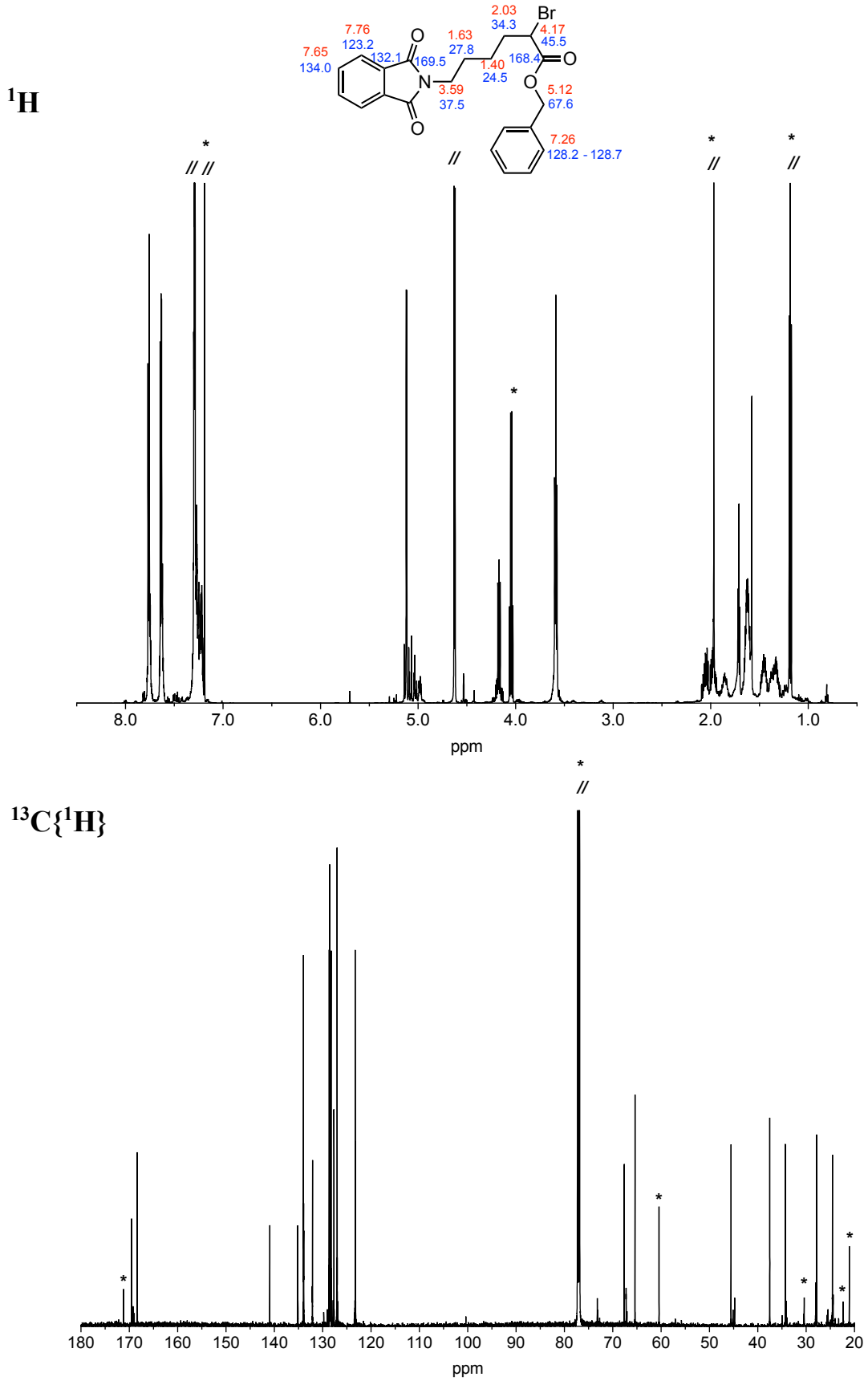

Figure 2.4: ^{1}H (top, red assignments) and $^{13}C\{^{1}H\}$ (bottom, blue assignments) NMR spectra of **2** in $CDCl_3$. The residual solvent peak and solvent impurities are marked with asterisks.

The ^{1}H NMR spectrum of **2** appears to be very similar to that of **1**, with the addition of a sharp multiplet at 7.29 ppm corresponding to the aromatic hydrogens on the benzyl group, as well as the multiplet corresponding to the ester CH_2 at 4.17 ppm. The disatereotopicity of the methylene protons (δ = 1.31 – 2.03 ppm) remains a prominent feature, with complex multiplet splitting patterns present. A large triplet is evident for the two methylene protons (δ = 3.59 ppm, ^3J = 7.28 Hz) adjacent to the phthalimide nitrogen. This is surprising given that the other three CH_2 groups are diastereotopic, however can be reasoned when the molecular symmetry of the system is considered. Phthalimide groups are known to have a C_2 axis of symmetry.[60] Any CH_2 groups that lie on the C_2 rotation axis are not considered diastereotopic, and are instead homotopic, and are shown as existing in a single environment in the ^{1}H NMR spectrum (**Figure 2.5**). ESI-MS was also used to confirm the identity of **2** (*m/z* = 430.0631 $[M + H]^+$).

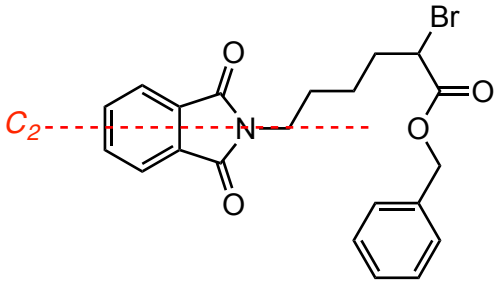

Figure 2.5: C_2 axis of symmetry in compound **2**. The CH_2 protons adjacent to the phthalimide lie on this axis and do not show disatereotopicity.

2.2.3 Synthesis and Characterisation of Di-*tert*-butyl Ester 3

The synthesis of the di-*tert*-butyl ester TACN derivative, **3**, began with the synthesis of the precursor, diBocTACN (**Scheme 2.5**).

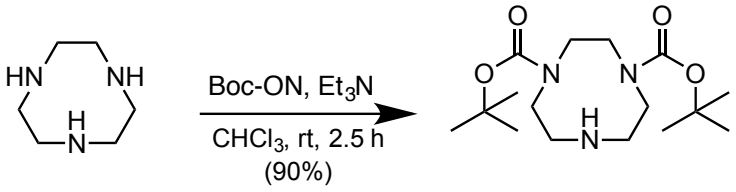

Scheme 2.5: Selective *N*-protection of two secondary amines in TACN with Boc-ON.

Following a literature procedure, two equivalents of Boc-ON were slowly added to a solution of TACN in $CHCl_3$ that had been pre-treated with triethylamine (Et_3N).[61] The product was synthesised in high yield (90%) and purity as shown in the ^1H and $^{13}C\{^1H\}$ spectra, apart from some slight ethyl acetate, despite extensive drying *in vacuo* (**Figure 2.6**).

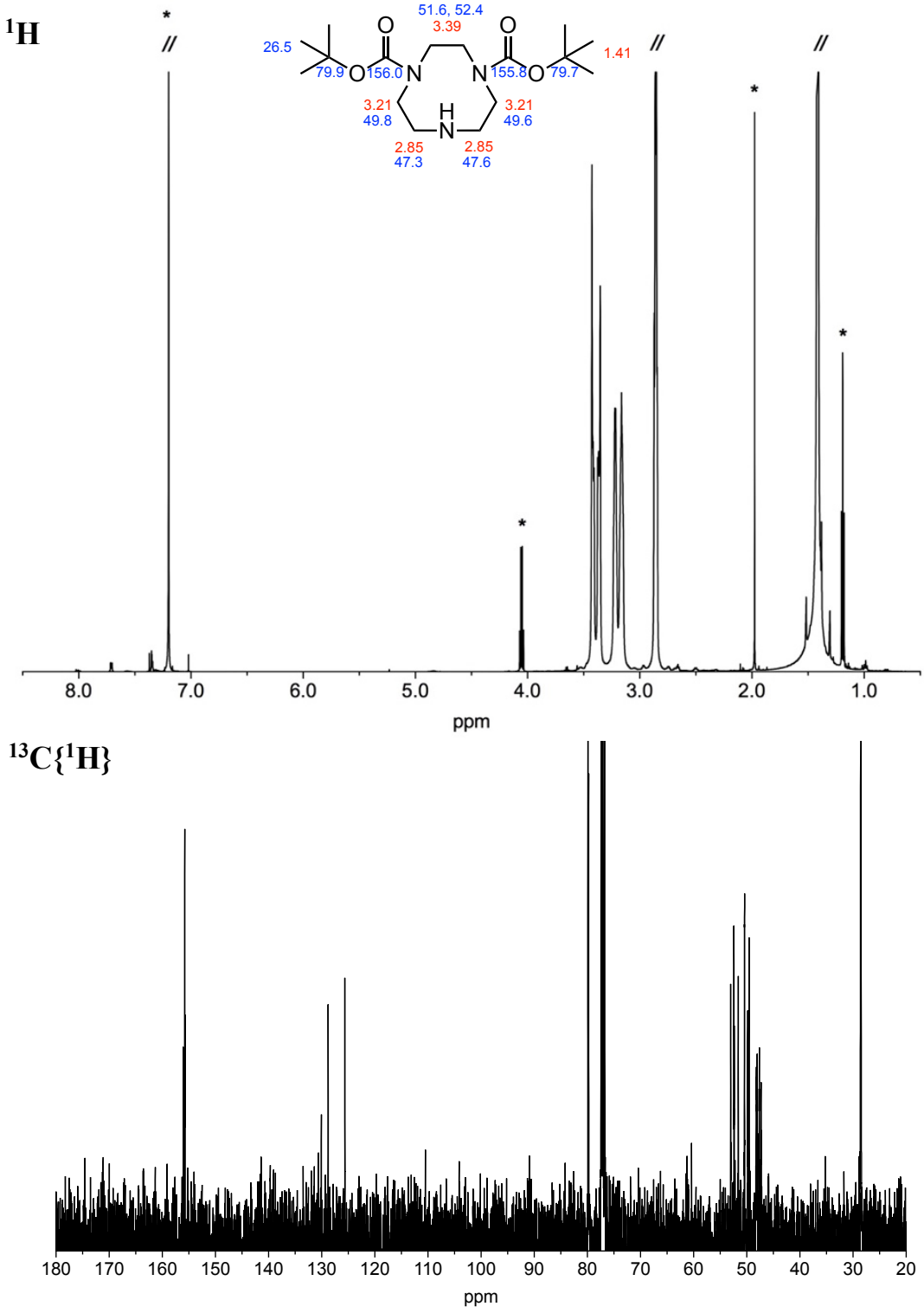

Figure 2.6: ^1H (top, red assignments) and $^{13}C\{^1H\}$ (bottom, blue assignments) NMR spectra of diBocTACN in $CDCl_3$. The residual solvent peak and solvent impurities are marked with black asterisks.

The ester, diBocTACN, has previously been reported to crystallise as white crystals following refrigeration below 0 °C.[61] However, the product obtained was a yellow oil, and did not change in appearance following several days storage at 0 °C. Initial *N*-alkylation experiments with **2** were conducted using potassium hydroxide as the base and toluene as the solvent. However, only starting material was isolated. The free secondary amine of diBocTACN was successfully alkylated with **2** using K_2CO_3 in acetonitrile *via* a S_N2 nucleophilic substitution reaction. The reaction was monitored by thin-later chromatography (TLC) and completed over two days with stirring at room temperature (**Scheme 2.6**).

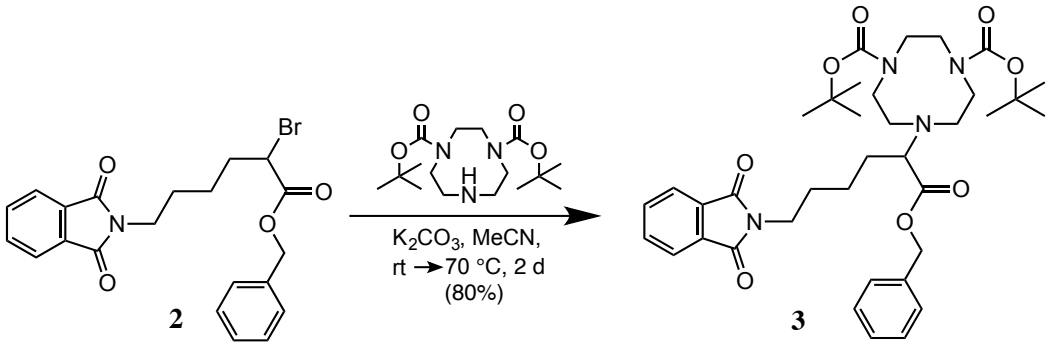

Scheme 2.6: *N*-monoalkylation of diBocTACN with **2**.

The room temperature ^1H and $^{13}C\{^1H\}$ NMR spectra of **3** contains signals that exhibit unusual splitting. These signals correspond to groups close to the carbamate bonds. In the ^1H NMR spectrum, the multiplet signal corresponding to the *tert*-butyl groups (δ = 1.41 – 1.44 ppm) is quite broad and deviates from the expected singlet. In the $^{13}C\{^1H\}$ NMR spectrum, the quaternary (δ = 77.5, 78.1 ppm), carbonyl (δ = 153.8, 154.2 ppm) and two methylene (δ = 49.7, 50.0, 50.6, 50.8 ppm) carbons are all split into two multiplet signals (**Figure 2.7**). This was rationalised to be caused by the partial double bond character of the carbamate bond, and the associated hindered C-N bond rotation.

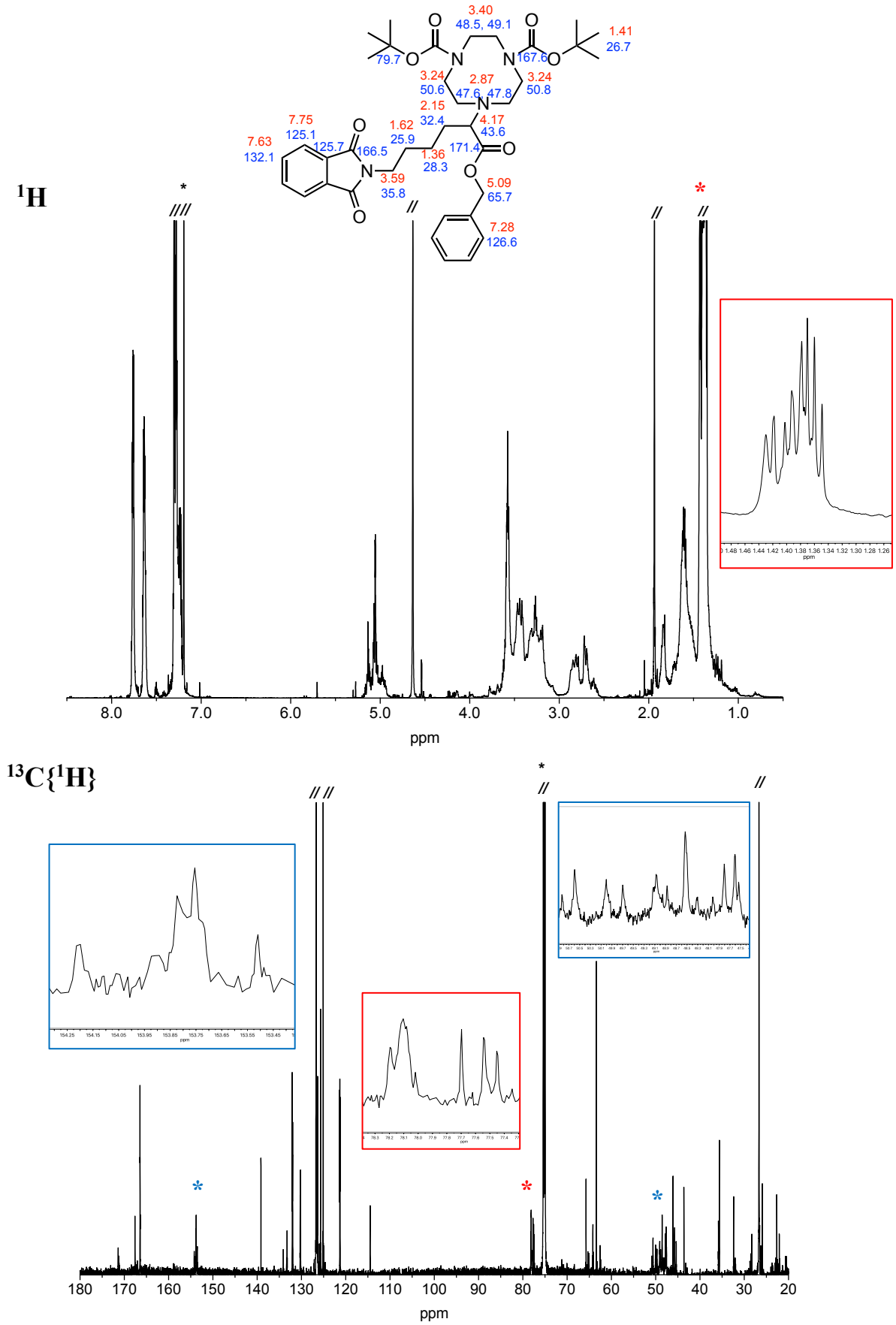

Figure 2.7: ^{1}H (top, red assignments) and $^{13}C\{^{1}H\}$ (bottom, blue assignments) NMR spectra of **3** in $CDCl_3$. Insets: ^{1}H (top) Boc multiplet signal; ^{13}C (bottom) multiplet signals for groups in proximity to the carbamate bonds. The residual solvent peak and solvent impurities are marked with black asterisks.

Carbamates exhibit resonance similar to that of amides.[62] Electron delocalisation and loss of conjugation of the heteroatom-(σ-bond)-carbon-(π-bond)-heteroatom system results in a partial double bond character of the C-N bond, hindering rotation around this bond (**Figure 2.8**).

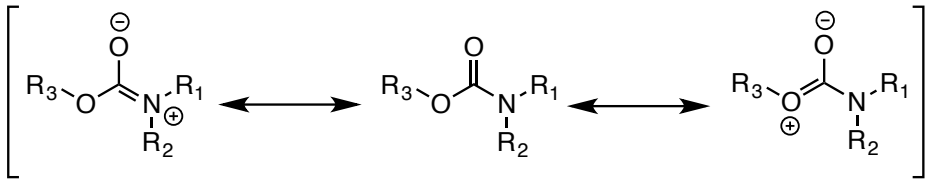

Figure 2.8: Possible resonance structures of the carbamate bond.

Variable-temperature ^{1}H NMR experiments were undertaken to investigate the observations noted in the NMR spectra (**Figure 2.9**). This was motivated by the thought that different isomers of **3** may be interconverting on the NMR timescale. Increasing the temperature may result in an averaging of the signals because the interconversion would be faster than the timescale of the NMR. As the temperature was increased from 298 K to 398 K, the *tert*-butyl peaks in the ^{1}H NMR appeared to coalesce into two sharp singlets (δ = 1.41 and 1.43 ppm). In the diBocTACN precursor, these two groups did not appear as separate peaks due to the centrosymmetric nature of the molecule. A possible explanation could be that the *t*-Boc groups are interconverting between confirmations, and that the partial double-bond character of the carbamate bond is causing hindered rotation. Without a crystal structure of **3**, it is difficult to predict the isomers that could be formed, as the preformed geometry of the macrocycle inhibits traditional s-*trans* and s-*cis* isomerism, as in acyclic carbamates.[62] This may also help to explain the unusual splitting patterns observed in the ^{13}C{^{1}H} spectrum.

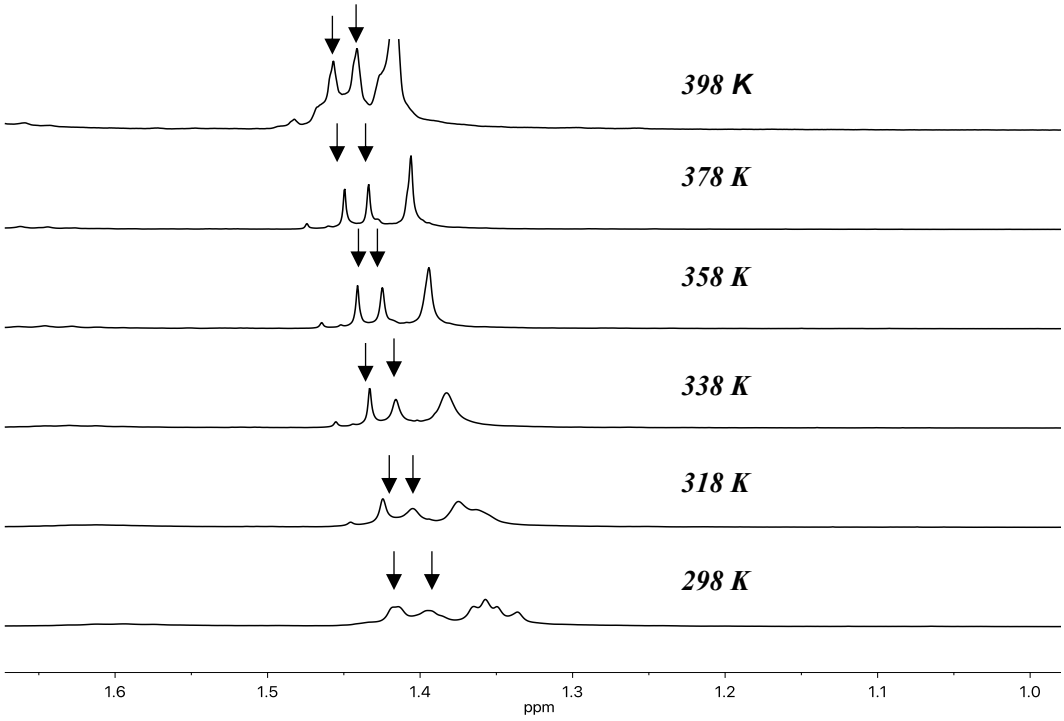

Figure 2.9: Variable-temperature ^{1}H NMR spectrum (δ = 1.0 – 1.65 ppm) of **3** in DMSO-*d*$_6$. Two sharp singlets are observed at 1.42 and 1.44 ppm at 398 K for the Boc signals (black arrows). The third signal at 1.35 ppm (298 K) is a methylene peak and not associated with the Boc groups or carbamate bond.

2.2.4 Synthesis and Characterisation of 5 *via* TFA Salt 4

The Boc groups of **3** were removed using trifluoroacetic acid (TFA), which was slowly added to a solution of **3** in DCM over 30 min to afford the trifluoroacetate salt **4**. Neutralisation of this species using base (1 M aqueous NaOH) gave the *N*-monosubstituted TACN derivative **5** with a yield of 66% (**Scheme 2.7**).

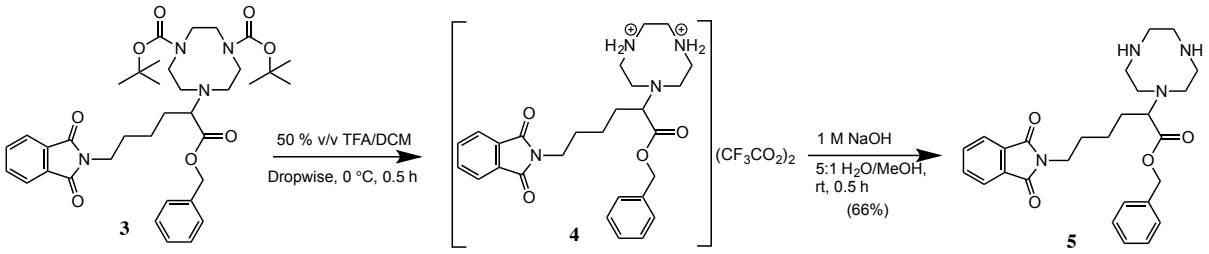

Scheme 2.7: Deprotection of **3** and neutralisation to afford the free base **5**.

The ESI-MS data collected for **4** indicated the presence of the monocation $[\mathbf{4} - H]^+$ at *m/z* = 479.2648. The trifluoroacetate salt was able to be characterised using ^{1}H, $^{13}C\{^{1}H\}$, and ^{19}F NMR. The ^{19}F NMR spectrum includes two singlets, which can be assigned to the trifluoroacetate counter-ions and residual trifluoroacetic acid (**Figure 2.10**).[63] The ^{1}H NMR spectrum was successfully assigned and the results are outlined in **Table 2.1**.

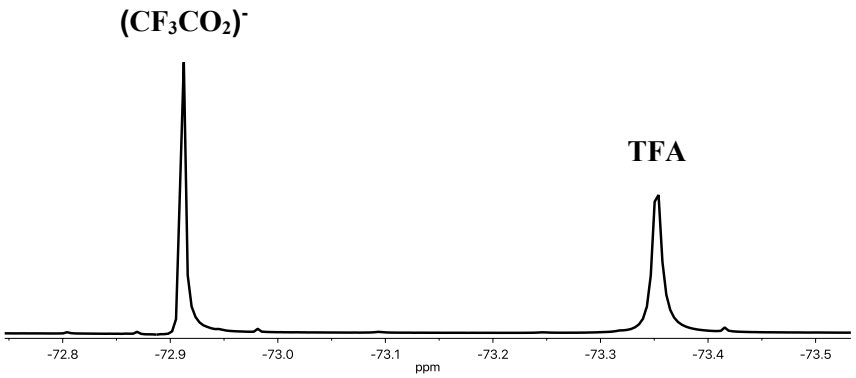

Figure 2.10: ^{19}F NMR spectrum of **4** in methanol-d_4, reported with respect to $CFCl_3$.

Table 2.1: ^{1}H NMR chemical shifts and assignments for **4**.

Chemical shift	Multiplicity	Integration	Functional group
1.34 – 1.50	m	2H	C*H*$_2$
1.64 – 1.77	m	2H	C*H*$_2$
1.78 – 2.09	m	2H	C*H*$_2$
3.02 – 3.27	m	2H	C*H*$_2$ macrocycle
3.33 – 3.35	m	6H	C*H*$_2$ macrocycle
3.36 – 3.47	m	2H	C*H*$_2$ macrocycle
3.58 – 3.66	m	2H	C*H*$_2$
3.67 – 3.76	m	2H	C*H*$_2$ macrocycle
4.61	s	1H	C*H*
5.11 – 5.29	m	2H	OC*H*$_2$
7.24 – 7.39	m	5H	Ar*H*
7.73 – 7.90	m	4H	Ar*H*

The protons of the secondary ammonium groups were not present in the spectrum, probably arising from chemical exchange. The signals associated with the macrocyclic methylene protons were difficult to assign and required the use of 2D heteronuclear NMR (HSQC and HMBC). The $^{13}C\{^{1}H\}$ NMR spectrum includes two quartets (δ = 157.5 and 159.7 ppm, $^{2}J_{CF}$ = 25 Hz), which correspond to the carbonyl groups of the trifluoroacetate anion and residual TFA, respectively, coupling with the three ^{19}F atoms. A quartet (δ = 115.6 ppm, $^{1}J_{CF}$ = 188 Hz) indicative of the CF_3 carbon of the trifluoroacetate counterion is also present (**Figure 2.11**).

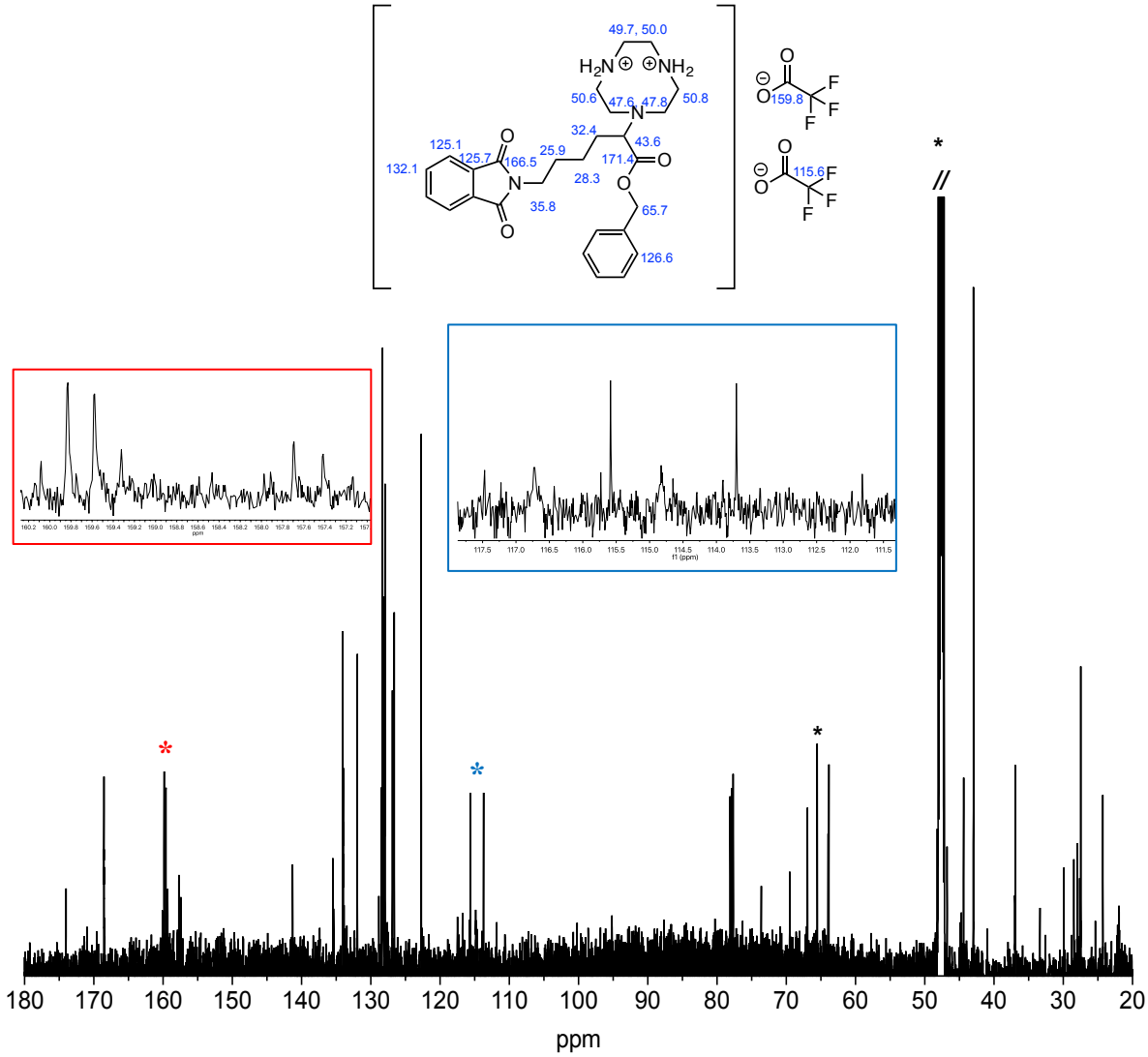

Figure 2.11: $^{13}C\{^{1}H\}$ NMR spectra of **4** in methanol-d_4. Insets: a quartet at 115.6 ppm corresponding to the CF_3 of the counterions and two quartets at 157.5 and 159.7 ppm corresponding to C=O of the TFA counterions and residual TFA are observed. The residual solvent peak and solvent impurities are marked with black asterisks.

The ^{1}H NMR spectrum of the free base **5** was more easily assigned than the spectrum of **4**, with the macrocyclic methylene protons (δ = 2.57 – 3.08 ppm) being more easily distinguishable as separate multiplets (**Table 2.2**). The secondary amine protons were not observed, most likely due to the signal broadening out due to intermolecular exchange. The ^{13}C{^{1}H} and ^{19}F NMR spectra of **5** indicated the absence of TFA counterions.

Table 2.2: ^{1}H NMR chemical shifts and assignments for **5**.

Chemical shift	Multiplicity	Integration	Functional group
1.32 – 1.37	m	2H	C*H*$_2$
1.60 – 1.62	m	2H	C*H*$_2$
1.98 – 2.04	m	2H	C*H*$_2$
2.57 – 2.69	m	4H	C*H*$_2$ macrocycle
2.70 – 2.82	m	4H	C*H*$_2$ macrocycle
2.89 – 3.08	m	4H	C*H*$_2$ macrocycle
3.50 – 3.60	m	2H	C*H*$_2$
4.13 – 4.17	m	1H	C*H*
5.02 – 5.11	m	2H	OC*H*$_2$
7.17 - 7.19	m	5H	Ar*H*
7.60 – 7.62	m	2H	Ar*H*
7.72 – 7.74	m	2H	Ar*H*

2.2.5 Synthesis and Characterisation of α-Aminophosphonate 6

The most common route to access α-aminophosphonates is the hydrophosphonylation of imines (**Scheme 2.8**). This can be achieved through two pathways: (i) in a two-component fashion known as the Pudovik reaction or (ii) in a three-component fashion known as the Kabachnik-Fields reaction.[64] The Kabachnik-Fields reaction combines the *in situ* formation of an imine by condensation of an amine with an aldehyde or ketone, with the hydrophosphonylation step.

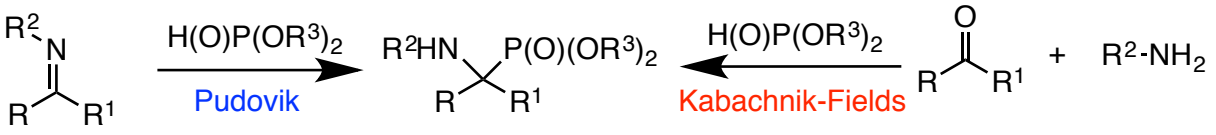

Scheme 2.8: Formation of α-aminophosphonates *via* Pudovik and Kabachnik-Fields reactions.

The Pudovik reaction mechanism is relatively straightforward and is known to proceed through a five-membered cyclic transition state involving the dialkyl phosphite and the imine. The mechanism for the Kabachnik-Fields reaction is more complicated.[65] The nature of the aldehyde, solvent and pK_b of the amine all appear to have an effect on the Kabachnik-Fields reaction pathway.[66] The synthesis of **6** has proven to be challenging. A modified Kabachnik-Fields reaction, following a similar synthetic procedure as Zeng and co-workers, was attempted in the first instance.[67] Triethyl phosphite and paraformaldehyde were added to **5** in a 2:2.2:1 ratio at room temperature with **5** in THF and stirred for 3 days. Following work-up the ^{1}H and ^{13}C{^{1}H} NMR showed only unreacted **5**. This was thought to be due to the imine not being formed because the reaction was conducted at room temperature. Subsequent reactions formed mixtures of the mono- and di-substituted phosphonate. Following a number of unsuccessful experiments to selectively form the di-substituted species, the α-aminophosphonate **6** was successfully synthesised under modified Kabachnik-Fields reaction conditions (**Scheme 2.9**).

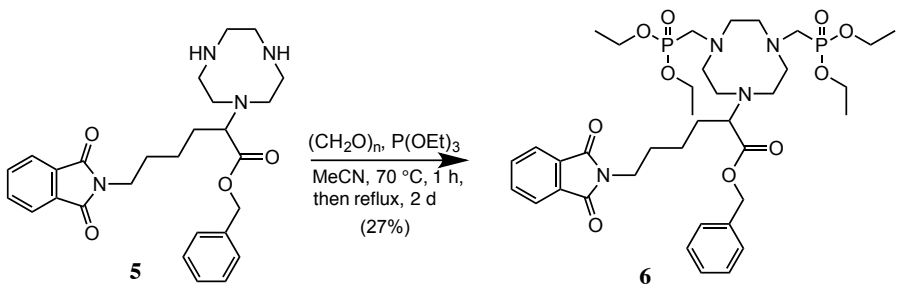

Scheme 2.9: Synthesis of α-aminophosphonate **6** *via* a modified Kabachnik-Fields reaction.

The free base **5** was reacted with paraformaldehyde for 1 hour at 70 °C to form the intermediate imine. Triethyl phosphite was then added and the mixture was heated to reflux and

stirred for 2 days. The crude product was isolated, extracted with diethyl ether, isolated as an orange oil and characterised using ^{1}H, $^{13}C\{^{1}H\}$ and 2D (HSQC, HMBC) NMR was successfully undertaken (**Figure 2.12**). Free base **5** and mono-substituted phosphonate species were absent from the NMR spectra and the ESI mass spectrum. The product **6** was observed in the ESI mass spectrum at *m/z* = 779.3549, $[\mathbf{6} + H]^{+}$.

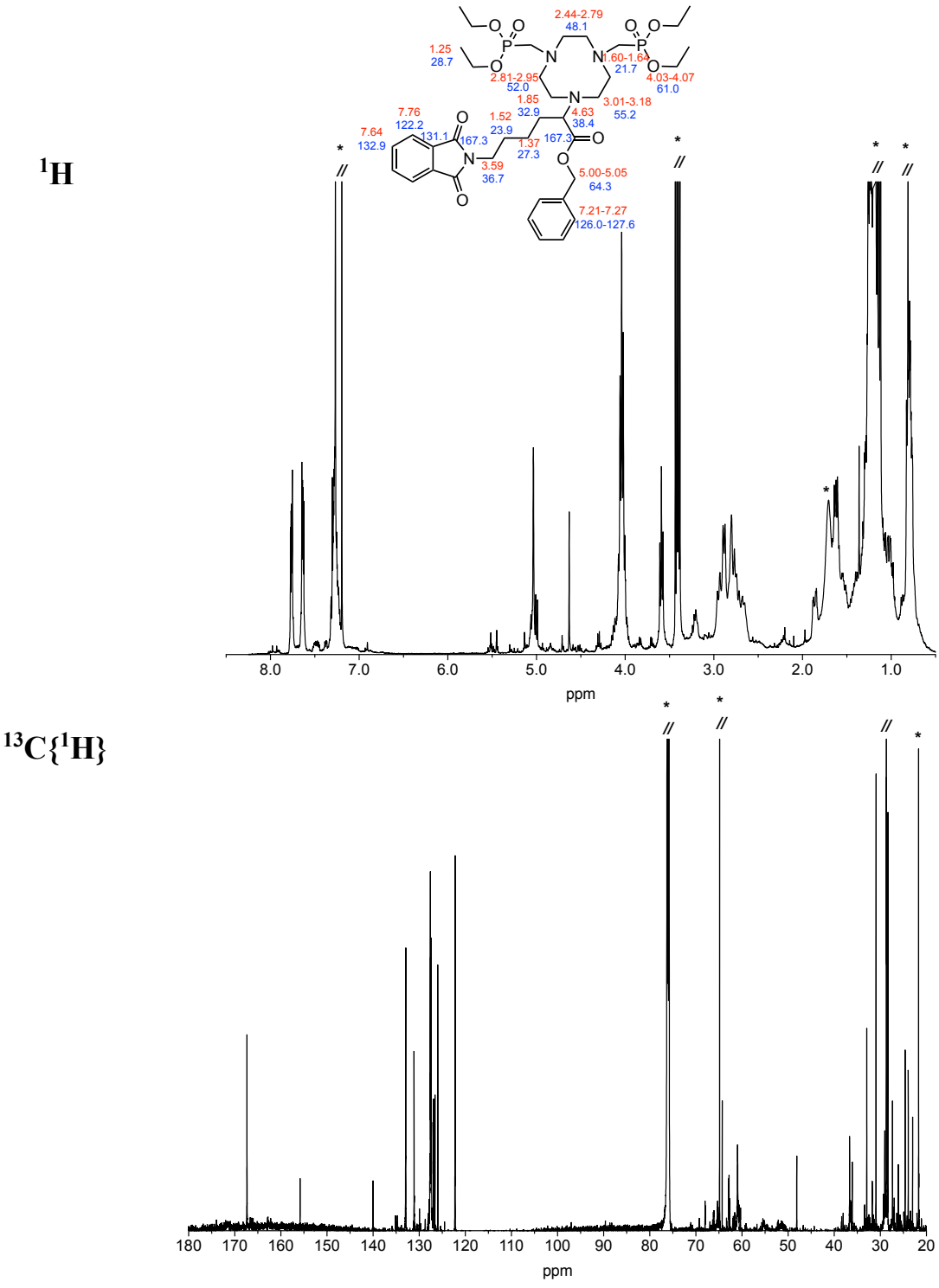

Figure 2.12: ^{1}H (top, red assignments) and $^{13}C\{^{1}H\}$ (bottom, blue assignments) NMR spectra of **6** in $CDCl_3$. The residual solvent peak and solvent impurities are marked with black asterisks.

Due to time constraints, the synthesis of **H_3L^1** was unable to be completed. The synthesis was planned to proceed *via* the following method: (1) deprotection of the primary amine with hydrazine; (2) conjugation of a model amino acid through the formation of a peptide bond with the primary amine functional group; (3) hydrogenation of the benzyl ester to produce the carboxylic acid group and; (4) hydrolysis of the diethyl phosphonates to produce the phosphonic acids. There are two common methods that are used to hydrolyse phosphonates to produce the respective phosphonic acids. The most common method is to use concentrated HCl solution (35-37 % in water; ~12 M) at reflux for 1 to 12 h. At the end of the reaction the excess HCl and water can be readily removed by distillation and any remaining water can be removed by azeotropic distillation with toluene.[68] This method usually involves refluxing the hydrochloric acid with the phosphonate for several hours and, upon cooling, the phosphonic acid precipitates within the reaction vessel. However, this method is unsuitable for molecules containing acid-sensitive functional groups such as amide bonds. This is particularly undesirable in systems where short-chain peptides, whose structure is linked together by amide bonds, are incorporated.

An alternative and less harsh method is McKenna's method.[69] In 1977, C. E. McKenna and co-workers reported the use of TMSBr to perform a transesterification of dialkyl phosphonates to the bis(trimethylsilyl) phosphonates. Following hydrolysis at room temperature, the respective phosphonic acids were produced. Previous work involving phosphonate-substituted DOTA chelators have shown that TMSBr can be used to produce phosphonic acids.[70] It was envisaged at the beginning of this project that TMSBr might present an efficient method for producing phosphonic acids from **6**.

3 Solid-Phase Synthesis

3.1 Synthetic Planning and Motivation for Solid-Phase Synthesis

Since its development in the early 1960s, solid-phase synthesis (SPS) has been the method of choice for peptide synthesis. A stepwise strategy is often used for small and medium-sized peptides, whilst a convergent strategy is used for larger peptides.[71] This method of synthesis has also been used for the synthesis of small molecules and biomolecules. SPS is largely dependent on the type of solid-phase support used. 2-Chlorotrityl chloride (CTC) resin is particularly useful for small molecule synthesis. CTC resin is a polymer support functionalised with chlorotrityl groups that form covalent bonds with nucleophiles such as carboxylates, and which can be cleaved under acidic conditions.[72] This also allows CTC resin to be used as a solid-phase carboxylic acid pseudo-protecting group (**Figure 3.1**). Temporary protection and deprotection of carboxylic acids in solution, by contrast, can be a complicated process.[73]

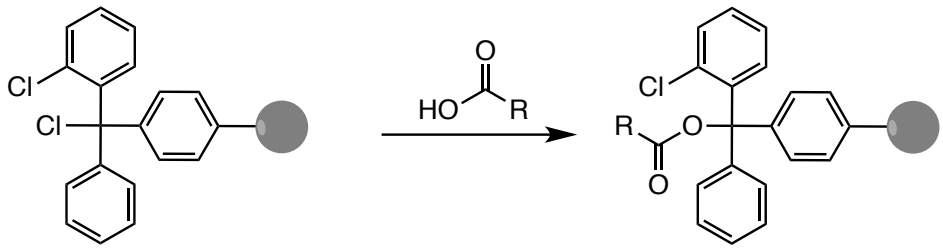

Scheme 3.1: 2-Chlorotrityl chloride (CTC) resin functioning as a temporary protecting group for carboxylic acids.

BFCs can also be conjugated to targeting peptides using SPS for use in radiopharmaceuticals. SPS can circumvent a number of the drawbacks associated with the synthesis of $\mathbf{H_3L^1}$. Fewer purification steps are needed, which limits the amount of work up required and avoids unnecessary loss of yield. Reagents are used in excess, which improves reaction yields and purification by shifting the reaction equilibrium to product formation. Secondary amine protecting groups are not necessary for TACN because the molecule is immobilised on the CTC resin. Recycling of starting materials is also possible and reactions may be performed at room temperature and neutral pH.[74] The disadvantages of SPS include

the small scale that the reactions are limited to and that CTC resin is not stable at elevated temperatures.[73]

A second synthetic strategy to access H_3L^1 was investigated using SPS. The retrosynthetic pathway to obtain H_3L^1 using SPS is outlined in **Scheme 3.1**. Compound **1** could be attached *via* the carboxylate to the CTC resin to produce resin-bound **10**. TACN could then be alkylated with **10** in excess to avoid the need for protecting groups on the secondary amines. **12** could be synthesised using triethyl phosphite and paraformaldehyde, followed by deprotection of the primary amine using hydrazine monohydrate to form **13**. At this stage, conjugation of a model amino acid using Fmoc-based solid-phase peptide synthesis (SPPS) could be performed to generate **14**, followed by hydrolysis of the protected phosphonates using TMSBr. A final cleave of **15** using TFA would yield an amino acid-conjugated H_3L^1.

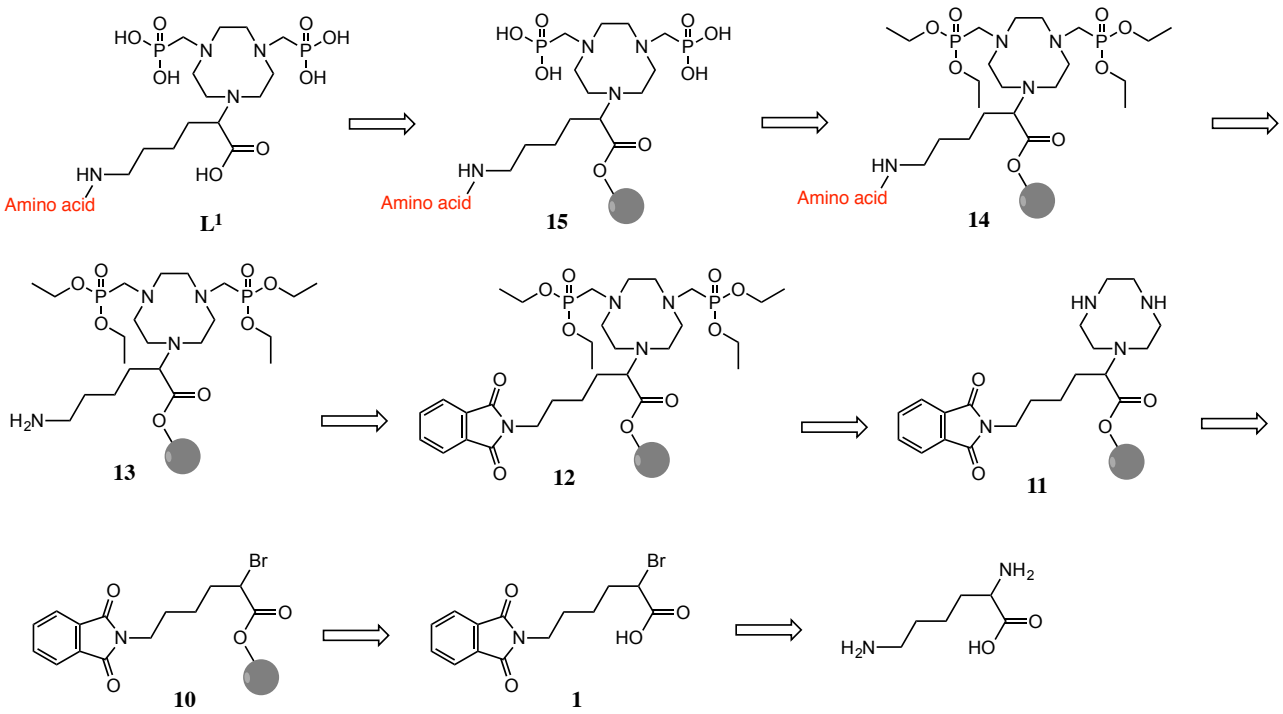

Scheme 3.2: Retrosynthetic pathway to produce H_3L^1 *via* solid-phase synthesis.

3.2 Synthetic Chemistry and Characterisation of Compounds

Compound **1** was attached to freshly regenerated CTC resin. The resin was pre-swelled with DCM. Swelling of the polystyrene material in organic solvents has a high influence on the diffusion and accessibility of reagents to the polymeric core, and thus to the synthetic efficiency of SPS. A solution of **1** in DCM (5 mL) was added to the resin, using DIPEA as a base, in a 12 mL solid-phase reaction vessel. After shaking mechanically overnight, methanol (MeOH) (5 mL) was added as a capping reagent for unreacted CTC. Following further mechanical shaking, the resin was filtered, washed with DCM, isopropanol (*i*PrOH) and MeOH, and dried.

Monitoring of each successive reaction on the resin was achieved using the chloranil test. The chloranil test enables the visualisation of both primary and secondary amines on solid phase by adding 2 – 3 drops of equal volume solutions of 2 % tetrachloro-1,4-benzoquinone (chloranil) in DMF and 2% acetaldehyde in DMF to a small amount of resin. A deep blue colour change to the originally light yellow beads indicates the presence of secondary amines, whilst a bright red colour indicates the presence of primary amines.

Test cleaves were also performed to check each successive reaction on a small amount of resin using a mixture of triisopropylsilane (TIPS, 2.5% v/v), water (2.5% v/v) and TFA (95% v/v) (250 μL total) with shaking for 5 minutes. TIPS and water act as scavengers, and are added during TFA cleavage in order to prevent side reactions with reactive carbocations.[75] TIPS acts as a hydride donor in acidic conditions and reacts with the trityl carbocation formed following cleavage from the CTC resin. The volume of the mixture was reduced by 90% under a steady stream of nitrogen gas and acetonitrile (1 mL) was added. Following centrifugation, the supernatant was removed and an ESI mass spectrum was collected of the resulting solution. The high-resolution ESI mass spectrum of **10** shows successful attachment to the CTC resin (m/z = 340.0020 $[M + H]^+$).

The *N*-monoalkylated TACN derivative **11** was successfully synthesised on resin using an excess of TACN in DCM as observed from the ESI mass spectrum with a peak assigned to the mono-alkylated TACN species (*m/z* = 389.2116 $[M + H]^+$).

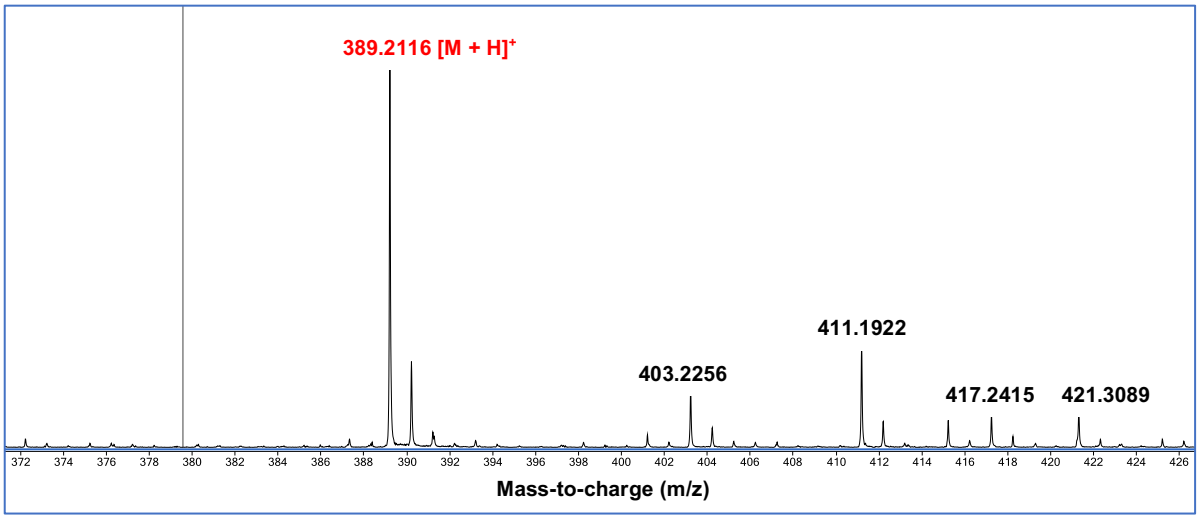

Figure 3.1: ESI mass spectrum of **11**.

The ESI-MS results for compounds **10 - 13** are listed in **Table 3.1**. Compounds **11** and **13** each showed the expected positive chloranil test for the presence of secondary amines. Compound **12** also showed a positive chloranil test that was attributed to incomplete phosphonation reaction, resulting in a mixture of mono- and di-substituted methylene phosphonate groups. The mass spectrometry analysis also showed the presence of both the mono- and di-phosphonylated species (*m/z* = 689.2 and 539.2).

Table 3.1: Results of the ESI-MS spectra of **10** – **13**.

Compound	MS *m/z* $[M + H]^+$	Chloranil test
10	341.1	Positive (blue)
11	389.1	Positive (blue)
12	689.2 (di); 539.2 (mono)	Positive (blue)
13	559.8	Positive (red)

Like the solution-phase synthesis, compound **12** has proven to be quite challenging to synthesise successfully using SPS. Several different reaction conditions have been evaluated including variations to reagent quantities, reaction durations and reaction temperatures in order

to selectively form the di-substituted species (**Table 3.2**). In all cases, paraformaldehyde ($(CH_2O)_n$) and triethyl phosphite ($P(OEt)_3$) were added at the same time. With the exception of the last two entries in **Table 3.2**, where the resin seemingly decomposed due to heat and no products were observed in the ESI mass spectrum, the formation of both the mono- and di-substituted phosphonate was observed (*m/*z = 689.2 and 539.2). This indicates that, unlike the solution-based synthesis, the formation of the intermediate imine was able to occur even though paraformaldehyde and triethyl phosphite were added at the same time.

Table 3.2: Reaction conditions attempted in the formation of **12**.

Entry	Equiv. $P(OEt)_3$	Equiv. $(CH_2O)_n$	Solvent	Temperature	Time
a	6.0	2.0	DMF/THF	25 °C	3 d
b	4.0	4.0	DMF/THF	25 °C	3 d
c	6.0	6.0	DMF/THF	25 °C	3 d
d	8.0	8.0	DMF/THF	25 °C	3 d
e	4.0	4.0	DMF/THF	50 °C	1 d
f	6.0	2.0	DMF/THF	25 °C	7 d
g	8.0	2.0	DMF/THF	25 °C	7 d
h	4.0	4.4	DMF/THF	25 °C	7 d
i	8.0	2.0	DMF/DCM	25 °C	3 d
j	3.0	3.3	DMF	80 °C	1 d
k	4.0	4.4	DMF/DCM	80 °C (MW)	20 min

In recent years, the application of automated microwave (MW) systems in combination with solid-phase chemistry has been used for the synthesis of peptides and small molecules.[76] MW irradiation was evaluated for the di-substitution of the phosphonate. However, this led to a series of uncharacterisable side-products. Despite these attempts and synthetic modifications, a method was not successfully found to selectively form the di-substituted phosphonate, and thus $\mathbf{H_3L^1}$ was unable to be synthesised on resin. Future work should focus on the optimisation of this and subsequent reactions because solid-phase synthesis has the potential to greatly improve the efficiency of bifunctional chelator synthesis.

4 Ga^{3+} Complex Synthesis and Radiochemistry

The triazamacrocyclic compounds NOTA (tri-carboxylic acid) and NOTP (tri-phosphonic acid) (**Figure 1.6**) are known to form highly thermodynamically stable complexes with Ga^{3+}. In addition, the incorporation of the carboxylates and phosphonates, respectively, has permitted $^{68}Ga^{3+}$ radiochemical complexation to take place at neutral pH, room temperature and at low chelator concentrations, important requirements for radiopharmaceutical synthesis. The properties of the solution-based complexes of [Ga(NOTA)] and [Ga(NOTP)] such as thermodynamic and kinetic stabilities have been reported previously.[51] Additionally, the X-ray crystal structure of the neutral complex, [Ga(NOTA)] has been previously reported with the complex exhibiting a distorted octahedral coordination environment around the Ga^{3+} ion.[51]

To the best of our knowledge, the X-ray crystal structure of a Ga^{3+} complex with NOTP has not previously been reported. A comparison of the solid-state structures of NOTA and NOTP with Ga^{3+} will aid in understanding their properties and those of mixed phosphonate-carboxylate chelator $\mathbf{H_3L^1}$. The reaction of commercially available NOTP with $Ga(NO_3)_3$ in water and 5% aqueous NH_3 (final pH ~2 – 3) led to the formation of a colourless complex (*m/z* = 477.9 $[[Ga(NOTP)] + H]^+$). Crystals suitable for X-ray analysis were obtained by slow evaporation of the aqueous solution.

4.1 Description of the Crystal Structure of 1,4,7-Triazacyclononane-1,4,7-tri(methylenephosphonato)gallium(III) ([Ga(NOTP)])

The neutral complex [Ga(NOTP)] crystallised in the monoclinic space group $P2_1/n$, in which the coordination geometry of the Ga^{3+} cation is distorted octahedral with N_3O_3 donor atoms. Experimental, crystallographic and refinement data for the complex are outlined in **Table 4.1**.

Table 4.1: Experimental, crystallographic, and refinement data for [Ga(NOTP)].

Parameter	[Ga(NOTP)]	Parameter	[Ga(NOTP)]
Formula	$C_9H_{21}GaN_3O_9P_3$	Volume (Å^3)	1612.71(19)
Formula weight	477.92	Z	4
Temperature (K)	123(2)	D_c (g cm^{-3})	1.968
Colour	colourless	Absorption coefficient (mm^{-1})	2.058
Wavelength (Å)	0.71073	$F(000)$	976
Crystal system	Monoclinic	Crystal size (mm)	0.25 x 0.25 x 0.25
Space group	$P2_1/n$	θ range for data collection (°)	3.42 – 30.66
Unit cell dimensions		Total reflections collected	21175
a (Å)	9.4481(7)	Independent reflections [R_{int}]	4588 [0.0374]
b (Å)	13.9640(8)	Goodness-of-fit on F^2	1.069
c (Å)	12.6178(8)	Final R indices [$I > 2\sigma(I)$]	$R_1 = 0.0256$
α (°)	90		$wR_2 = 0.0669$
β (°)	104.358(7)	R indices (all data)	$R_1 = 0.0301$
γ (°)	90		$wR_2 = 0.0698$

A molecular diagram of the X-ray crystal structure of [Ga(NOTP)] is shown in **Figure 4.1**, and relevant bond lengths and angles are summarised in **Table 4.2**. Ga^{3+} is bound to the three amine nitrogen atoms of the triazacyclononane macrocycle and to three deprotonated phosphonato oxygen atoms, which project on the same side of the ring. The three amine nitrogen atoms occupy the facial set of sites in a distorted octahedral geometry, and all three *trans* N-Ga-O angles are approximately 169° due to the intrinsically small bite angle of the adjacent five-membered chelate rings. The triangular face comprising the oxygen atoms is larger (average angle O-Ga-O = 96°) than that comprising the nitrogen atoms (average angle N-Ga-N = 83°). This causes a relative twist of the two planes defined by N(1), N(2), N(3) (N_3 plane) and O(1), O(4), O(7) (O_3 plane) by approximately 11° along the pseudo C_3 axis away from a symmetrically staggered confirmation. The Ga^{3+} ion is shifted slightly towards the O_3 plane (Ga(1)-O_3 plane distance = 1.00 Å; Ga(1)-N_3 plane distance = 1.37 Å) (**Figure 4.2**).

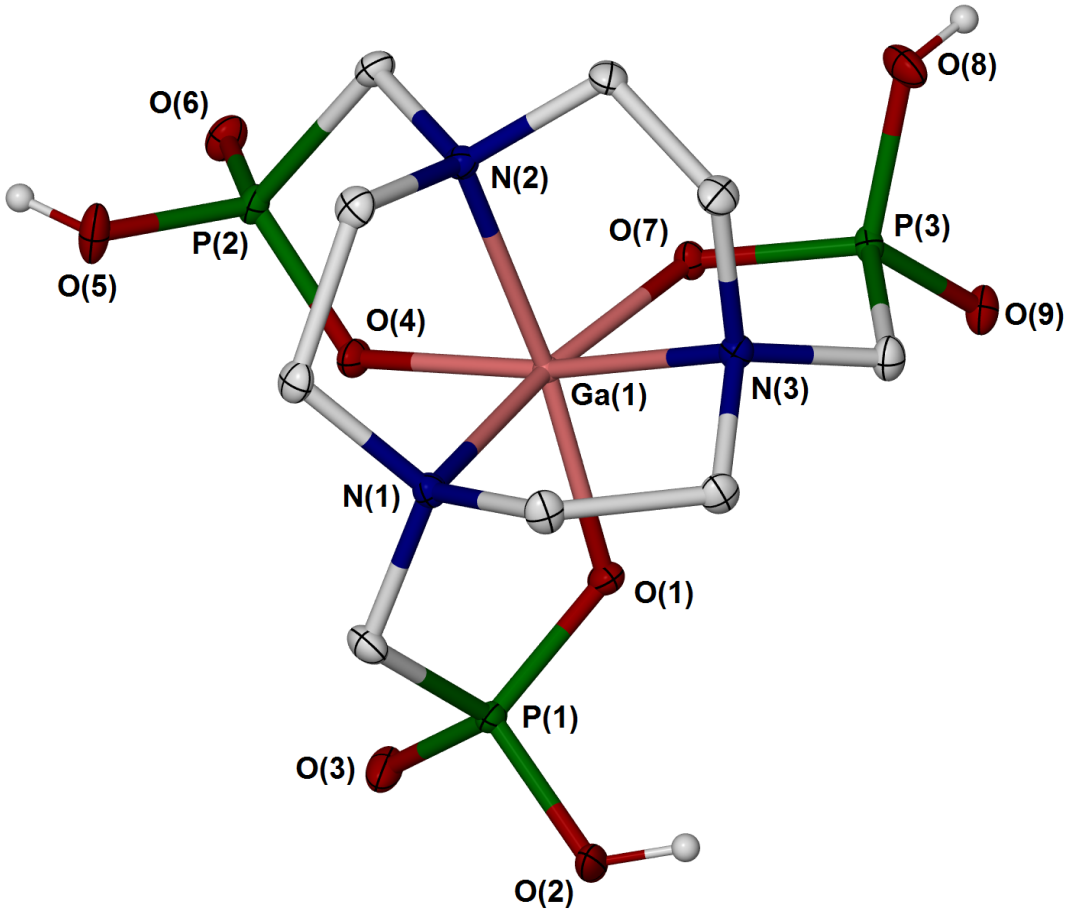

Figure 4.1: Molecular diagram of the X-ray crystal structure of [Ga(NOTP)]. Ellipsoids are shown at 50% probability (non-hydrogen atoms). Some hydrogen atoms have been omitted for clarity. Selected bond lengths (Å): **Ga(1)-O:** O(1) 1.9106(11), O(4) 1.9291(11), O(7) 1.9390(11); **Ga(1)-N:** N(1) 2.1451(13), N(2) 2.0968(13), N(3) 2.1300(13).

Table 4.2: Selected molecular dimensions (bond lengths in Å and angles in °) for [Ga(NOTP)].

Bond lengths			
Ga(1)-O(1)	1.9106(11)	Ga(1)-N(2)	2.0968(13)
Ga(1)-O(4)	1.9291(11)	Ga(1)-N(3)	2.1300(13)
Ga(1)-O(7)	1.9390(11)	Ga(1)-N(1)	2.1451(13)
Bond angles			
O(1)-Ga(1)-O(4)	94.83(5)	O(7)-Ga(1)-N(3)	85.94(5)
O(1)-Ga(1)-O(7)	93.69(5)	N(2)-Ga(1)-N(3)	83.53(5)
O(4)-Ga(1)-O(7)	98.29(5)	O(1)-Ga(1)-N(1)	86.43(5)
O(1)-Ga(1)-N(2)	169.79(5)	O(4)-Ga(1)-N(1)	93.62(5)
O(4)-Ga(1)-N(2)	85.86(5)	O(7)-Ga(1)-N(1)	168.03(5)
O(7)-Ga(1)-N(2)	96.30(5)	N(2)-Ga(1)-N(1)	83.36(5)
O(1)-Ga(1)-N(3)	95.07(5)	N(3)-Ga(1)-N(1)	82.13(5)
O(4)-Ga(1)-N(3)	168.95(5)		

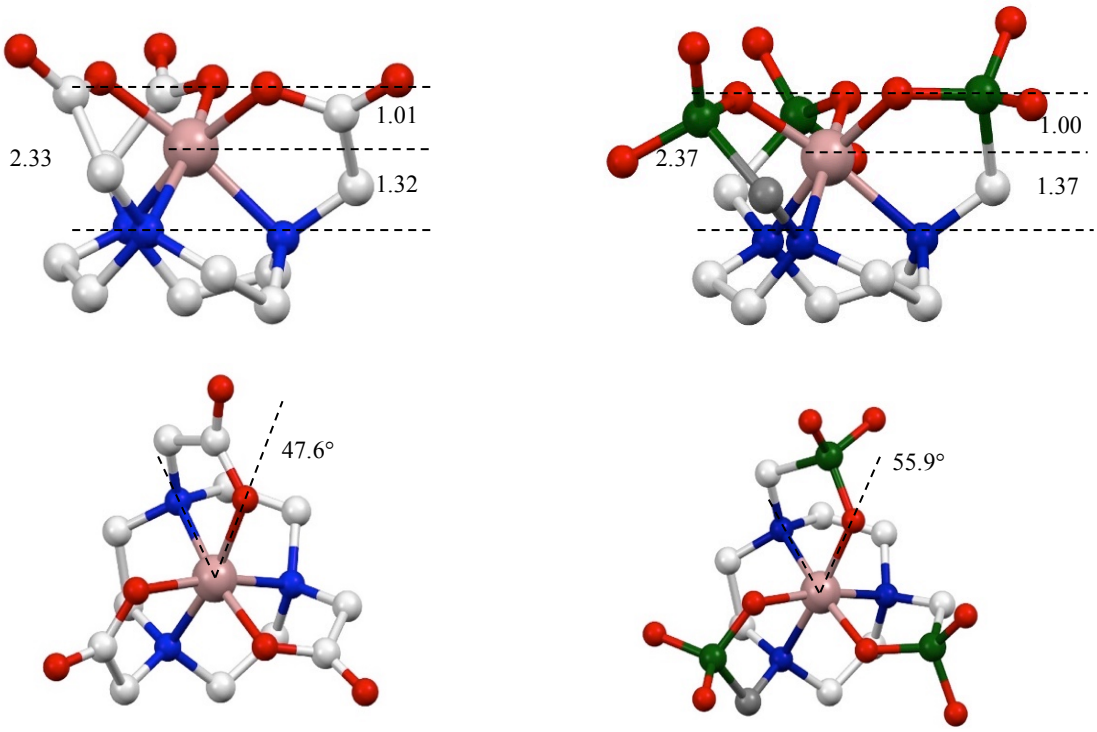

Figure 4.2: Comparison of the X-ray molecular structures of [Ga(NOTA)] and [Ga(NOTP)]. Distances are in Å. Angles given are torsion angles of the pseudo-octahedral coordination environments. Colour scheme: C, white; N, blue; P, green; O, red; Ga, pink.

The average torsion angle of a six-coordinate complex can help to define its coordination geometry as existing somewhere between octahedral and trigonal prismatic.[77] The position of a centroid (Cen) can be calculated between the three atoms of each trigonal face, in this case the O_3 and N_3 planes. The torsion angle is then defined as the dihedral angle formed between O-Cen_{O3}-Cen_{N3}-N, where O and N belong to the same five-membered chelate ring. A torsion angle of 0° indicates an ideal trigonal prismatic geometry, 60° indicates an ideal octahedral geometry, and 30° is a geometry half-way between the two (**Figure 4.3**). The three torsion angles for [Ga(NOTP)] are 53.3°, 50.8° and 52.2°, with an average torsion angle of 52.1°. This indicates that the coordination geometry of [Ga(NOTP)] is distorted octahedral. The pendant phosphonato arms adopt a chiral right- (Δ) or left-handed (Λ) three-blade propeller-like layout,

which imposes the same conformation to each of the three five-membered chelate rings belonging to the triazacyclononane macrocycle. According to the nomenclature introduced by Corey and Bailar (δ for a positive sign for the N-C-C-N dihedral angle and λ for a negative sign), the triazamacrocycle can exist as either the clockwise (δ,δ,δ) or anti-clockwise (λ,λ,λ) enantiomeric forms.[78] Examining the crystal lattice, it appears that two discrete enantiomers, Δλλλ-SSS and Λδδδ-RRR, are present as a racemate within the unit cell (**Figure 4.3**).

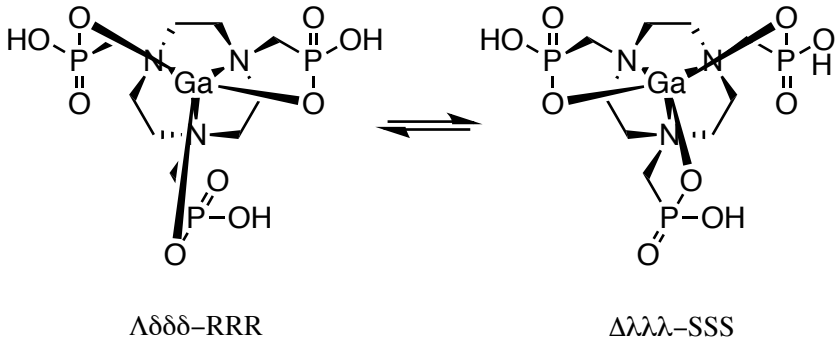

Λδδδ–RRR Δλλλ–SSS

Figure 4.3: Schematic representation of the Δλλλ-SSS and Λδδδ-RRR enantiomeric forms of [Ga(NOTP)] viewed down the C_3 axis.

The complex displays intermolecular hydrogen bonding motifs. The three pendant phosphonato P=O groups on each complex form hydrogen bonds with the protonated O-H groups on an adjacent complex, forming 2D hydrogen-bonded sheets (**Figure 4.4**). The hydrogen bond distances between the O-H hydrogen donor and the P=O oxygen acceptor atoms are 2.5314(17) Å (O(2)-H(2)····O(9)), 2.5108(18) Å (O(5)-H(5)····O(3)), and 2.4862(17) Å (O(8)-H(8)····O(6)) (**Table 4.3**).

Table 4.3: Hydrogen bond lengths (Å) and angles (°) for [Ga(NOTP)] (D = hydrogen-bond donor; A = hydrogen-bond acceptor).

D-H····A	d (D-H)	d (H····A)	d (D····A)	< (DHA)
O(2)-H(2)····O(9) #1	0.81(3)	1.73(3)	2.5314(17)	174(3)
O(5)-H(5)····O(3) #2	0.75(3)	1.76(3)	2.5108(18)	178(4)
O(8)-H(8)····O(6) #3	0.79(3)	1.72(3)	2.4862(17)	167(3)

Symmetry transformations used to generate equivalent atoms: #1: -x+1, -y, -z+1; #2: -x+1, -y+1, -z+1; #3: -x+1/2, y-1/2, -z+3/2

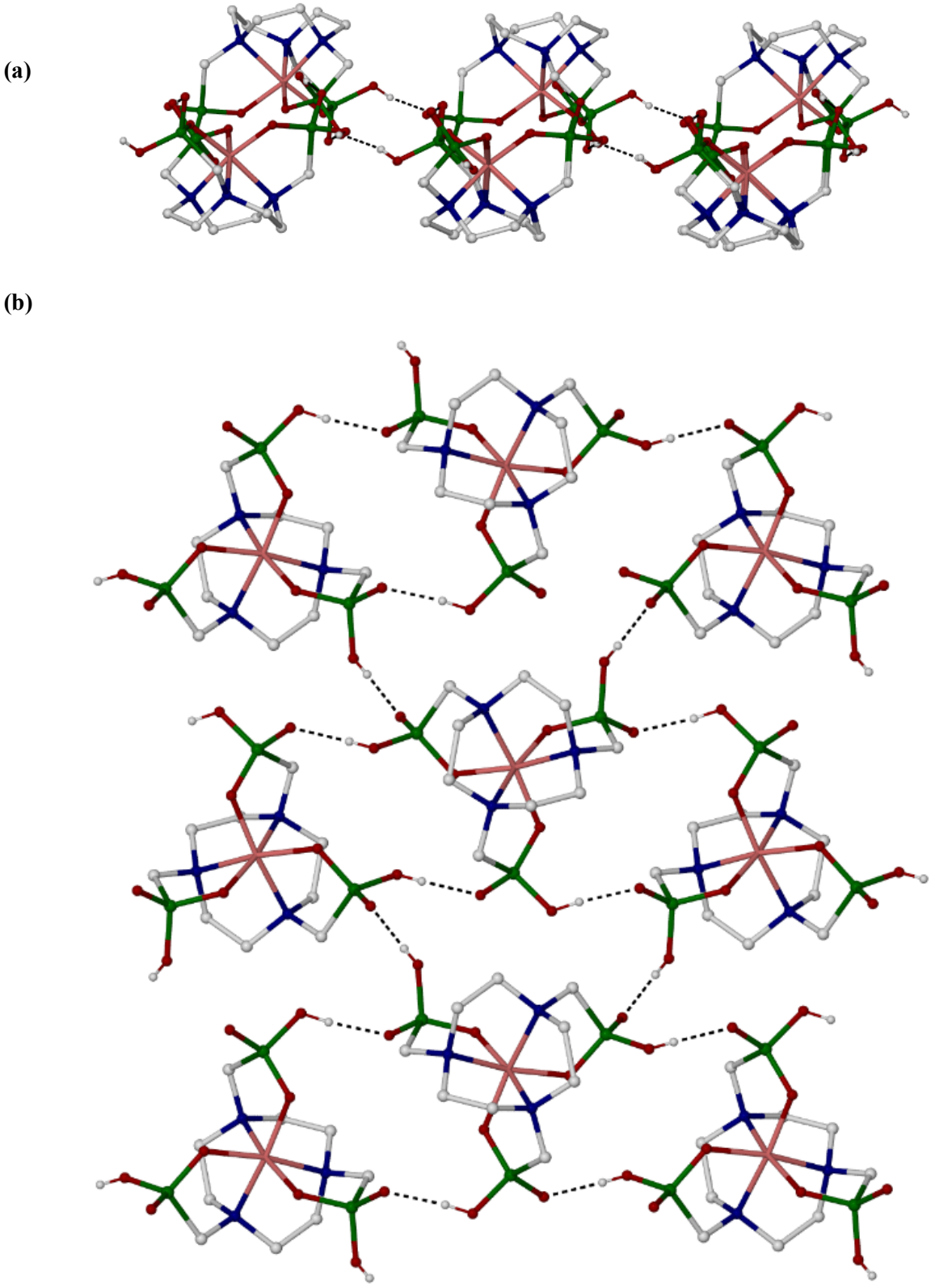

Figure 4.4: Molecular packing in **[**Ga(NOTP)] with H-bonds shown as black dashes. Molecules of [Ga(NOTP)] form 2D hydrogen-bonded sheets (a) top view (b) side view. All CH hydrogen atoms omitted for clarity. Symmetry transformations used to generate equivalent atoms: #1 -x+1, -y, -z+1; #2 -x+1, -y+1, -z+1; #3 -x+1/2, y-1/2, -z+3/2. Atom colour scheme: C, white; N, blue; P, green; O, red; Ga, pink.

4.2 Radiolabelling of NOTP

Radiolabelling of NOTP with ^{68}Ga was undertaken and analysed using reverse-phase high-performance liquid chromatography (RP-HPLC). ^{68}Ga was eluted from a ^{68}Ge/^{68}Ga generator using 0.1 M aqueous HCl and the eluate was collected. ^{68}Ga (10 μL, approx. 1.2 MBq in 0.1 M aqueous HCl) was added to an aqueous solution of NOTP (100 μL, 0.2 M ammonium acetate, pH 6 – 7) and the solution was incubated at 25 °C for 10 min. The radiochromatogram of [^{68}Ga][Ga(NOTP)] is shown in **Figure 4.5**. A single peak was observed in the radiochromatogram with a retention time of 10.21 min that was assigned to [^{68}Ga][Ga(NOTP)]. The radiochemical yield of [^{68}Ga][Ga(NOTP)] was high (>95%) as determined by radio-HPLC, with an apparent molar activity of 0.5 MBq/nmol at the time of synthesis. Apparent molar activity is a measure of radioactivity that takes into account the moles of non-radioactive components (NOTP) into the calculation of radioactivity.

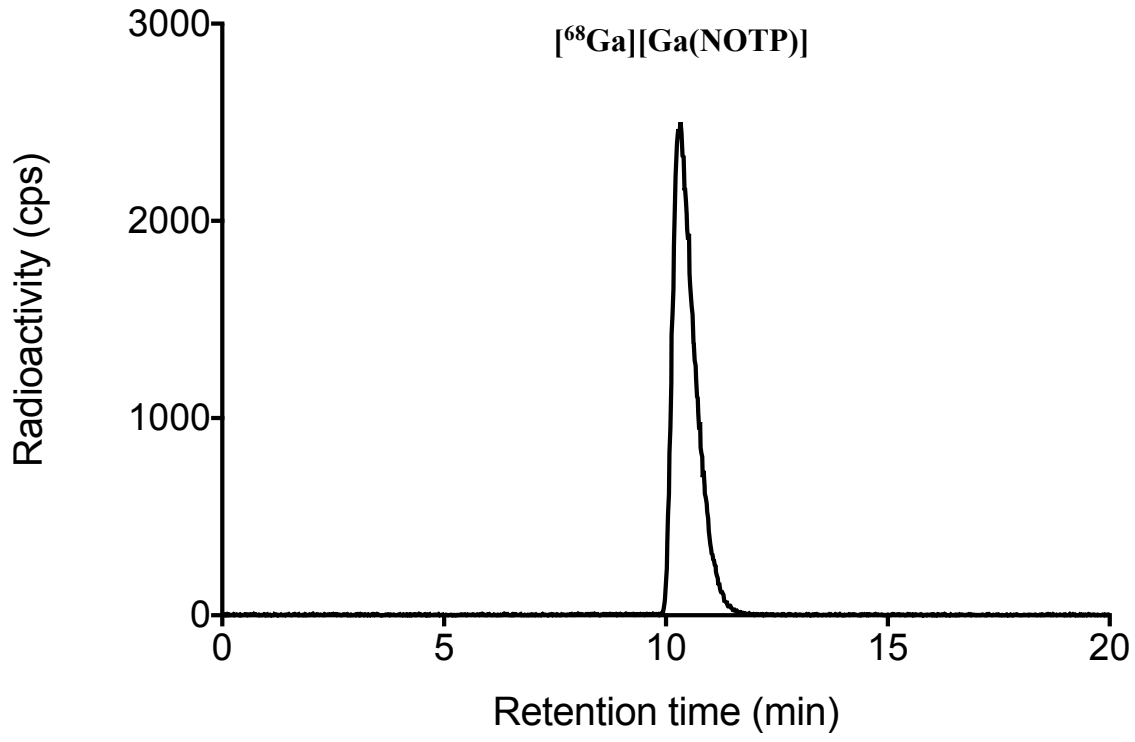

Figure 4.5: Size exclusion radio-HPLC trace of [^{68}Ga][Ga(NOTP)].

5 Conclusions and Future Work

Using traditional solution-based synthetic methods, several key intermediates in the synthesis of the bifunctional chelator **H_3L^1** were successfully produced and characterised. Additionally, there is evidence to suggest that the solid-phase synthesis of **H_3L^1** is a viable alternative to traditional solution-based methods, with ESI-MS data highlighting that intermediates can be synthesised on resin. The key synthesis of the di-ethyl phosphonate intermediate was successfully synthesised in solution, however there were issues with incomplete conversion on solid-phase. A mixture of the mono- and di-substituted species was present after several synthetic modifications.

In solution, the final three steps of the synthesis of **H_3L^1** are the following: firstly, to deprotect the primary amine by cleaving the phthalimide group using hydrazine monohydrate in a Gabriel-like reaction;[79] secondly, to perform a hydrogenation on the benzyl ester to reform the carboxylic acid and; thirdly, to hydrolyse the protected phosphonates to access two phosphonic acids. Additionally, future work would include forming the Ga^{3+} complex of **H_3L^1** as well as the radioactive analogue using $^{68}Ga^{3+}$.

The radiochemical synthesis and solid-state characterisation of [Ga(NOTP)] was successfully undertaken. The X-ray crystal structure of the neutral distorted octahedral complex, [Ga(NOTP)], indicates two discrete enantiomers, Δλλλ-SSS and Λδδδ-RRR, are present as a racemate within the unit cell. [Ga(NOTP)] presents an opportunity in future experiments to compare the coordination chemistry of **H_3L^1** with Ga^{3+} as an aid to understanding the chemistry behind the mixed carboxylate-phosphonate bifunctional chelator as a potential radiopharmaceutical.

6 Experimental Details

6.1 General Procedures

Reagents were purchased from standard commercial sources unless otherwise stated. NOTP was purchased from Macrocyclics, Inc. (TX, USA). 2-Chlorotrityl chloride resin was purchased from GL Biochem (China) and freshly regenerated according to a literature procedure.[73] Unless specified, all reagents were used as supplied without further purification. High temperature reactions were carried out in paraffin oil baths controlled by temperature probes. Reduced pressure/*in vacuo* means 50 – 850 mbar under rotary evaporation at 60 °C. Thin layer chromatography was performed on aluminium plates and visualised under 254 nm UV light. Flash chromatography was performed on silica gel. Solid-phase synthesis was carried out in solid-phase reaction vessels (12 mL or 24 mL) that were purchased from Torvig (AZ, USA). Monitoring of secondary amines on solid-phase was performed by staining beads of resin with solutions of 2% chloranil (tetrachloro-1,4-benzoquinone) in DMF and 2% acetaldehyde in DMF. A blue colour staining of the beads indicated a positive test.

6.2 General Analytical Details

Infrared spectroscopy was carried out using an Agilent Cary 630 ATR-FTIR spectrometer. Nuclear magnetic resonance spectroscopy was carried out using Bruker spectrometers: either an AVANCE III 600 (^{1}H at 600.27 MHz, ^{13}C{^{1}H} at 150.95 MHz) or AVANCE III 400 (^{1}H at 400.13 MHz). Spectra were processed using MestReNova 10.0 software. Deuterated solvents ($CDCl_3$, acetone-d_6) were obtained from Merck and Cambridge Isotope Laboratories Inc. Chemical shifts (δ) are reported in parts per million (ppm) with respect to residual solvent peaks for ^{1}H and ^{13}C{^{1}H} and $CFCl_3$ for ^{19}F{^{1}H} NMR spectra. Signal splitting was reported as: s = singlet, d = doublet, t = triplet, dd = doublet of doublets, etc. Coupling constants (*J*) are reported in Hz. Integrals are relative. Unless specified, all NMR spectra were recorded at 25 °C. Low

resolution mass spectrometry (MS) was carried out using an Agilent 1260 Infinity liquid chromatograph system coupled with 6120 series quadrupole mass spectrometer in MeOH or acetonitrile using electrospray ionisation (ESI). High resolution mass spectrometry (HRMS) was carried out with an Agilent 6540 UHD Accurate Mass Q-TOF LCMS. The mass spectrometer is fitted with the Agilent Jet Stream Source, using ESI. Reference mass correction was undertaken using reference compound purine/HP0921 mix. Positive or negative detection is shown by the charge on the ion, *e.g.* $[M + H]^+$ for a positive protonated ion and $[M – H]^-$ for a negative deprotonated ion. Radiolabelling of NOTP with ^{68}Ga was undertaken and analysed using reverse-phase high performance liquid chromatography (RP-HPLC). ^{68}Ga was eluted from a titanium dioxide-based ^{68}Ge/^{68}Ga generator (Eckhert Ziegler) using aqueous HCl (0.1 M, 5 mL) and the eluate was collected in 5 x 1 mL fractions. Aliquots of the fourth fraction (1 mL, containing 144 MBq ^{68}Ga) were used directly for radiolabelling. ^{68}Ga (10 μL, approx. 1.2 MBq in 0.1 M aqueous HCl) was added to an aqueous solution of NOTP (100 μL, 0.2 M ammonium acetate, pH 6 – 7) and the solution was incubated at 25 °C for 10 min. The solution (10 μL) was added to an aqueous sodium phosphate solution (500 μL, 0.150 M). Radio-HPLC traces were acquired using a Shimadzu HPLC system with an Agilent AvanceBio size-exclusion column (4.6 mm x 300 mm x 2.7 μm), a 0.35 mL min^{-1} flow rate isocratic elution of 0.150 M phosphate buffer at 25 °C with UV spectroscopic detection at 220 nm. Data were processed and analysed using Laura radiochromatography software (LabLogic).

6.3 Crystallographic Data Collection and Structure Refinements

Low-temperature single-crystal X-ray diffraction experiments were performed using an OXFORD Gemini diffractometer fitted with a CCD detector and using Mo-Kα radiation (λ 0.071073 Å). Crystals were quench-cooled to 123(3) K. The data were collected and processed

using the proprietary software CrysAlis PRO v1.171.38.43d.[80] The structure was solved and refined by conventional methods using the SHELX-2018 software.[81]

6.4 Solution-Phase Synthesis

6.4.1 2-Bromo-6-(1,3-dioxoisoindolin-2-yl)hexanoic acid (1)

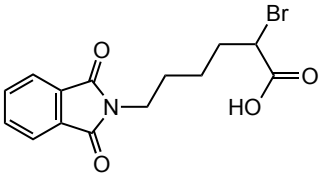

A solution of L-lysine monohydrochloride (7.01 g, 38.4 mmol, 2 equiv.) in 100 mL of water was treated with $CuSO_4 \cdot 5H_2O$ (4.79 g, 19.2 mmol, 1 equiv.). After stirring for 30 min, the pH was adjusted to 9 with 5M KOH (10 mL) and *N*-carbethoxyphthalimide (8.42 g, 38.4 mmol, 2 equiv.) was added. The pH was maintained between 9 – 10 by the addition of 5 M KOH (13 mL) and the solution was left to stir overnight. The pH was adjusted to 0.4 by the addition of 48% HBr (10 mL) and any remaining precipitate was removed by filtration. The filtrate was cooled to <5 °C, and treated with further HBr (15 mL) and KBr (10.98 g, 92.2 mmol, 4.8 equiv.). The mixture was treated dropwise over 1 h with a solution of $NaNO_2$ (5.15 g, 74.9 mmol, 3.9 equiv.) in water (50 mL) while maintaining the temperature at < 5°C. The mixture was stirred at <5 °C for 1 h and then allowed to warm to room temperature and stirred overnight. The resulting precipitate was collected by filtration, dissolved in ethyl acetate (150 mL) and the solution was washed with water (2 x 50 mL) and brine (35 mL), dried with Na_2SO_4 and taken to dryness *in vacuo* to produce a white powder (12.61 g, 37.10 mmol, 97%). **IR(ATR)** ν_{max} 3162m, 3100m (O-H), 2935m, 2862m (C-H), 1767m, 1731s, 1677s (C=O), 720s (C-Br) cm^{-1}; **^{1}H NMR** (600 MHz, $CDCl_3$): δ = 1.36 – 1.55 (m, 2H, C*H*$_2$), 1.64 – 1.70 (m, 2H, C*H*$_2$), 1.95 – 2.11 (m, 2H, C*H*$_2$), 3.64 (t, 2H, C*H*$_2$, $^3J_{HH}$ = 7.3 Hz), 4.17 (t, 1H, C*H*, $^3J_{HH}$ = 7.3 Hz), 7.65 (m, 2H, Ar*H*), 7.77 (m, 2H, Ar*H*); **^{13}C{^{1}H} NMR** (150 MHz, $CDCl_3$): δ = 24.5, 27.8, 34.1, 37.6 (*C*H$_2$), 45.0 (*C*H), 123.3, 132.1, 134.0 (C_{arom}), 168.5 (*C*OOH), 173.5 (*C*=O); **LRMS** (ESI) *m/z* = 340.2 [M + H]$^+$; **HRMS** (ESI) *m/z* = 340.0020 [M + H]$^+$ (experimental), 340.0179 (calcd).

6.4.2 Benzyl 2-bromo-6-(1,3-dioxoisoindolin-2-yl)hexanoate (2)

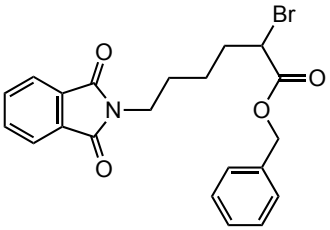

To a solution of *N*-*N*'-dicyclohexylcarbodiimide (DCC, 1.59 g, 7.72 mmol, 1.05 equiv.) and 4-dimethylaminopyridine (DMAP, 0.09 g, 0.74 mmol, 0.1 equiv.) in DCM (30 mL) was added **1** (2.50 g, 7.35 mmol, 1 equiv.) and benzyl alcohol (0.84 mL, 8.09 mmol, 1.1 equiv.). The opaque, white mixture was stirred overnight in the dark at room temperature. The suspension was filtered and the filtrate was concentrated *in vacuo* to produce a pale-yellow oil. The oil was purified by silica gel chromatography with ethyl acetate/hexane (5:1) to obtain a colourless oil (2.99 g, 6.95 mmol, 95%). $\boldsymbol{R_f}$ 0.73 (ethyl acetate-hexane, 5:1); **IR(ATR)** ν_{max} 2937m, 2865m (C-H), 1736m, 1707s (C=O), 718s (C-Br) cm^{-1}; **^{1}H NMR** (600 MHz, $CDCl_3$): δ = 1.31 – 1.47 (m, 2H, C*H*$_2$), 1.59 – 1.67 (m, 3H, C*H*$_2$), 1.98 – 2.09 (m, 1H, C*H*$_2$), 3.59 (t, 2H, OC*H*$_2$, $^3J_{HH}$ = 7.28 Hz), 4.17 (dd, 1H, C*H*, $^3J_{HH}$ = 6.68, 7.92 Hz), 5.12 (2H, m, OC*H*$_2$), 7.29 (m, 5H, OAr*H*), 7.61 – 7.65 (m, 2H, Ar*H*), 7.76 – 7.78 (m, 2H, Ar*H*); **^{13}C{^{1}H} NMR** (150 MHz, $CDCl_3$): δ = 24.5, 27.8, 34.3, 37.5 (*C*H$_2$), 45.5 (*C*H), 67.6 (O*C*H$_2$), 123.2 (*C*$_{arom}$), 128.2, 128.3, 128.4, 128.5, 128.6, 128.7 (O*C*$_{arom}$), 134.0 (*C*$_{arom}$), 168.4 (O*C*=O), 169.5 (C=O); **LRMS** (ESI) *m/z* = 452.0 $[M + Na]^+$; **HRMS** (ESI) *m/z* = 430.0631 $[M + H]^+$ (experimental), 430.0648 (calcd).

6.4.3 Di-tert-butyl 1,4,7-triazacyclononane-1,4-dicarboxylate (diBocTACN)

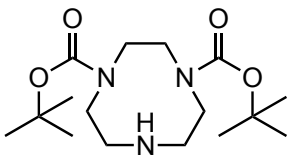

To a solution of 1,4,7-triazacyclononane (4.50 g, 35.01 mmol, 1 equiv.) in $CHCl_3$ (120 mL) was added triethylamine (14.08 mL, 101.00 mmol, 2.9 equiv.). A solution of 2-(*tert*-butoxycarbonyloxyimino)-2-phenylacetonitrile (Boc-ON, 17.24 g, 70.02 mmol, 2 equiv.) in $CHCl_3$ (150 mL) and added dropwise to the stirring solution over 30 min. The mixture was then stirred for 2 h at room temperature, and concentrated *in vacuo* to afford a yellow oil. The yellow oil was dissolved in ethyl acetate (250 mL) and washed with 4% $NaHCO_3$ (100 mL), brine (100 mL) and 10% citric

acid solution (3 x 150 mL), whereupon the desired product moved to the aqueous phase. To the aqueous fraction was added NaOH (approx. 5 g) under ice cooling until the pH was adjusted to 10. The product was extracted from the turbid solution with $CHCl_3$ (3 x 300 mL). The organic fractions were dried over Na_2SO_4 and concentrated *in vacuo* to produce diBocTACN as a yellow oil (10.35 g, 31.34 mmol, 90%). **IR(ATR)** ν_{max} 2975m (N-H), 2931m (C-H), 1678s (C=O), 1460m (CH_3 cm^{-1}; **^{1}H NMR** (600 MHz, $CDCl_3$): δ = 1.41 (s, 18H, C*H*$_3$(*t*-Bu)), 2.87 (m, 4H, C*H*$_2$ macrocycle), 3.19 (m, 4H, C*H*$_2$ macrocycle), 3.40 (m, 4H, C*H*$_2$ macrocycle); **^{13}C{^{1}H} NMR** (150 MHz, $CDCl_3$): δ = 26.5 (*t*-Bu(*C*H$_3$), 47.3, 47.6, 49.6, 49.8, 51.6, 52.4 (*C*H$_2$ macrocycle), 79.7, 79.9 (*C*CH$_3$(*t*-Bu)), 155.8, 156.0 (*C*=O); **LRMS** (ESI) *m/z* = 330.3 [M + H]$^+$; **HRMS** (ESI) *m/z* = 330.2378 [M + H]$^+$ (experimental), 330.2348 (calcd).

6.4.4 Di-*tert*-butyl 7-(1-(benzyloxy)-6-(1,3-dioxoisoindolin-2-yl)-1-oxohexan-2-yl)-1,4,7-triazacyclononane-1,4-dicarboxylate (3)

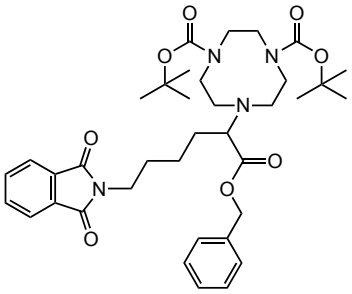

To a solution of diBocTACN (1.42 g, 4.31 mmol, 1 equiv.) in acetonitrile (30 mL) at 0 °C was added K_2CO_3 (0.60 g, 4.31 mmol, 1 equiv.). A solution of **2** (1.85 g, 4.31 mmol, 1 equiv.) in acetonitrile (50 mL) was then added dropwise at 0 °C. The reaction was warmed to room temperature and stirred for 12 h. The temperature was raised to 50 °C and the reaction mixture was stirred for a further 2 d. The suspension was filtered and the pale-yellow solution was dried over $MgSO_4$ and concentrated *in vacuo* to obtain a pale-yellow oil (2.35 g, 3.46 mmol, 80%). **^{1}H NMR** (600 MHz, $CDCl_3$): δ = 1.36 (m, 2H, C*H*$_2$), 1.41 – 1.44 (m, 18H, C*H*$_3$(*t*-Bu)), 1.62 (m, 2H, C*H*$_2$), 2.15 (m, 2H, C*H*$_2$), 2.70 – 2.87 (m, 4H, C*H*$_2$ macrocycle), 3.18 – 3.29 (m, 4H, C*H*$_2$ macrocycle), 3.42 – 3.46 (m, 4H, C*H*$_2$ macrocycle), 3.56 – 3.60 (m, 2H, C*H*$_2$), 4.17 (s, 1H, C*H*), 5.01 – 5.15 (m, 2H, OC*H*$_2$), 7.27 – 7.30 (m, 5H, OAr*H*), 7.62 – 7.65 (m, 2H, Ar*H*), 7.75 – 7.77 (m, 2H, Ar*H*); **^{13}C{^{1}H} NMR** (150 MHz, $CDCl_3$):

δ = 25.9 (*C*H_2), 26.7 (*C*H_3-(*t*-Bu)), 28.3, 32.4, 35.8 (*C*H_2), 43.6 (*C*H), 47.6, 47.8, 49.7, 50.0, 50.6, 50.8 (*C*H_2 macrocycle), 65.7 (O*C*H_2), 79.7 (*C*CH_3(*t*-Bu)), 125.1, 125.7 (C_{arom}), 126.3, 126.4, 126.5, 126.6, 126.7 (OC_{arom}), 132.1 (C_{arom}), 166.5 (*C*=O), 167.6 (*C*=O(*t*-Bu), 171.4 (O*C*=O); **LRMS** (ESI) *m/z* = 679.3 $[M + H]^+$; **HRMS** (ESI) *m/z* = 679.3698 $[M + H]^+$ (experimental), 679.3701 (calcd).

6.4.5 [7-(1-(benzyloxy)-6-(1,3-dioxoisoindolin-2-yl)-1-oxohexan-2-yl)-1,4,7-triazacyclononane-1,4-diium]-bis(trifluoroacetate) (4)

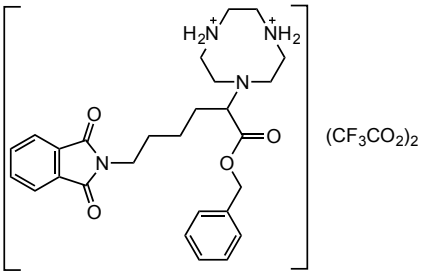

To a solution of **3** (1.01 g, 1.49 mmol) in DCM (10 mL) was added 50% v/v DCM/TFA (15 mL) at 0 °C and the golden yellow solution was stirred for 0.5 h. The solution was sparged with nitrogen gas to remove TFA, after which it was concentrated *in vacuo*. Diethyl ether (20 mL) was added to the crude mixture, which was then concentrated *in vacuo* to produce a dark-yellow oil (1.72 g). **^{1}H NMR** (400 MHz, methanol-d_4): δ = 1.34 – 1.50 (m, 2H, CH_2), 1.64 – 1.77 (m, 2H, CH_2), 1.77 – 2.09 (m, 2H, CH_2), 3.02 – 3.27 (m, 2H, CH_2 macrocycle), 3.33 – 3.35 (m, 6H, CH_2 macrocycle), 3.36 – 3.47 (m, 2H, CH_2 macrocycle), 3.58 – 3.66 (m, 2H, CH_2), 3.66 – 3.76 (m, 2H, TACN ring), 4.61 (s, 1H, C*H*), 5.11 – 5.29 (m, 2H, OCH_2), 7.24 – 7.39 (m, 5H, OAr*H*), 7.73 – 7.90 (m, 4H, Ar*H*); **^{13}C{^{1}H} NMR** (100 MHz, methanol-d_4): δ = 24.3, 27.5, 29.9, 33.4 (*C*H_2) 42.9 (*C*H), 44.4, 46.8, 48.2 (*C*H_2 macrocycle), 65.5 (O*C*H_2), 115.6 (q, *C*F_3, $^1J_{CF}$ = 188 Hz), 122.7, 126.6, 126.8 (C_{arom}), 127.9, 128.1, 128.2, 128.3 (OC_{arom}), 134.0 (C_{arom}), 159.8 (q, *C*=O, $^2J_{CF}$ = 25 Hz), 168.5 (*C*=O), 174.0 (O*C*=O); **^{19}F{^{1}H} NMR** (376 MHz, methanol-d_4): δ -72.9; **LRMS** (ESI) *m/*z = 479.2 $[M + H]^+$; **HRMS** (ESI) *m/z* = 479.2648 $[M + H]^+$ (experimental), 479.2653 (calcd).

6.4.6 Benzyl 6-(1,3-dioxoisoindolin-2-yl)-2-(1,4,7-triazacyclononan-1-yl)hexanoate (5)

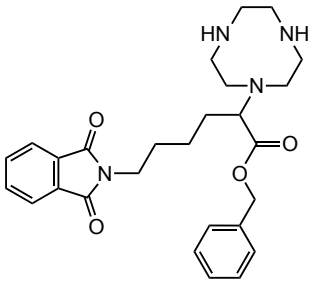

To a solution of **4** (1.72 g, 2.43 mmol) in 5:1 H_2O/MeOH (100 mL) was slowly added 1 M NaOH until the pH of the solution was adjusted to 9 – 10. The turbid mixture was extracted with $CHCl_3$ (2 x 100 mL), the combined organic layers were washed with brine, dried over $MgSO_4$ and concentrated *in vacuo* to produce a pale-yellow oil (0.77 g, 1.61 mmol, 66%). **^{1}H NMR** (600 MHz, $CDCl_3$): δ = 1.32 – 1.37 (m, 2H, C*H*$_2$), 1.60 – 1.62 (m, 2H, C*H*$_2$), 1.98 – 2.04 (m, 2H, C*H*$_2$), 2.57 – 2.69 (m, 4H, C*H*$_2$ macrocycle), 2.70 – 2.82 (m, 4H, C*H*$_2$ macrocycle), 2.89 – 3.08 (m, 4H, C*H*$_2$ macrocycle), 3.50 – 3.60 (m, 2H, C*H*$_2$), 4.13 – 4.17 (m, 1H, C*H*), 5.02 – 5.11 (m, 2H, OC*H*$_2$), 7.17 – 7.19 (m, 5H, OAr*H*), 7.60 – 7.62 (m, 2H, Ar*H*), 7.72 – 7.74 (m, 2H, Ar*H*); **^{13}C{^{1}H} NMR** (150 MHz, $CDCl_3$): δ = 24.5, 28.8, 33.9, 37.5 (*C*H$_2$), 43.1 (*C*H), 44.7, 45.5, 47.3, 49.1, 51.2, 52.4 (*C*H$_2$ macrocycle), 65.3 (O*C*H$_2$), 127.0 (*C*$_{arom}$), 127.6, 128.3, 128.4, 128.5, 128.6, 128.7 (O*C*$_{arom}$), 132.1, 134.0 (*C*$_{arom}$), 168.4 (*C*=O), 168.5 (O*C*=O); **LRMS** (ESI) *m/*z = 479.2 $[M + H]^+$; **HRMS** (ESI) *m/z* = 479.2648 $[M + H]^+$ (experimental), 479.2653 (calcd).

6.4.7 Benzyl 2-(4,7-bis((diethoxyphosphoryl)methyl)-1,4,7-triazacyclononan-1-yl)-6-(1,3-dioxoisoindolin-2-yl)hexanoate (6)

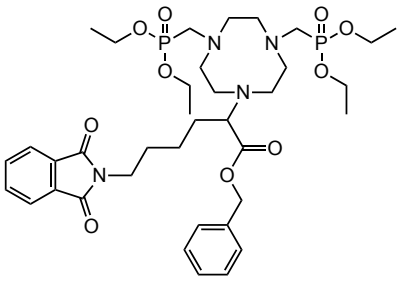

To a solution of **5** (0.23 g, 0.48 mmol, 1 equiv.) in acetonitrile (20 mL) was added paraformaldehyde (0.03 g, 1.05 mmol, 2.2 equiv.) at 70 °C and the mixture was stirred for 1 h. Triethyl phosphite (0.16 mL, 0.95 mmol, 2 equiv.) was added and the mixture was left to stir for 2 d at reflux. The mixture was filtered and the filtrate was concentrated *in vacuo*. The crude product was dissolved in diethyl ether, washed with water (3 x 75 mL) and the organic layers were collected and dried over Na_2SO_4. The mixture was filtered and concentrated *in vacuo* to produce an orange oil (0.08 g, 0.10 mmol, 27%). **^{1}H NMR** (600

MHz, $CDCl_3$): δ = 1.25 (t, 12H, $POCH_2CH_3$, $^3J_{HH}$ = 6 Hz), 1.37 (m, 2H, CH_2), 1.52 (m, 2H, CH_2), 1.60 – 1.64 (m, 4H, PCH_2), 1.85 (m, 2H, CH_2), 2.44 – 2.79 (m, 4H, CH_2 macrocycle), 2.81 – 2.95 (m, 4H, CH_2 macrocycle), 3.01 – 3.18 (m, 4H, CH_2 macrocycle), 3.59 (t, 2H, CH_2, ^3J = 6 Hz), 4.03 – 4.07 (m, 8H, $POCH_2CH_3$), 4.63 (s, 1H, CH), 5.00 – 5.05 (m, 2H, OCH_2), 7.21 – 7.27 (m, 5H, OAr*H*), 7.64 (m, 2H, Ar*H*), 7.76 (m, 2H, Ar*H*); **$^{13}C\{^1H\}$ NMR** (150 MHz, $CDCl_3$): δ = 21.7 (PCH_2), 23.9 (CH_2), 27.3 (CH_2), 28.7 ($POCH_2CH_3$), 32.9 (CH_2), 36.7 (CH_2), 38.4 (CH), 48.1, 52.0, 55.2 (CH_2 macrocycle), 61.0 ($POCH_2CH_3$), 64.3 (OCH_2), 122.2 (C_{arom}), 126.0, 126.6, 126.9, 127.3, 127.4, 127.6, (OC_{arom}), 131.1, 132.9 (C_{arom}), 167.3 (C=O, OC=O); **LRMS** (ESI) *m/z* = 779.3 $[M + H]^+$; **HRMS** (ESI) *m/z* = 779.3549 $[M + H]^+$ (experimental), 779.3544 (calcd).

6.4.8 1,4,7-triazacyclononane-1,4,7-tri(methylenephosphonato)gallium(III) ([Ga(NOTP)])

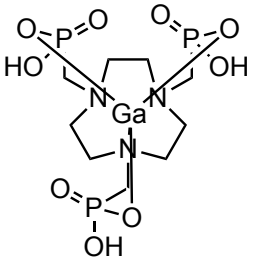

1,4,7-Triazacyclononane-1,4,7-tri(methylene phosphonic acid) (NOTP, 20 mg, 0.049 mmol) and $Ga(NO_3)_3 \cdot H_2O$ (12.5 mg, 0.049 mmol) were dissolved in 1 mL of water to produce a slightly turbid mixture. After brief heating at 70 °C, the solution turned clear. The pH of the solution was found to be <1. An aqueous solution of 5% NH_3 was added until a pH of between 2 – 3 was achieved. **LRMS** (ESI) *m/z* = 477.9 $[M + H]^+$, 499.9 $[M + Na]^+$. Colourless crystals suitable for X-ray diffraction studies were obtained by slow crystallisation of the above solution.

6.5 Solid-Phase Synthesis

6.5.1 Compound 10

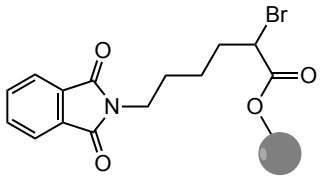

Freshly regenerated 2-chlorotrityl chloride resin (0.11 g, 1.0 mmol/g loading) was allowed to warm to room temperature before being transferred into a solid-phase synthesis reaction vessel. The resin was swelled with DCM (30 mL) and the vessel was shaken for 30 min. 2-Bromo-6-(1,3-dioxoisoindolin-2-yl)hexanoic acid (0.11 g, 0.33 mmol, 3 equiv.) and DIEA (28 μL, 0.16 mmol, 1.5 equiv.) were added to the resin and the reaction mixture was mechanically shaken overnight at room temperature. MeOH (5 mL) was added as a capping reagent and the reaction was further shaken for 10 min. The solution was filtered and the resin was washed with DCM, *i*PrOH and MeOH and dried. A test cleave was performed by adding 250 μL of TFA/H_2O/TIPS (38:1:1) v/v to a small amount of resin in an Eppendorf tube. The mixture was shaken for 1 min, then the solvent was evaporated by blowing nitrogen gas over the mixture. The remaining solid was dissolved in 1 mL of acetonitrile, centrifuged and the resulting supernatant was collected. **LRMS** (ESI) *m/z* = 341.0 $[M + H]^+$.

6.5.2 Compound 11

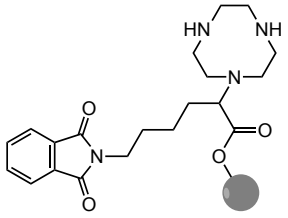

A solution of 1,4,7-triazacyclononane (0.44 g, 3.19 mmol, 10 equiv.) was dissolved in DCM (4 mL) and added to the pre-swelled resin (in DCM), and shaken mechanically overnight at room temperature. The resin was filtered and washed with DCM, *i*PrOH, MeOH and finally *i*PrOH.

A test cleave of the product bound to the resin was performed as previously described. A chloranil test indicated the presence of secondary amines. **LRMS** (ESI) *m/z* = 389.2 $[M + H]^+$; **HRMS** (ESI) *m/z* = 389.2185 $[M + H]^+$ (experimental), 389.2144 (calcd).

6.5.3 Compound 12

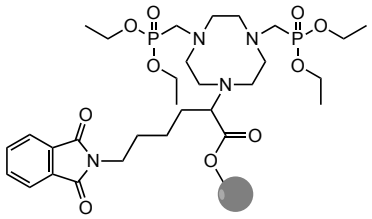

Triethyl phosphite (0.328 mL, 1.914 mmol, 6 equiv.) and paraformaldehyde (0.019 g, 0.638 mmol, 2 equiv.) were added to the pre-swelled (5 mL 1:1 DMF/THF) resin, and shaken mechanically at room temperature for 6 d. The resin was filtered and washed with DCM, *i*PrOH, MeOH and finally *i*PrOH. A test cleave of the product bound to the resin was performed as previously described. A chloranil test indicated the presence of secondary amines. **LRMS** (ESI) *m/z* = 689.3 $[M + H]^+$; **HRMS** (ESI) *m/z* = 689.3080 $[M + H]^+$ (experimental), 689.3036 (calcd).

6.5.4 Compound 13

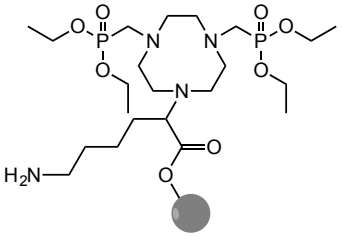

The resin was washed with 3 x DCM, 3 x 1:1 DCM/THF and 3 x THF. A solution of 1:1 MeOH/THF (4.5 mL) and hydrazine monohydrate (0.5 mL) was added. This mixture was then loaded onto the resin and shaken mechanically overnight. The resin was filtered and washed with MeOH and DCM. **LRMS** (ESI) *m/z* = 559.8 $[M + H]^+$; **HRMS** (ESI) *m/z* = 557.2875 $[M - H]^-$ (experimental), 557.2875 (calcd).

References

[1] J. C. Dabrowiak, *Metals in Medicine*, John Wiley & Sons, **2017**.

[2] S. J. Lippard, in *Bioinorganic Chemistry*, **1994**, pp. 505-583.

[3] L. Ronconi, P. J. Sadler, *Coord. Chem. Rev.* **2008**, *252*, 2239-2277.

[4] a) B. Rosenberg, L. Van Camp, T. Krigas, *Nature* **1965**, *205*, 698-699; b) S. Dasari, P. B. Tchounwou, *Eur. J. Pharmacol.* **2014**, *740*, 364-378.

[5] a) T. Storr, *Ligand Design in Medicinal Inorganic Chemistry*, John Wiley & Sons, Chichester, West Sussex, United Kingdom, **2014**; b) J. L. Sessler, *Medicinal Inorganic Chemistry*, Oxford University Press, Washington, DC, **2005**; c) D. L. Ma, H. Z. He, K. H. Leung, D. S. H. Chan, C. H. Leung, *Angew. Chem. Int. Ed.* **2013**, *52*, 7666-7682; d) L. Chiang, M. R. Jones, C. L. Ferreira, T. Storr, *Curr. Top. Med. Chem.* **2012**, *12*, 122-144.

[6] L. Ronconi, P. J. Sadler, *Coord. Chem. Rev.* **2007**, *251*, 1633-1648.

[7] M. D. Bartholomä, A. S. Louie, J. F. Valliant, J. Zubieta, *Chem. Rev.* **2010**, *110*, 2903-2920.

[8] I. Bertini, Knovel, *Biological Inorganic Chemistry: Structure and Reactivity*, Sausalito, Calif. : University Science Books, **2007**.

[9] E. W. Price, C. Orvig, *Chem. Soc. Rev.* **2013**, *43*, 260-290.

[10] P. J. Blower, *Dalton Trans.* **2015**, *44*, 4819-4844.

[11] S. Liu, D. S. Edwards, *Bioconjugate Chem.* **2001**, *12*, 7-34.

[12] A. Rahmim, H. Zaidi, *Nucl. Med. Commun.* **2008**, *29*, 193-207.

[13] G. Pathuri, A. F. Hedrick, S. E. January, W. K. Galbraith, V. Awasthi, C. D. Arnold, B. D. Cowley, H. Gali, *J. Label. Compd. Radiopharm.* **2015**, *58*, 14-19.

[14] D. L. Smith, W. A. P. Breeman, J. Sims-Mourtada, *Appl. Radiat. Isot.* **2013**, *76*, 14-23.

[15] A. Turlakow, H. W. Yeung, J. Pui, H. Macapinlac, E. Liebovitz, V. Rusch, A. Goy, S. M. Larson, *Arch. Intern. Med.* **2001**, *161*, 1003-1007.

[16] A. Almuhaideb, N. Papathanasiou, J. Bomanji, *Ann. Saudi Med.* **2011**, *31*, 3-13.

[17] I. Velikyan, *Molecules* **2015**, *20*, 12913-12943.

[18] L. E. McInnes, S. E. Rudd, P. S. Donnelly, *Coord. Chem. Rev.* **2017**, *352*, 499-516.

[19] F. Rösch, in *Theranostics, Gallium-68, and Other Radionuclides*, Springer, **2013**, pp. 3-16.

[20] a) H. Schnökel, *Dalton Trans.* **2008**, 4344-4362; b) C. Jones, A. Stasch, in *The Group 13 Metals Aluminium, Gallium, Indium and Thallium: Chemical Patterns and Peculiarities*, **2011**; c) R. C. Fischer, P. P. Power, *Chem. Rev.* **2010**, *110*, 3877-3923.

[21] *CRC Handbook of Chemistry and Physics (Internet Version 2016)*, CRC Press LLC/Taylor and Francis, Boca Raton, FL, **2016**.

[22] S. M. Moerlein, M. J. Welch, *Int. J. Nucl. Med. Biol.* **1981**, *8*, 277-287.

[23] R. D. Shannon, *Acta Cryst. A* **1976**, *32*, 751-767.

[24] R. G. Pearson, *Inorg. Chem.* **1988**, *27*, 734-740.

[25] J. E. Huheey, E. A. Keiter, R. L. Keiter, O. K. Medhi, *Inorganic Chemistry: Principles of Structure and Reactivity*, Pearson Education India, **2006**.

[26] L. R. Bernstein, *Pharmacol. Rev.* **1998**, *50*, 665-682.

[27] A. E. Martell, R. M. Smith, *Critical stability constants, Vol. 1*, Springer, **1974**.

[28] R. E. Weiner, G. J. Schreiber, P. B. Hoffer, J. T. Bushberg, *J. Nucl. Med.* **1985**, *26*, 908-916.

[29] M. Eder, O. Neels, M. Müller, U. Bauder-Wüst, Y. Remde, M. Schäfer, U. Hennrich, M. Eisenhut, A. Afshar-Oromieh, U. Haberkorn, K. Kopka, *Pharmaceuticals* **2014**, *7*, 779-796.

[30] R. Cusnir, C. Imberti, R. C. Hider, P. J. Blower, M. T. Ma, *Int. J. Mol. Sci.* **2017**, *18*, 1-23.

[31] E. Eppard, M. Wuttke, P. L. Nicodemus, F. Rösch, *J. Nucl. Med.* **2014**, *55*, 1023-1028.

[32] M. I. Tsionou, C. E. Knapp, C. A. Foley, C. R. Munteanu, A. Cakebread, C. Imberti, T. R. Eykyn, J. D. Young, B. M. Paterson, P. J. Blower, M. T. Ma, *RSC Adv.* **2017**, *7*, 49586-49599.

[33] J. D. Young, V. Abbate, C. Imberti, L. K. Meszaros, M. T. Ma, S. Y. Terry, R. C. Hider, G. E. Mullen, P. J. Blower, *J. Nucl. Med.* **2017**, *58*, 1270-1277.

[34] T. Joshi, M. Kubeil, A. Nsubuga, G. Singh, G. Gasser, H. Stephan, *ChemPlusChem* **2018**, *83*, 554-564.

[35] V. Kubíček, Z. Böhmová, R. Ševčíková, J. Vaněk, P. Lubal, Z. Poláková, R. Michalicová, J. Kotek, P. Hermann, *Inorg. Chem.* **2018**, *57*, 3061-3072.

[36] C. L. Ferreira, D. T. T. Yapp, D. Mandel, R. K. Gill, E. Boros, M. Q. Wong, P. Jurek, G. E. Kiefer, *Bioconjugate Chem.* **2012**, *23*, 2239-2246.

[37] S. V. Govindan, R. B. Michel, G. L. Griffiths, D. M. Goldenberg, M. J. Mattes, *Nucl. Med. Biol.* **2005**, *32*, 513-519.

[38] C. F. Ramogida, J. F. Cawthray, E. Boros, C. L. Ferreira, B. O. Patrick, M. J. Adam, C. Orvig, *Inorg. Chem.* **2015**, *54*, 2017-2031.

[39] J. Seemann, B. P. Waldron, F. Roesch, D. Parker, *ChemMedChem* **2015**, *10*, 1019-1026.

[40] a) M. I. M. Prata, A. C. Santos, C. F. G. C. Geraldes, J. J. P. de Lima, *J. Inorg. Biochem.* **2000**, *79*, 359-363; b) J. Notni, J. Šimeček, P. Hermann, H. J. Wester, *Chem. Eur. J.* **2011**, *17*, 14718-14722.

[41] H. Eidherr, F. Girschele, M. Mitterhauser, W. Wadsak, in *Radiochemical Syntheses*, John Wiley & Sons, **2012**, pp. 321-334.

[42] B. P. Burke, G. S. Clemente, S. J. Archibald, *J. Label. Compd. Radiopharm.* **2014**, *57*, 239-243.

[43] J.-F. Morfin, E. Tóth, *Inorg. Chem.* **2011**, *50*, 10371-10378.

[44] R. Delgado, J. J. R. F. Da Silva, *Talanta* **1982**, *29*, 815-822.

[45] M. I. Prata, J. P. André, Z. Kovács, A. I. Takács, G. Tircsó, I. Tóth, C. F. Geraldes, *J. Inorg. Biochem.* **2017**, *177*, 8-16.

[46] B. Drahoš, V. Kubíček, C. S. Bonnet, P. Hermann, I. Lukeš, É. Tóth, *Dalton Trans.* **2011**, *40*, 1945-1951.

[47] C. Geraldes, A. Sherry, W. Cacheris, *Inorg. Chem.* **1989**, *28*, 3336-3341.

[48] J. Notni, P. Hermann, J. Havlíčková, J. Kotek, V. Kubíček, J. Plutnar, N. Loktionova, P. J. Riss, F. Rösch, I. Lukeš, *Chem. Eur. J.* **2010**, *16*, 7174-7185.

[49] A. Evers, R. D. Hancock, A. E. Martell, R. J. Motekaitis, *Inorg. Chem.* **1989**, *28*, 2189-2195.

[50] A. Bianchi, L. Calabi, C. Giorgi, P. Losi, P. Mariani, P. Paoli, P. Rossi, B. Valtancoli, M. Virtuani, *J. Chem. Soc., Dalton Trans.* **2000**, 697-705.

[51] J. Notni, J. Šimeček, H.-J. Wester, *ChemMedChem* **2014**, *9*, 1107-1115.

[52] G. Máté, J. Šimeček, M. Pniok, I. Kertész, J. Notni, H.-J. Wester, L. Galuska, P. Hermann, *Molecules* **2015**, *20*, 13112-13126.

[53] C. Ferreira, E. Lamsa, M. Woods, Y. Duan, P. Fernando, C. Bensimon, M. Kordos, K. Guenther, P. Jurek, G. Kiefer, *Bioconjugate Chem.* **2010**, *21*, 531-536.

[54] Y. Ma, W. Luo, P. J. Quinn, Z. Liu, R. C. Hider, *J. Med. Chem.* **2004**, *47*, 6349-6362.

[55] K. E. Holt, G. E. Hutton, C. N. Morfitt, G. Ruecroft, S. J. Taylor, P. D. Tiffin, N. Tremayne, M. Woods, *Tetrahedron Lett.* **1997**, *38*, 8253-8256.

[56] W. Beck, *Z. Naturforsch. B* **2009**, *64*, 1221-1245.

[57] a) S.-G. Kim, J. Kim, H. Jung, *Tetrahedron Lett.* **2005**, *46*, 2437-2439; b) M. P. Doyle, B. Siegfried, J. F. Dellaria, *J. Org. Chem.* **1977**, *42*, 2426-2431.

[58] F. A. L. Anet, *J. Am. Chem. Soc.* **1986**, *108*, 1354-1355.

[59] B. Neises, W. Steglich, *Angew. Chem. Int. Ed.* **1978**, *17*, 522-524.

[60] a) M. A. Kuznetsov, A. S. Pan'kova, A. V. Ushkov, S. I. Selivanov, *Russ. J. Org. Chem.* **2008**, *44*, 1807-1815; b) R. C. Howell, S. H. Edwards, A. S. Gajadhar-Plummer, A. K. Ishenkumba, G. L. McPherson, J. T. Mague, A. J. P. White, D. J. Williams, *Molecules* **2003**, *8*, 565-592.

[61] S. Kimura, E. Bill, E. Bothe, T. Weyhermüller, K. Wieghardt, *J. Am. Chem. Soc.* **2001**, *123*, 6025-6039.

[62] a) A. R. Modarresi-Alam, P. Najafi, M. Rostamizadeh, H. Keykha, H.-R. Bijanzadeh, E. Kleinpeter, *J. Org. Chem.* **2007**, *72*, 2208-2211; b) A. K. Ghosh, M. Brindisi, *J. Med. Chem.* **2015**, *58*, 2895-2940.

[63] M. J. Little, N. Aubry, M.-E. Beaudoin, N. Goudreau, S. R. LaPlante, *J. Pharm. Biomed. Anal.* **2007**, *43*, 1324-1330.

[64] a) G. Keglevich, E. Bálint, R. Kangyal, M. Bálint, M. Milen, *Heteroat. Chem.* **2014**, *25*, 282-289; b) T. E. Ali, S. M. Abdel-Kariem, *Arkivoc* **2015**, *6*, 246-287.

[65] A. N. Pudovik, *Dokl. Akad. Nauk SSSR* **1952**, *83*, 865.

[66] a) R. A. Cherkasov, V. I. Galkin, *Russ. Chem. Rev.* **1998**, *67*, 857-882; b) R. Gancarz, I. Gancarz, *Tetrahedron Lett.* **1993**, *34*, 145-148; c) R. A. Cherkasov, V. I. Galkin, N. G. Khusainova, O. A. Mostovaya, R. Garifzyanov, G. K. Nuriazdanova, N. S. Krasnova, E. A. Berdnikov, *Russ. J. Gen. Chem. (Engl. Transl.)* **2005**, *41*, 1481-1484; d) V. I. Kruitkov, A. N. Lavrent'ev, E. V. Sukhanovskaya, *Russ. J. Gen. Chem. (Engl. Transl.)* **1991**, *61*, 1321.

[67] D. Zeng, Q. Ouyang, Z. Cai, X.-q. Xie, C. J. Anderson, *Chem. Commun.* **2014**, *50*, 43-45.

[68] C. M. Sevrain, M. Berchel, H. Couthon, P.-A. Jaffrès, *Beilstein J. Org. Chem.* **2017**, *13*, 2186-2213.

[69] C. E. McKenna, M. T. Higa, N. H. Cheung, M.-C. McKenna, *Tetrahedron Lett.* **1977**, *18*, 155-158.

[70] S. M. Vibhute, J. Engelmann, T. Verbi, M. E. Maier, N. K. Logothetis, G. Angelovski, *Org. Biomol. Chem.* **2013**, *11*, 1294-1305.

[71] a) T. Bruckdorfer, O. Marder, F. Albericio, *Curr. Pharm. Biotechnol.* **2004**, *5*, 29-43; b) G. B. Fields, *Methods in Enzymology, Solid-Phase Peptide Synthesis, Vol. 289*, Academic Press, Orlando, FL, **1997**.

[72] E. Prats-Alfonso, F. García-Martín, N. Bayo, L. J. Cruz, M. Pla-Roca, J. Samitier, A. Errachid, F. Albericio, *Tetrahedron* **2006**, *62*, 6876-6881.

[73] F. García-Martín, N. Bayó-Puxan, L. J. Cruz, J. C. Bohling, F. Albericio, *QSAR Comb. Sci.* **2007**, *10*, 1027-1035.

[74] a) K. Barlos, O. Chatzi, D. Gatos, G. Stavropoulos, *Int. J. Peptide Protein Res.* **1991**, *37*, 513-520; b) K. Barlos, D. Gatos, W. Schäfer, *Angew. Chem. Int. Ed. Engl.* **1991**, *30*, 590-593.

[75] D. A. Pearson, M. Blanchette, M. L. Baker, C. A. Guindon, *Tetrahedron Lett.* **1989**, *30*, 2739-2742.

[76] a) A. L. Pedersen, A. P. Tofteng, L. Malik, K. J. Jensen, *Chem. Soc. Rev.* **2012**, *41*, 1826-1844; b) C. O. Kappe, *Acc. Chem. Res.* **2013**, *46*, 1579-1587.

[77] R. Eisenberg, W. W. Brennessel, *Acta Cryst.* **2006**, *62*, 464-466.

[78] E. J. Corey, J. C. Bailar, *J. Am. Chem. Soc.* **1959**, *81*, 2620-2629.

[79] S. Gabriel, *Ber. Dtsch. Chem. Ges.* **1887**, *20*, 2224-2236.

[80] *Rigaku Oxford Diffraction*, Yarnton, England, **2015**.

[81] G. M. Sheldrick, *Acta Crystallogr. C* **2015**, *71*, 3-8.

A Supplementary Information

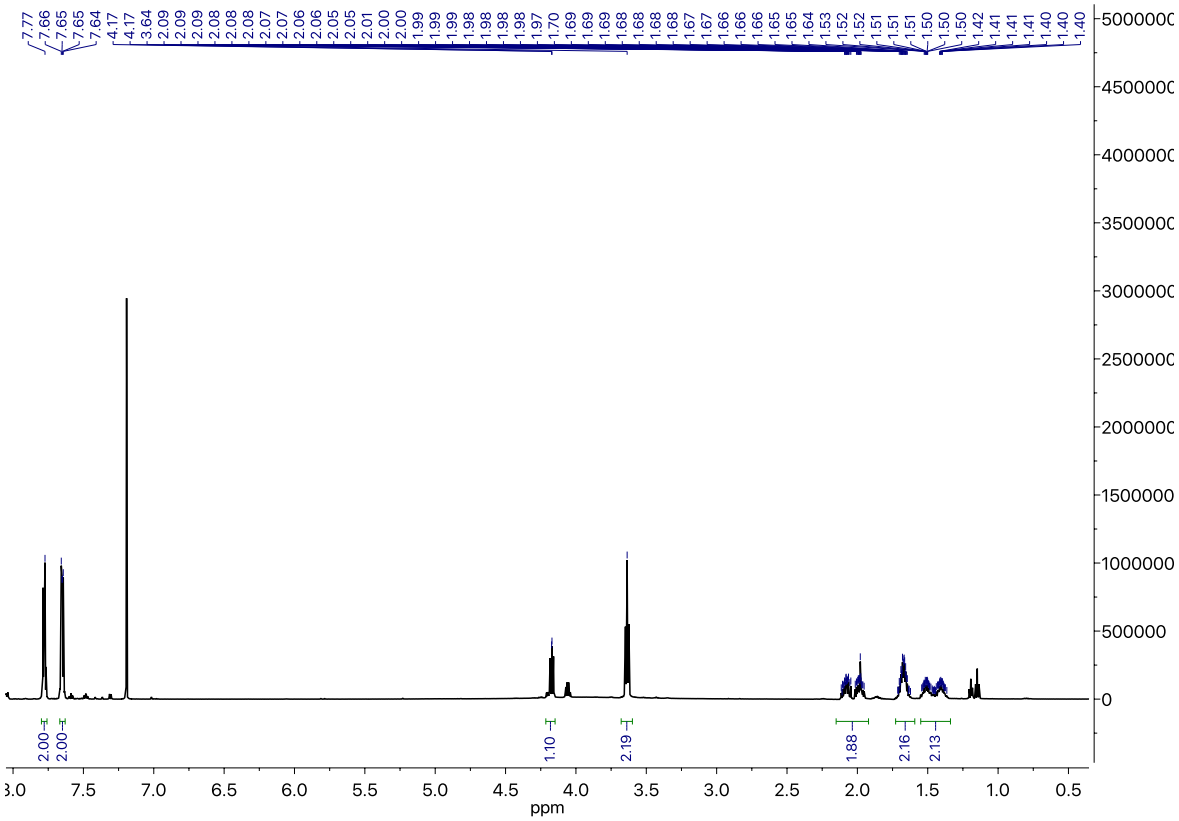

Figure A1: ^{1}H NMR spectrum of **1.**

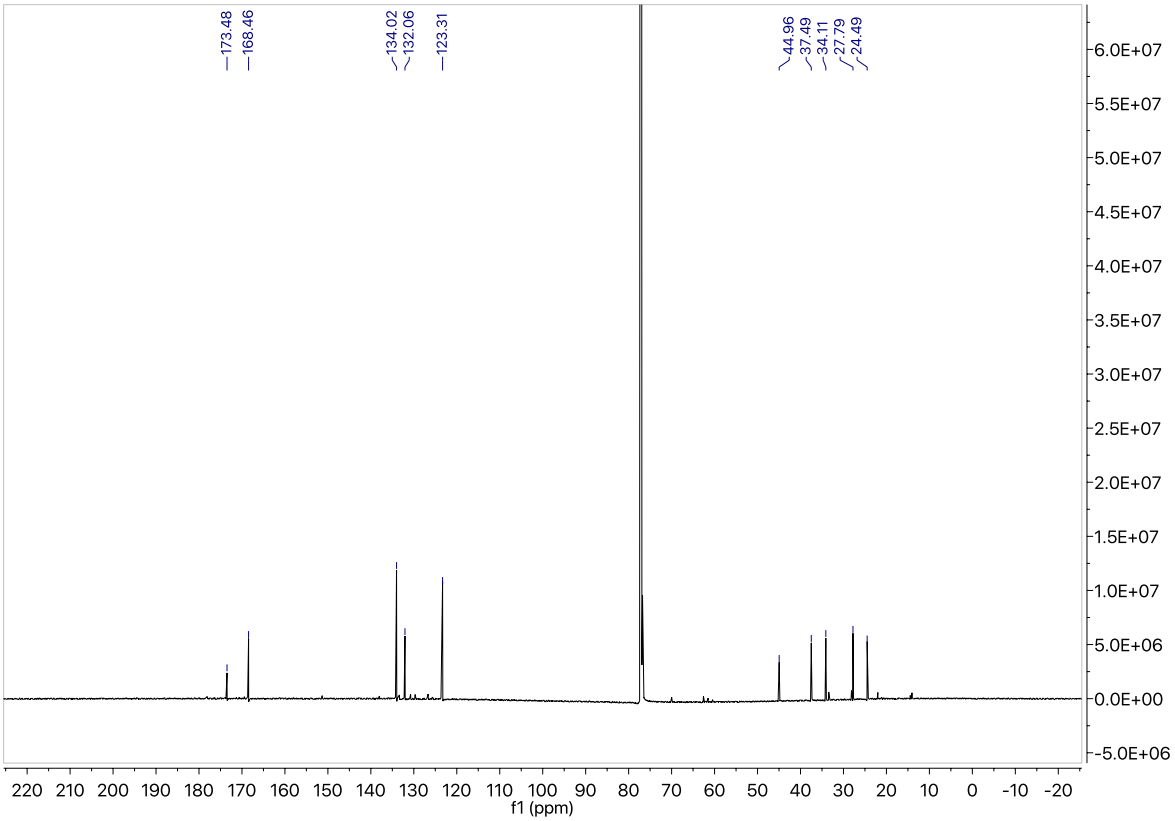

Figure A2: ^{13}C{^{1}H} NMR spectrum of **1.**

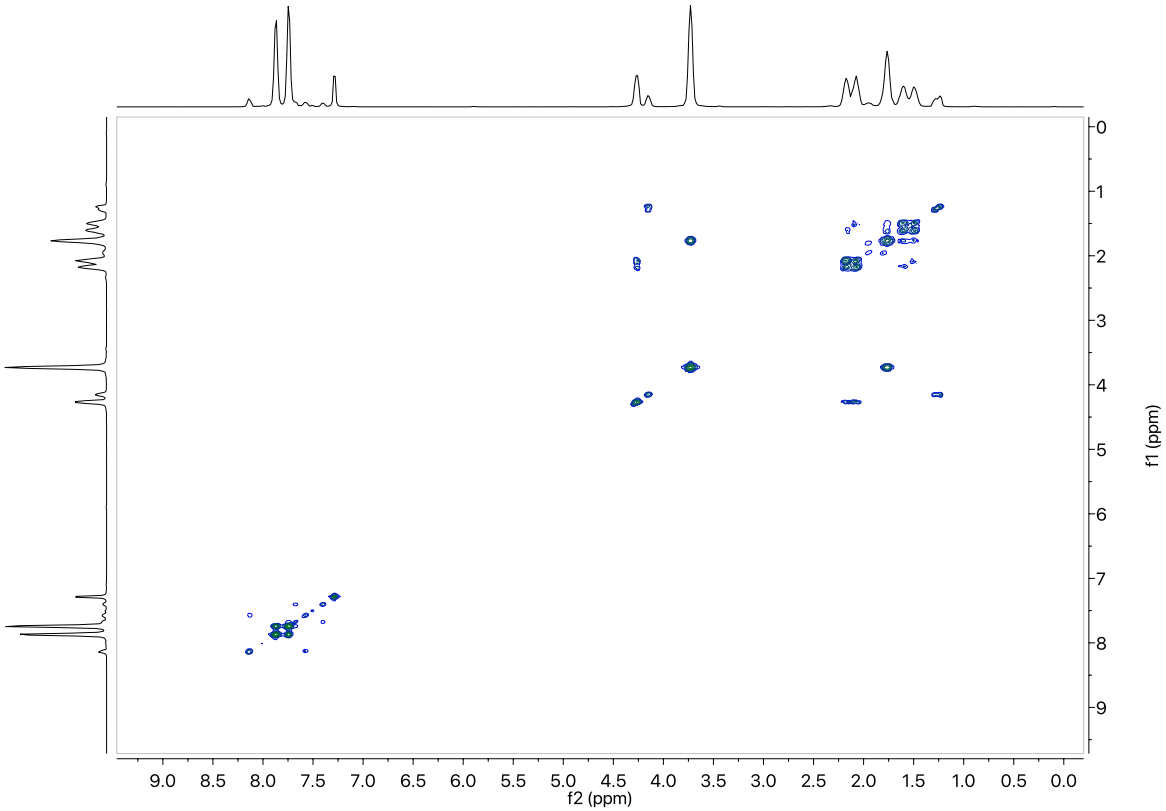

Figure A3: ^{1}H-^{1}H COSY spectrum of **1.**

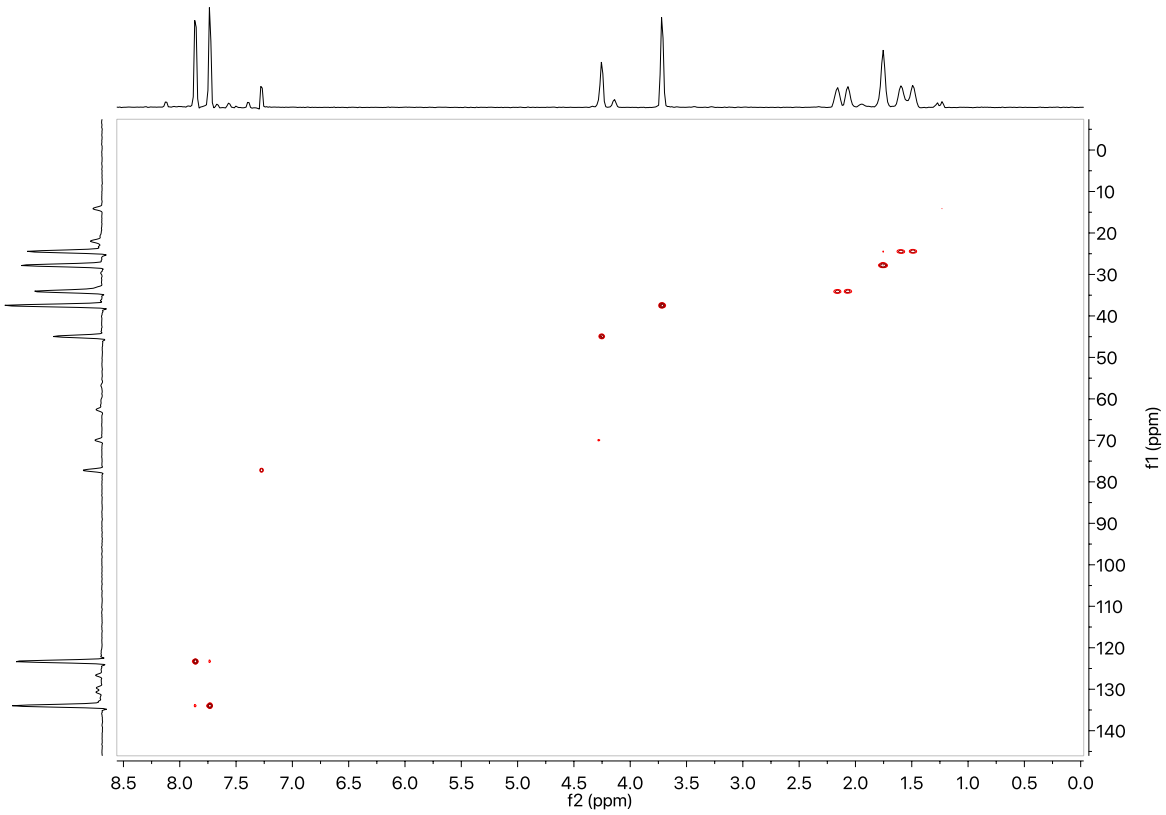

Figure A4: ^{1}H-^{13}C HSQC spectrum of **1.**

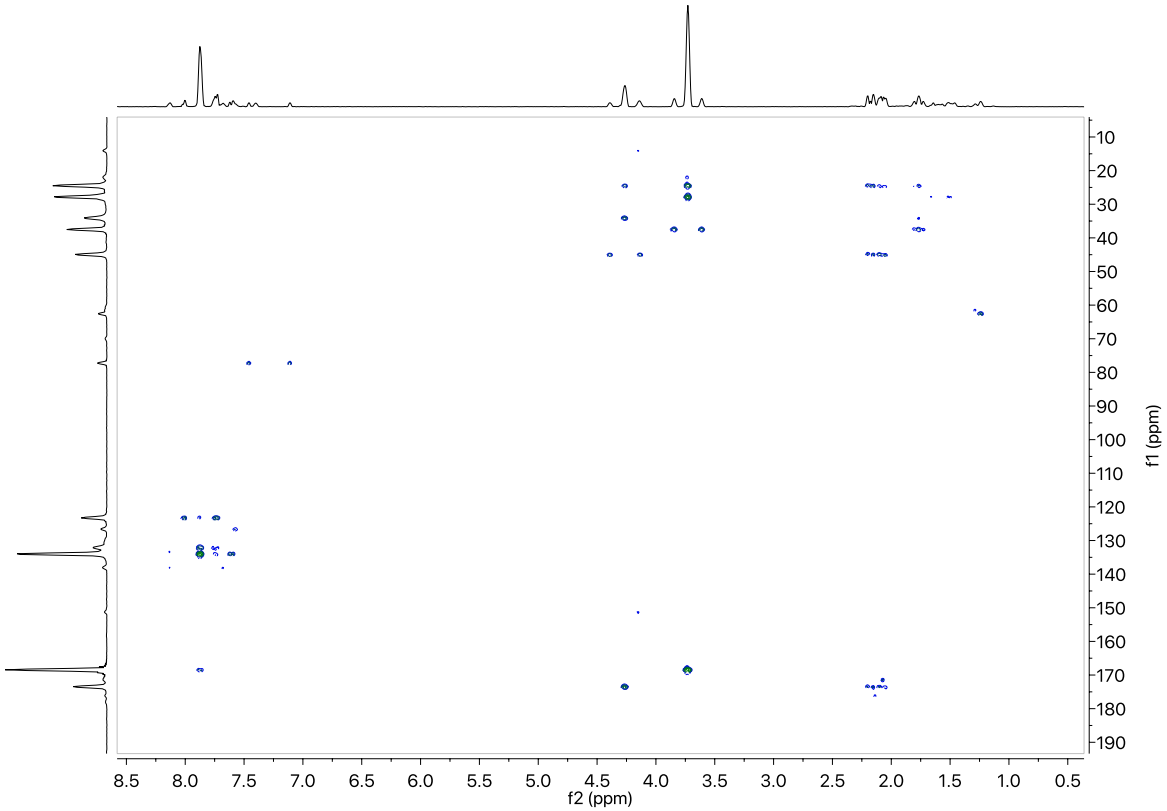

Figure A5: ^{1}H-^{13}C HMBC spectrum of **1.**

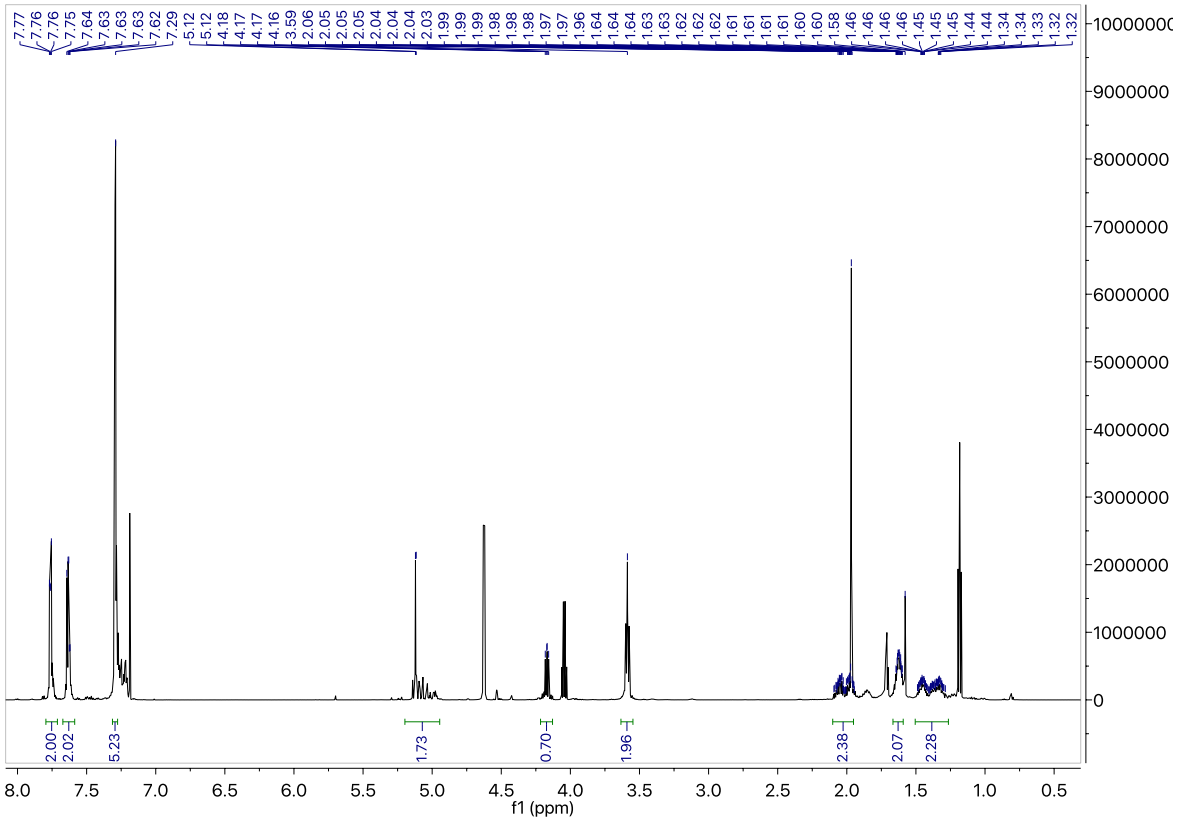

Figure A6: ^{1}H NMR spectrum of **2.**

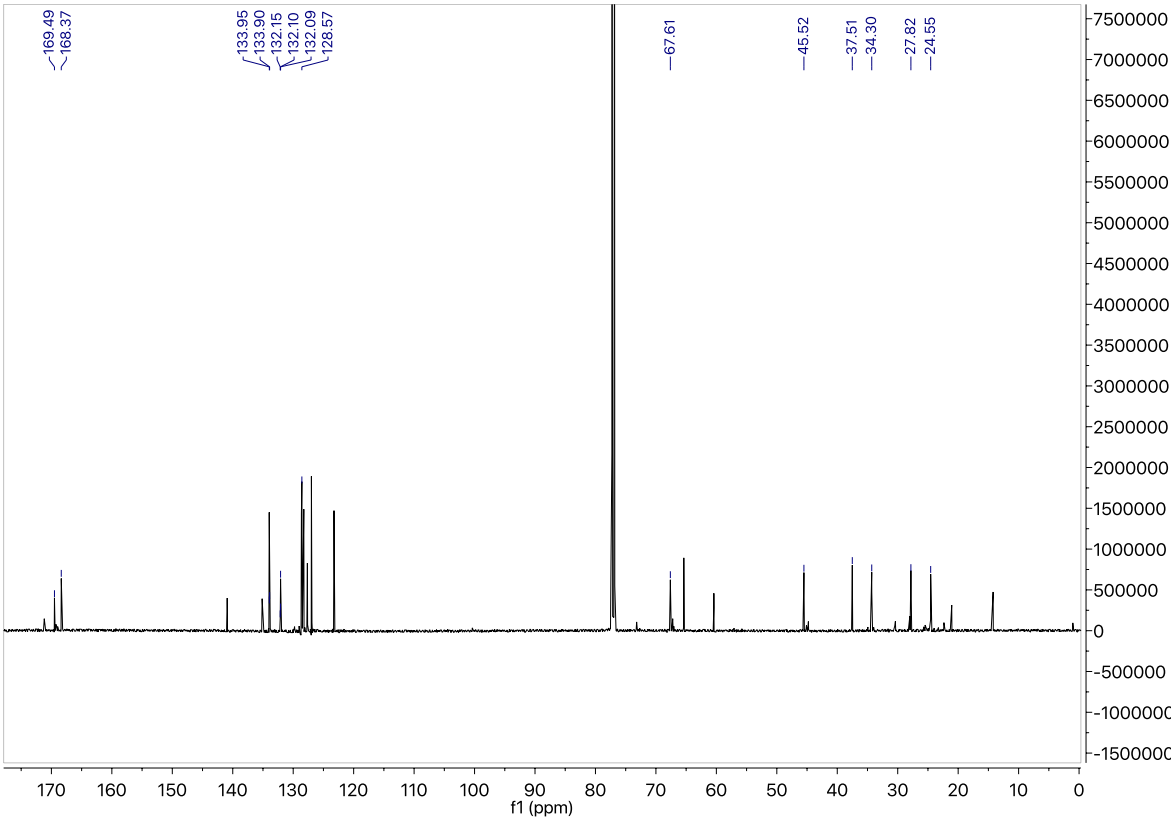

Figure A7: $^{13}C\{^{1}H\}$ NMR spectrum of **2.**

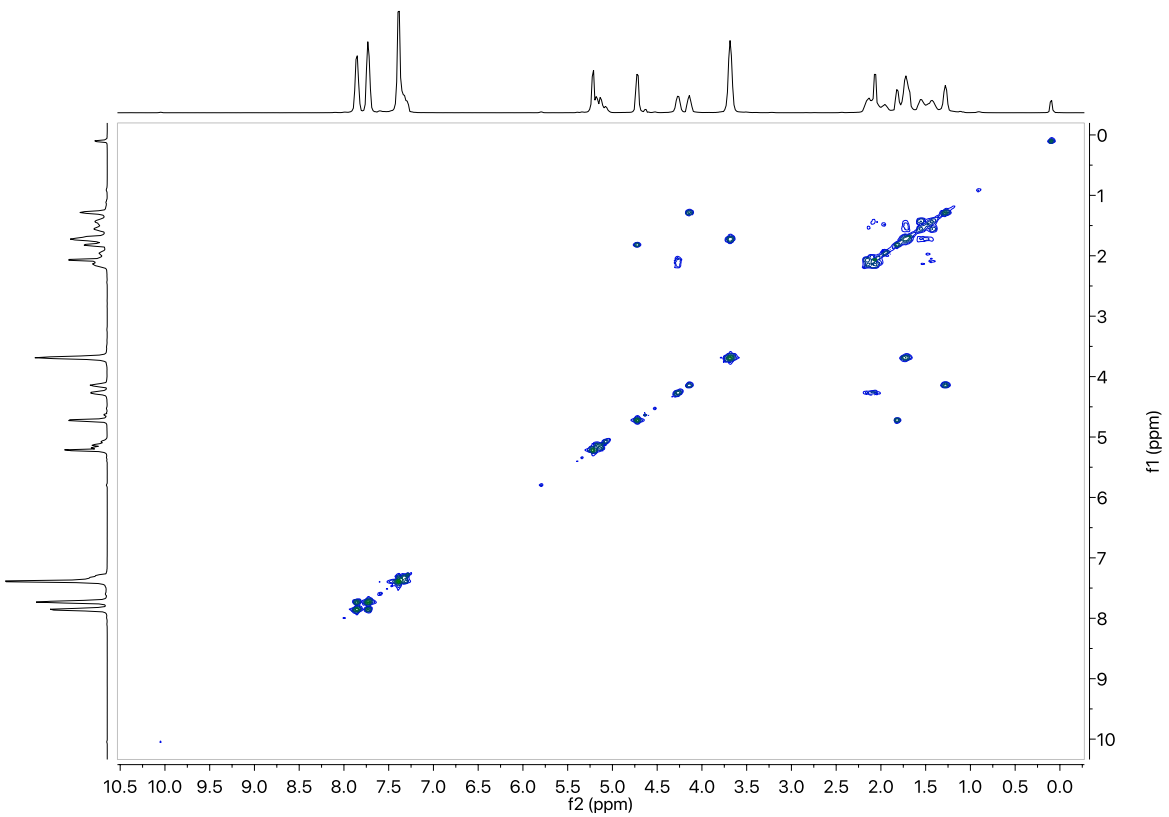

Figure A8: ^{1}H-^{1}H COSY spectrum of **2.**

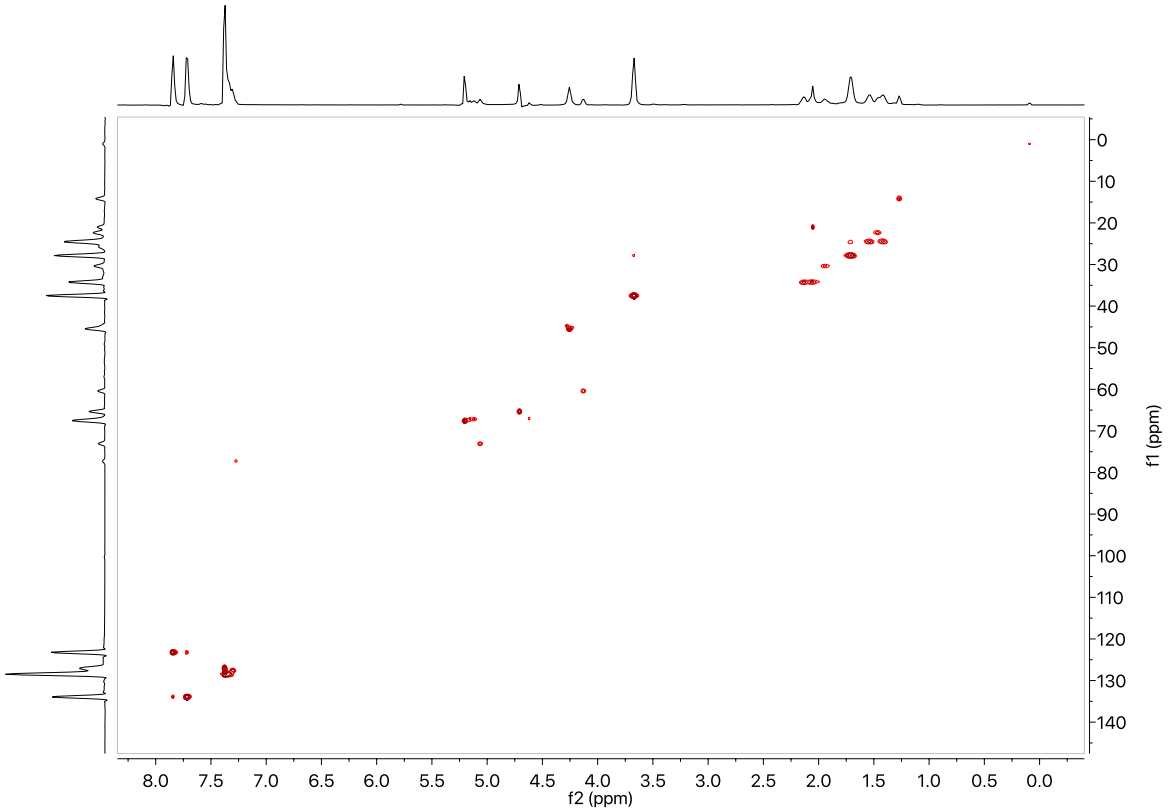

Figure A9: ^{1}H-^{13}C HSQC spectrum of **2.**

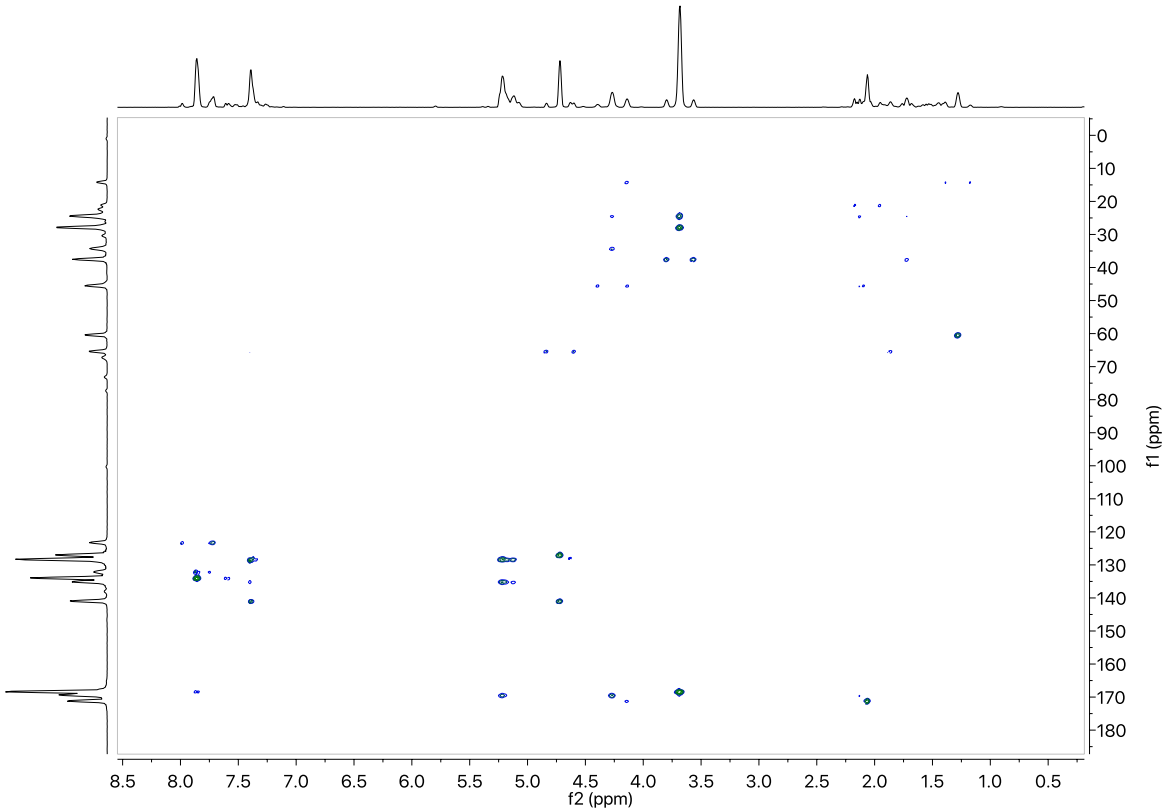

Figure 10: ^{1}H-^{13}C HMBC spectrum of **2.**

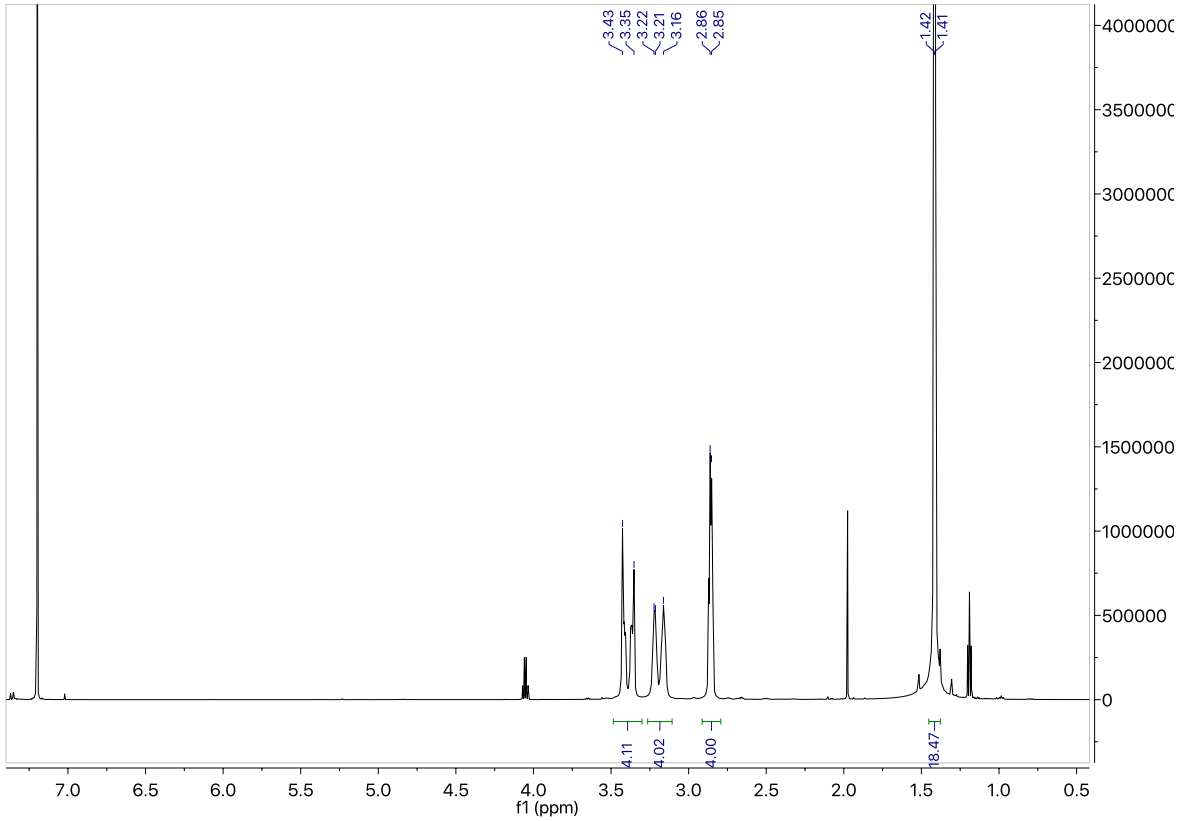

Figure A11: ^{1}H NMR spectrum of diBocTACN.

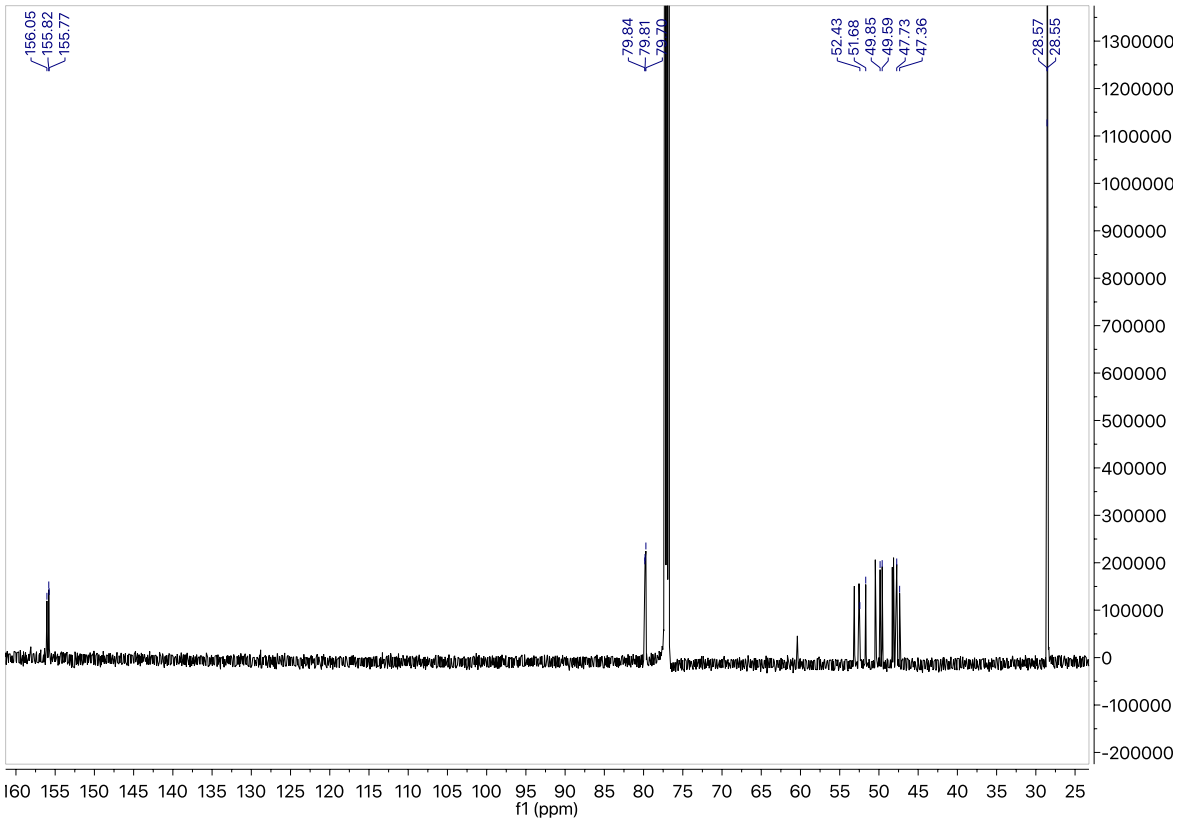

Figure A12: ^{13}C{^{1}H} NMR spectrum of diBocTACN.

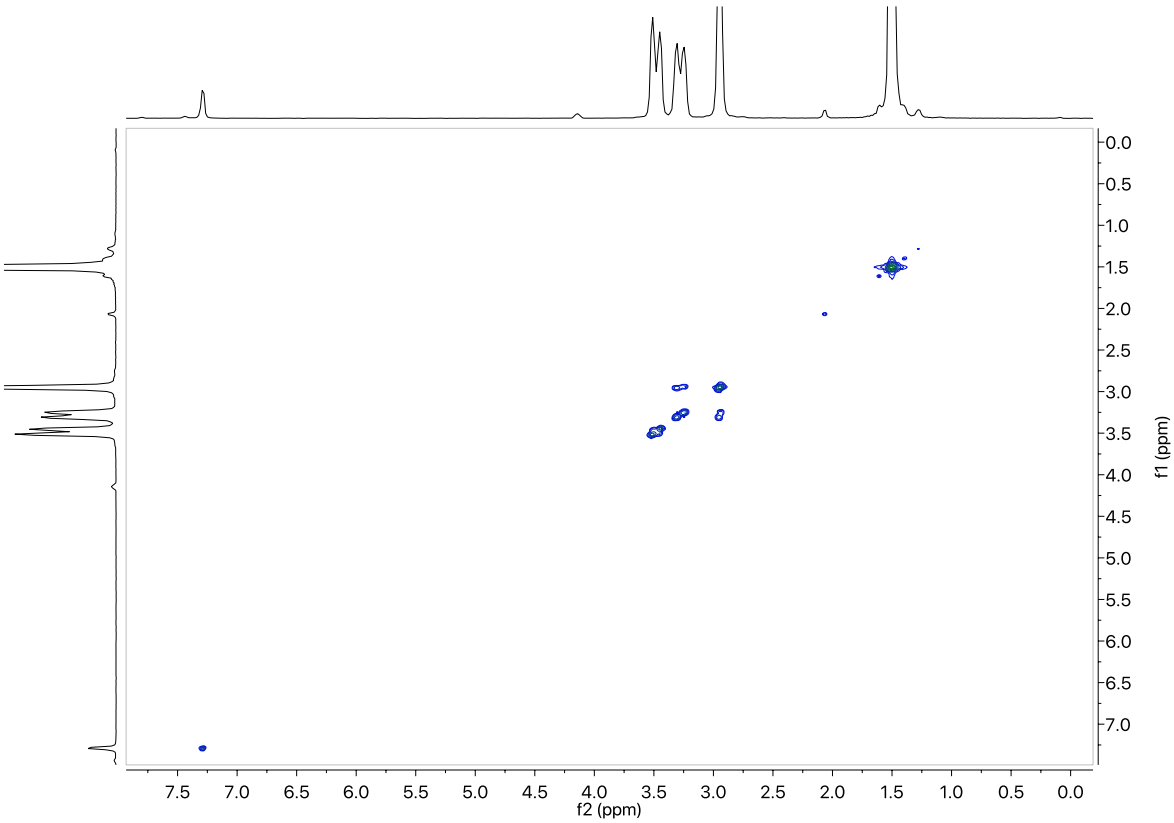

Figure A13: ^{1}H-^{1}H COSY spectrum of diBocTACN.

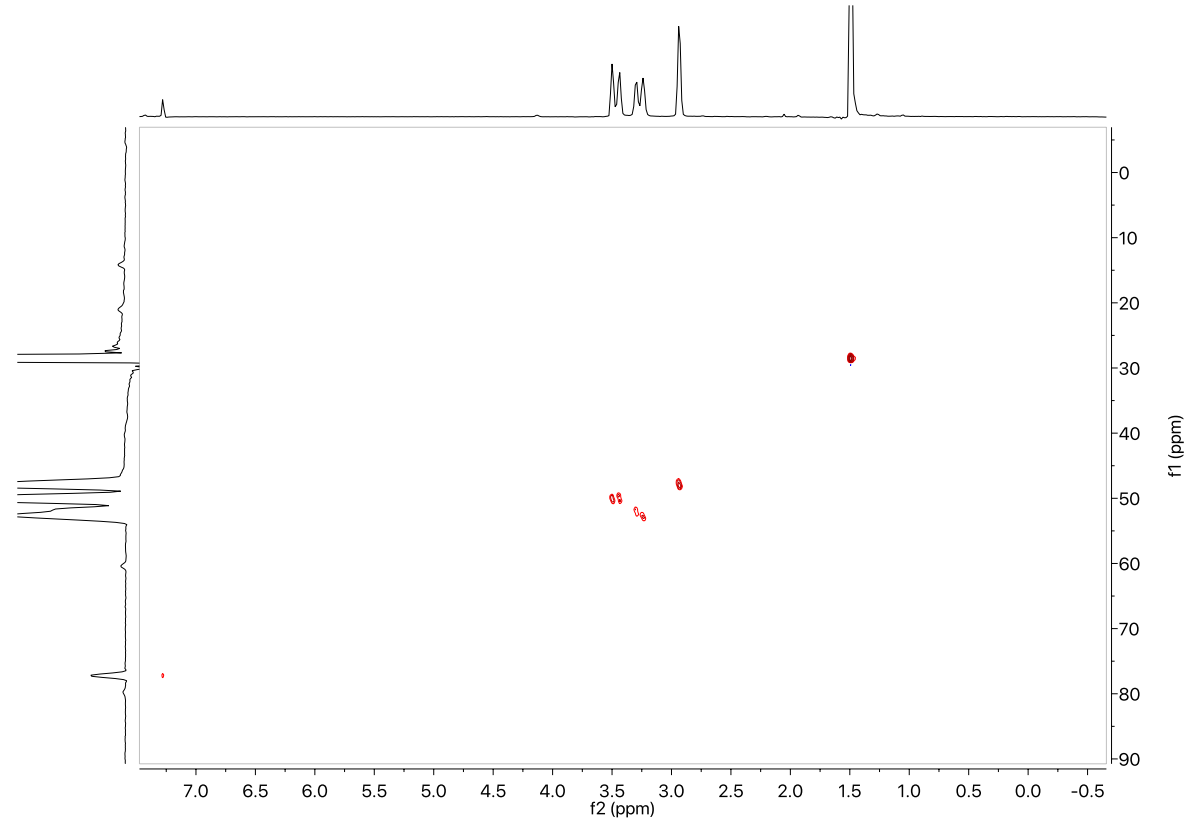

Figure A14: ^{1}H-^{13}C HSQC spectrum of diBocTACN.

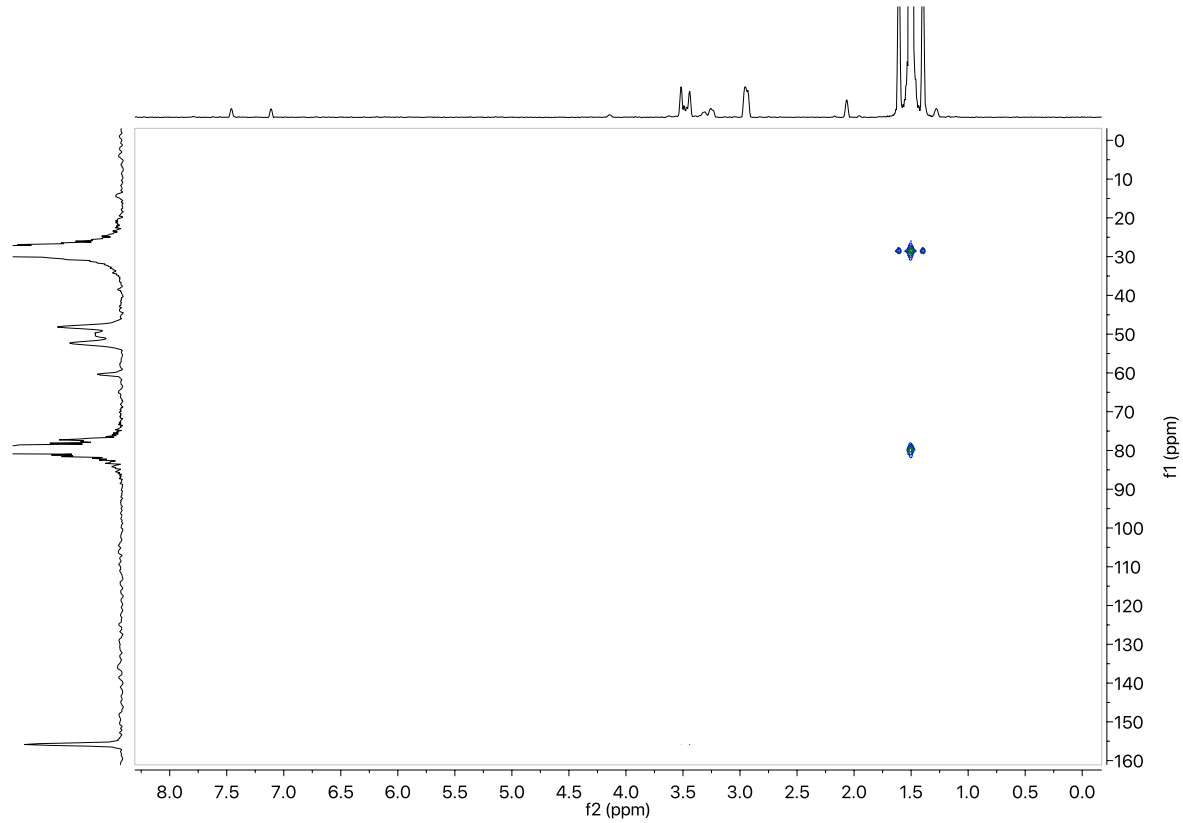

Figure A15: ^{1}H-^{13}C HMBC spectrum of diBocTACN.

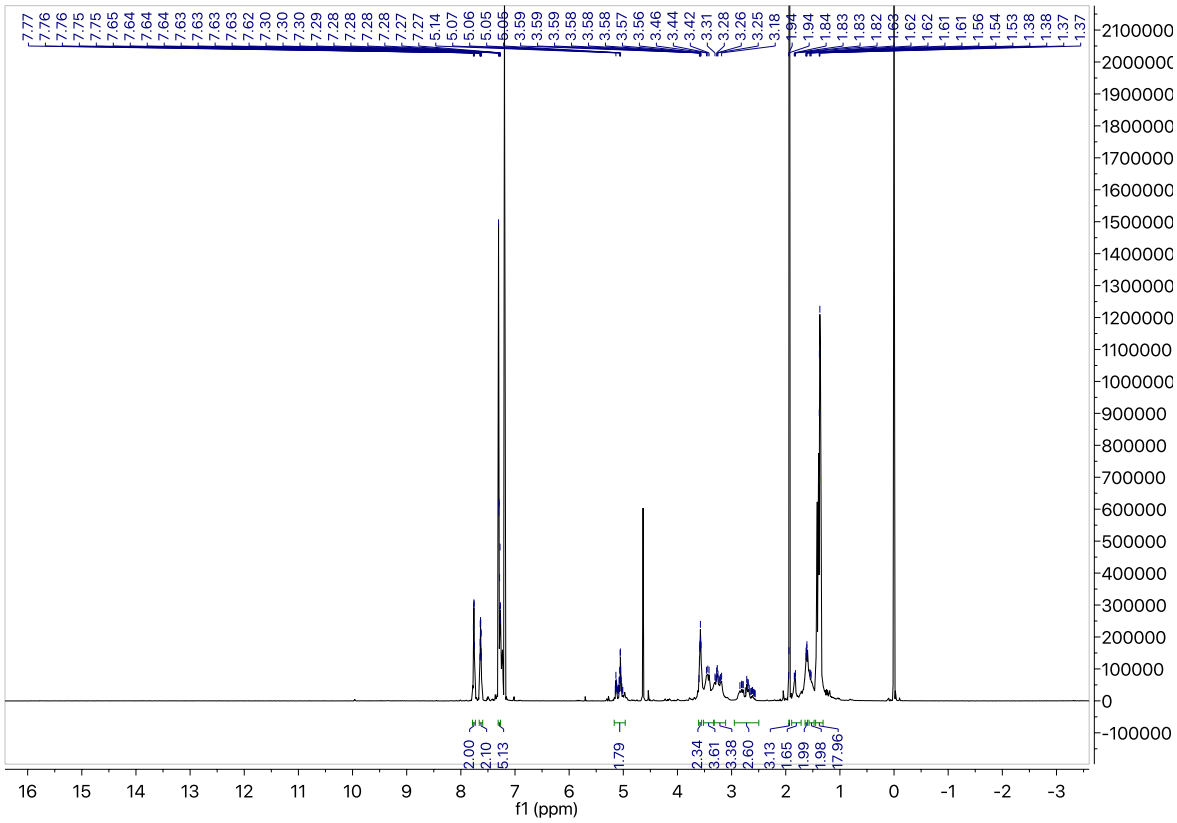

Figure A16: ^{1}H NMR spectrum of **3.**

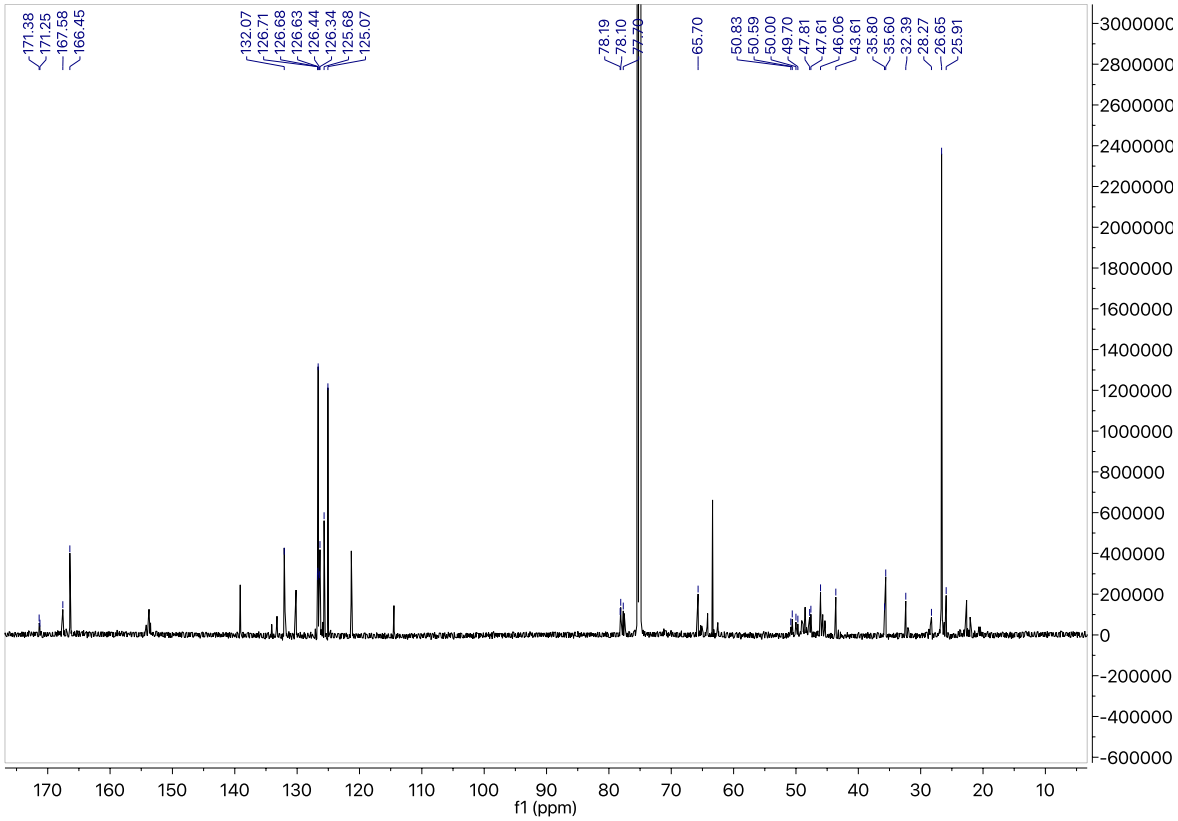

Figure A17: $^{13}C\{^{1}H\}$ NMR spectrum of **3.**

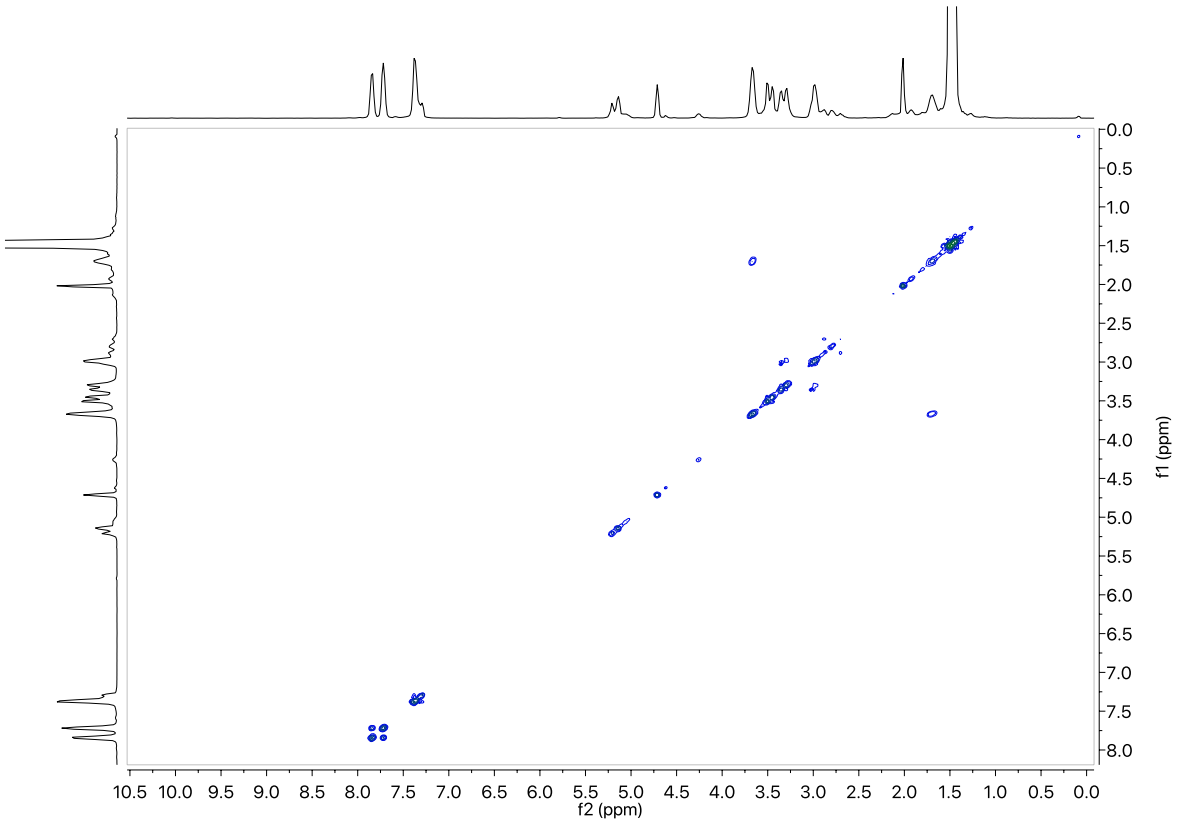

Figure A18: ^{1}H-^{1}H COSY spectrum of **3.**

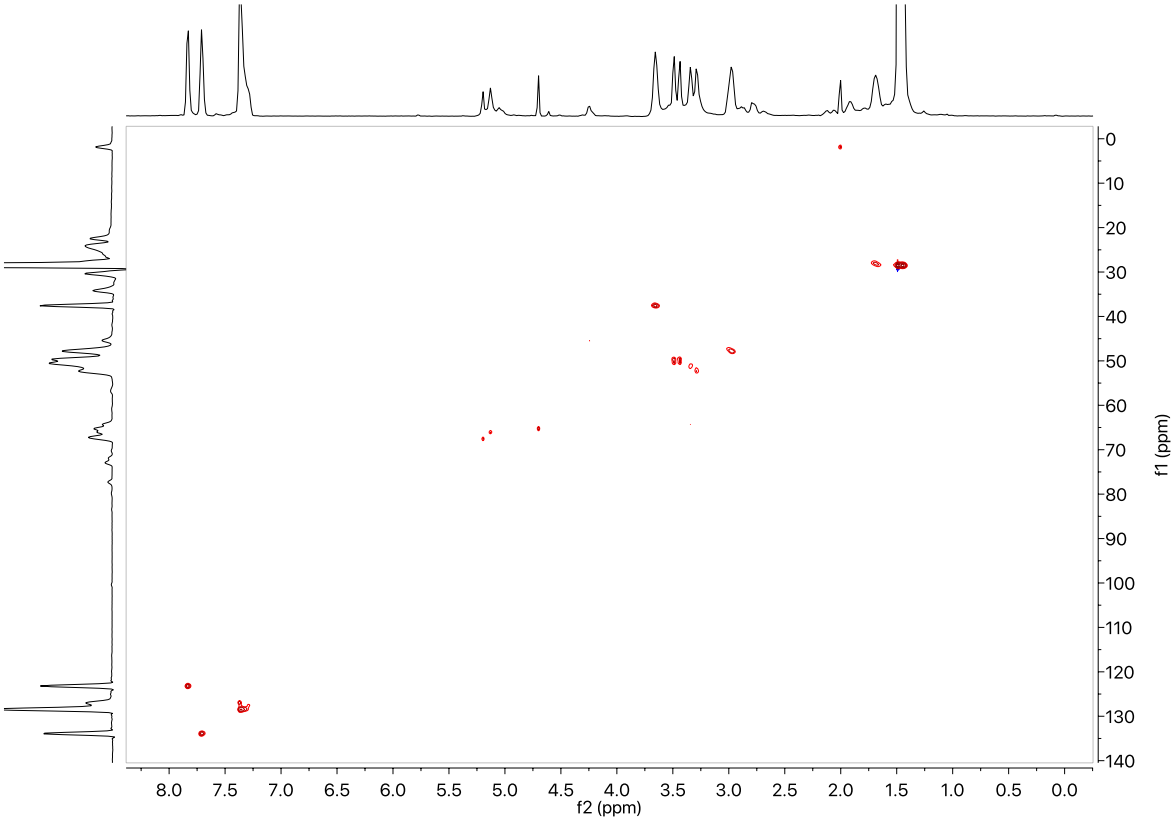

Figure A19: ^{1}H-^{13}C HSQC spectrum of **3.**

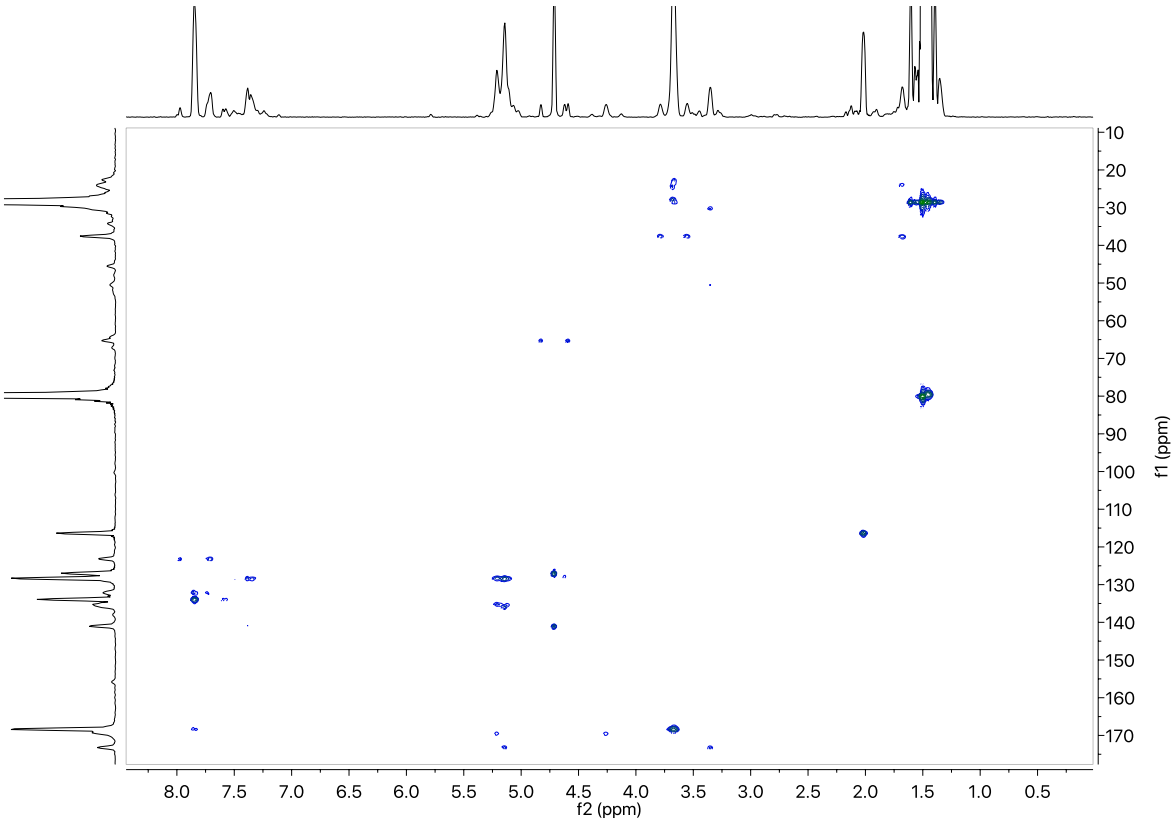

Figure A20: ^{1}H-^{13}C HMBC spectrum of **3.**

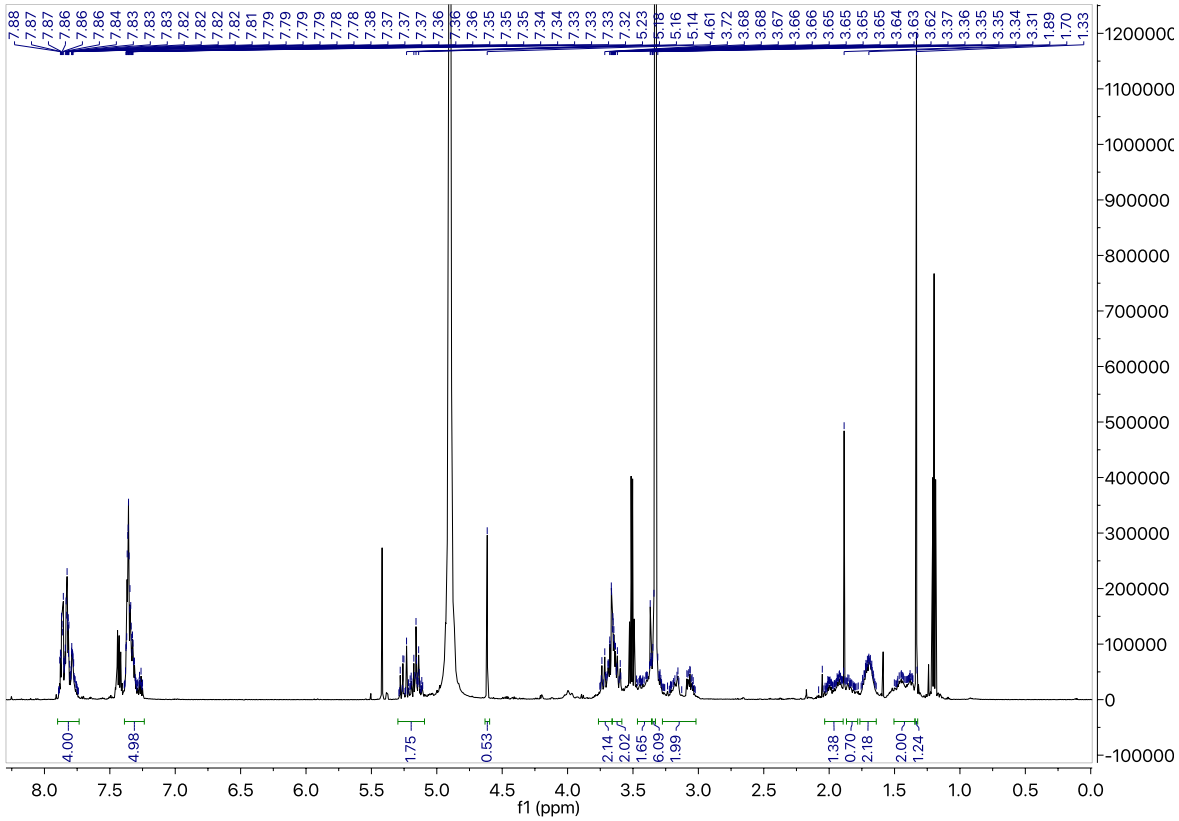

Figure A21: ^{1}H NMR spectrum of **4.**

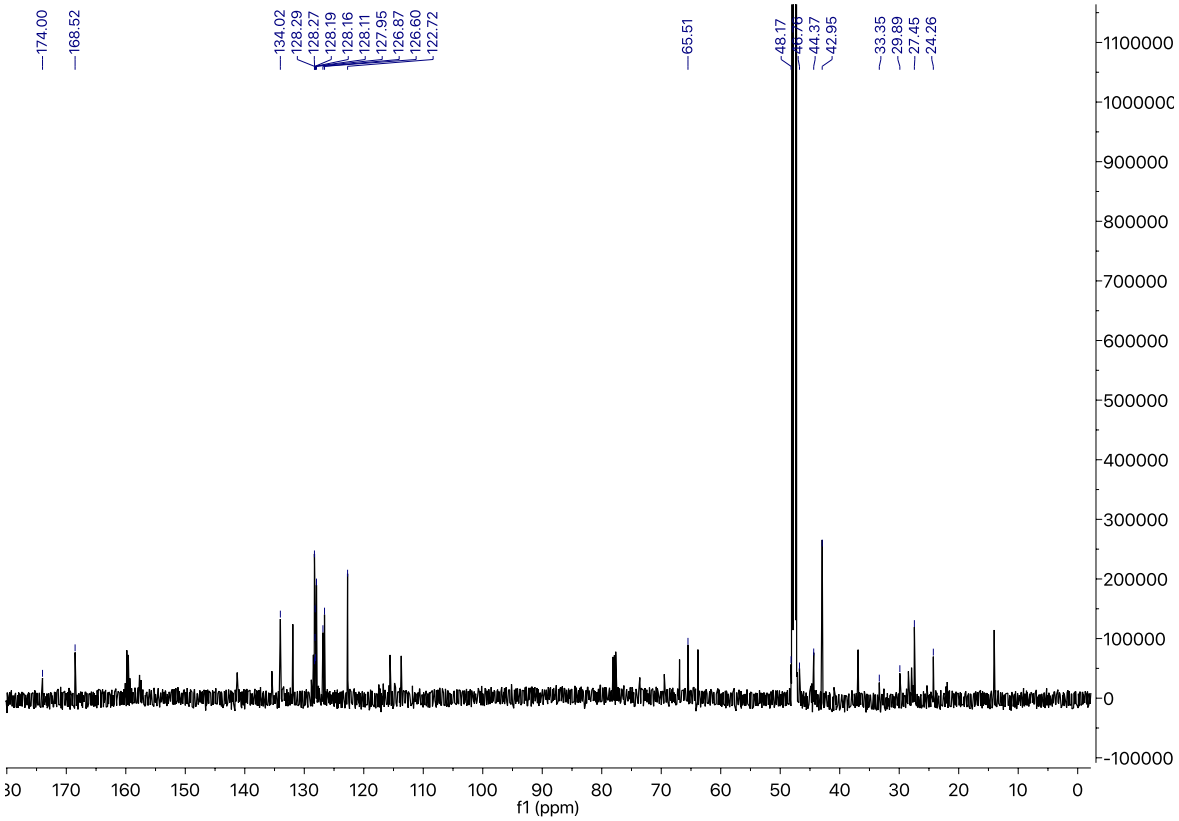

Figure A22: ^{13}C{^{1}H} NMR spectrum of **4.**

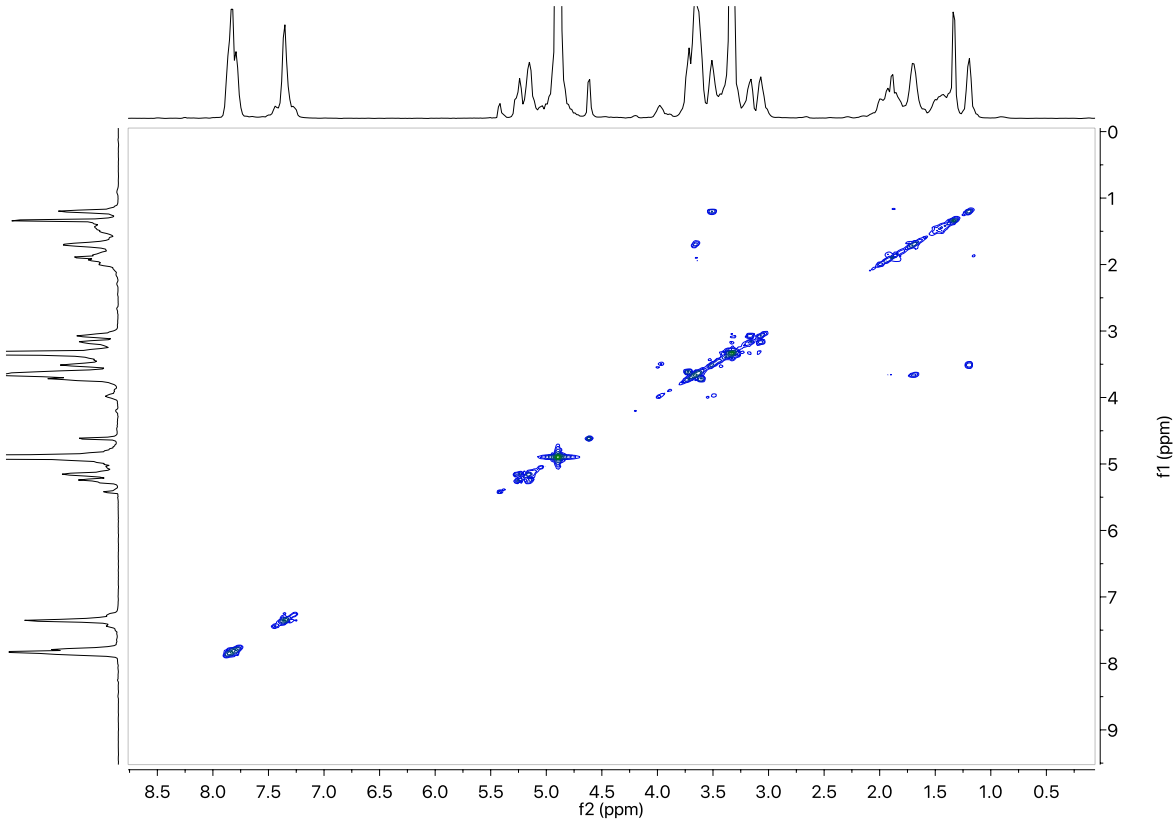

Figure A23: ^{1}H-^{1}H COSY spectrum of **4.**

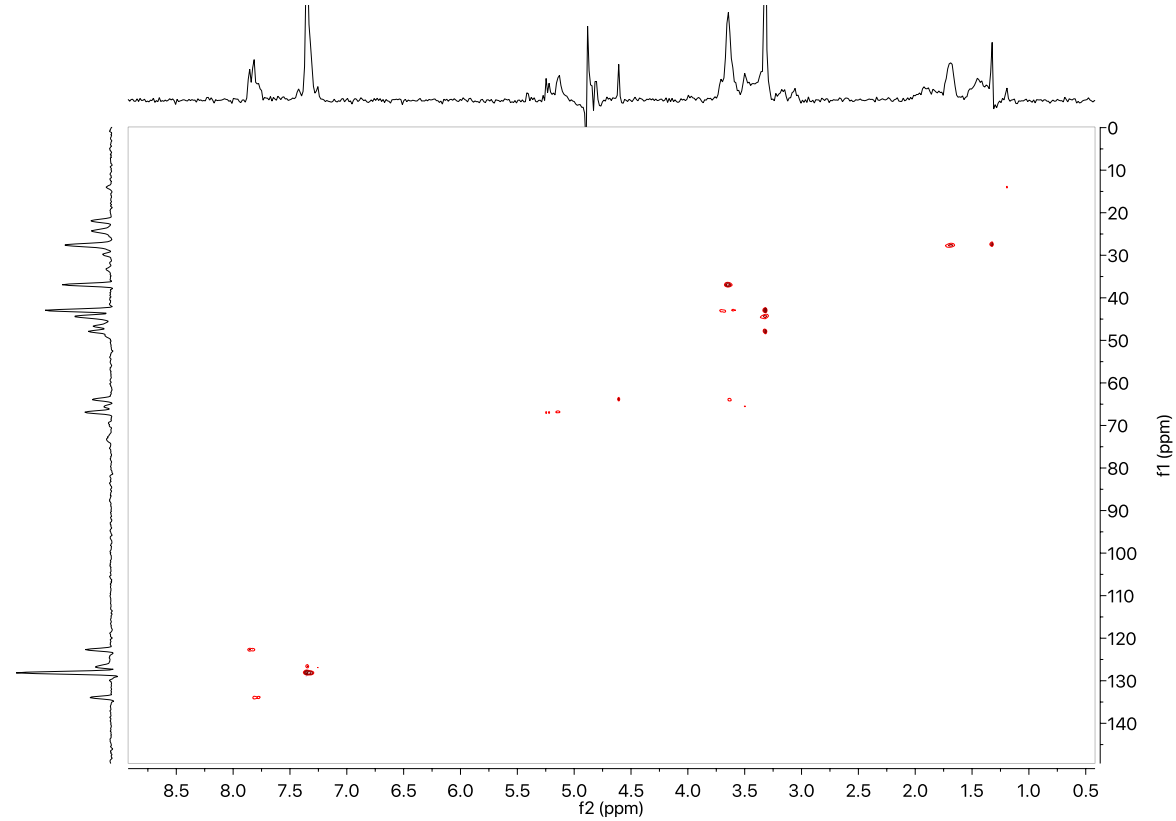

Figure A24: ^{1}H-^{13}C HSQC spectrum of **4.**

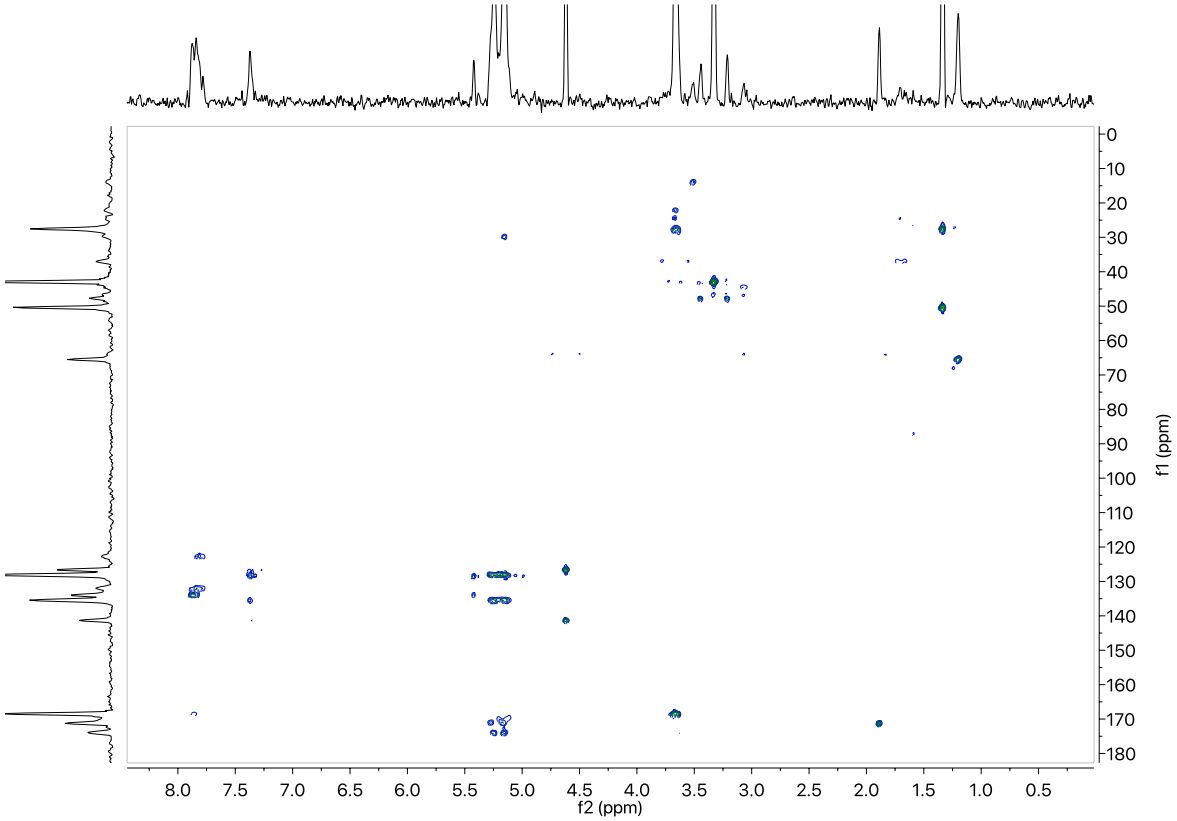

Figure A25: ^{1}H-^{13}C HMBC spectrum of **4.**

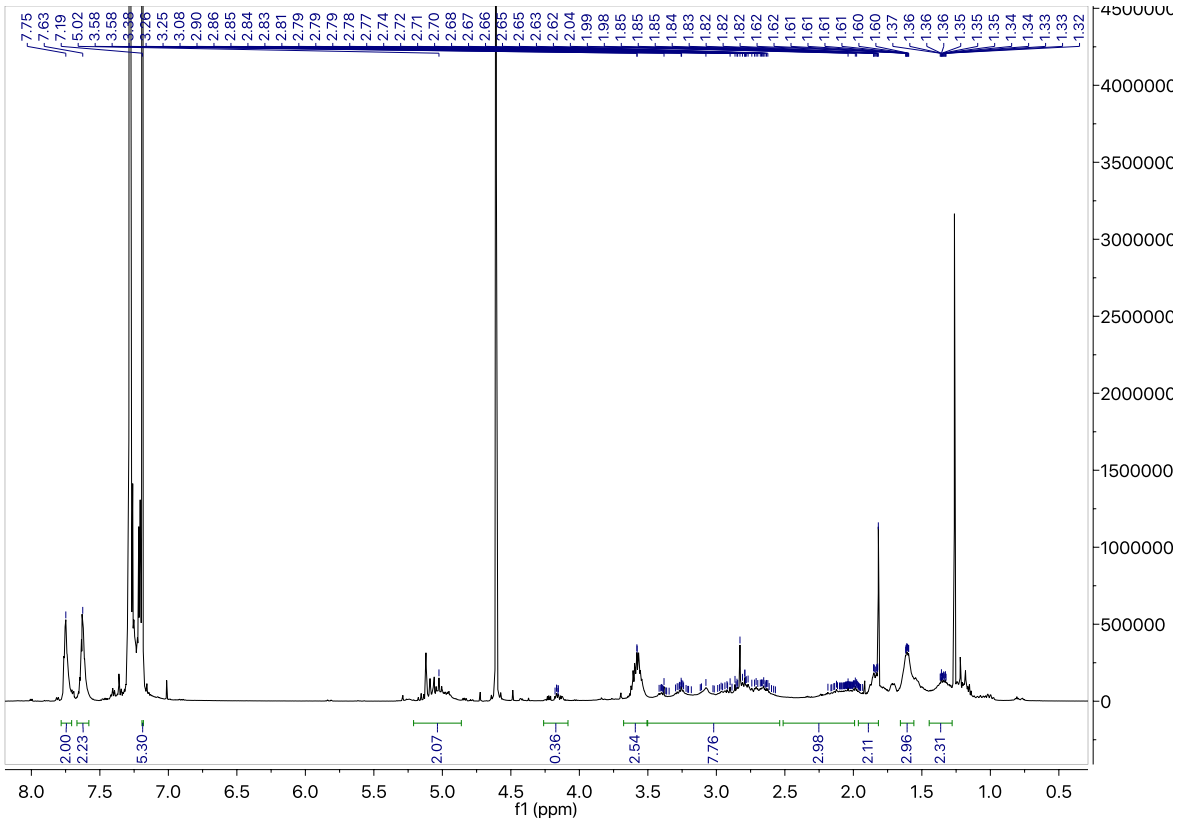

Figure A26: ^{1}H NMR spectrum of **5.**

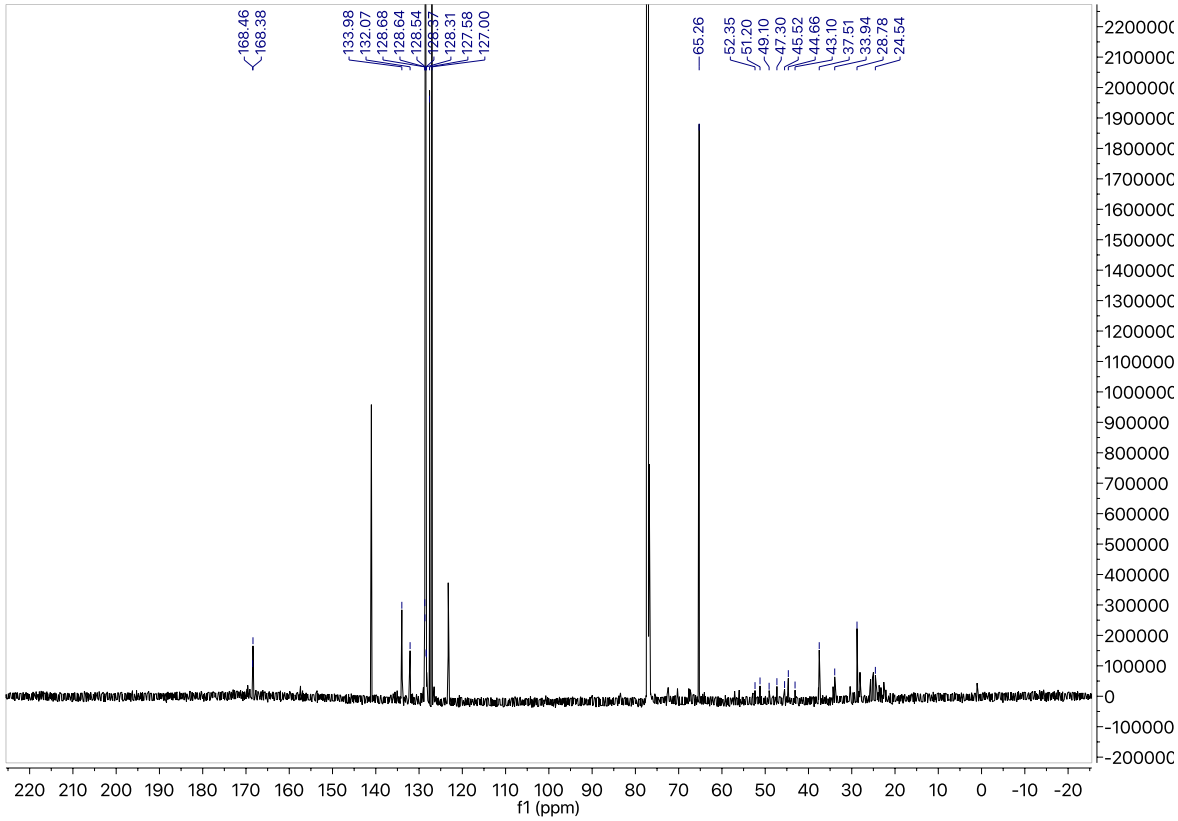

Figure A27: $^{13}C\{^{1}H\}$ NMR spectrum of **5.**

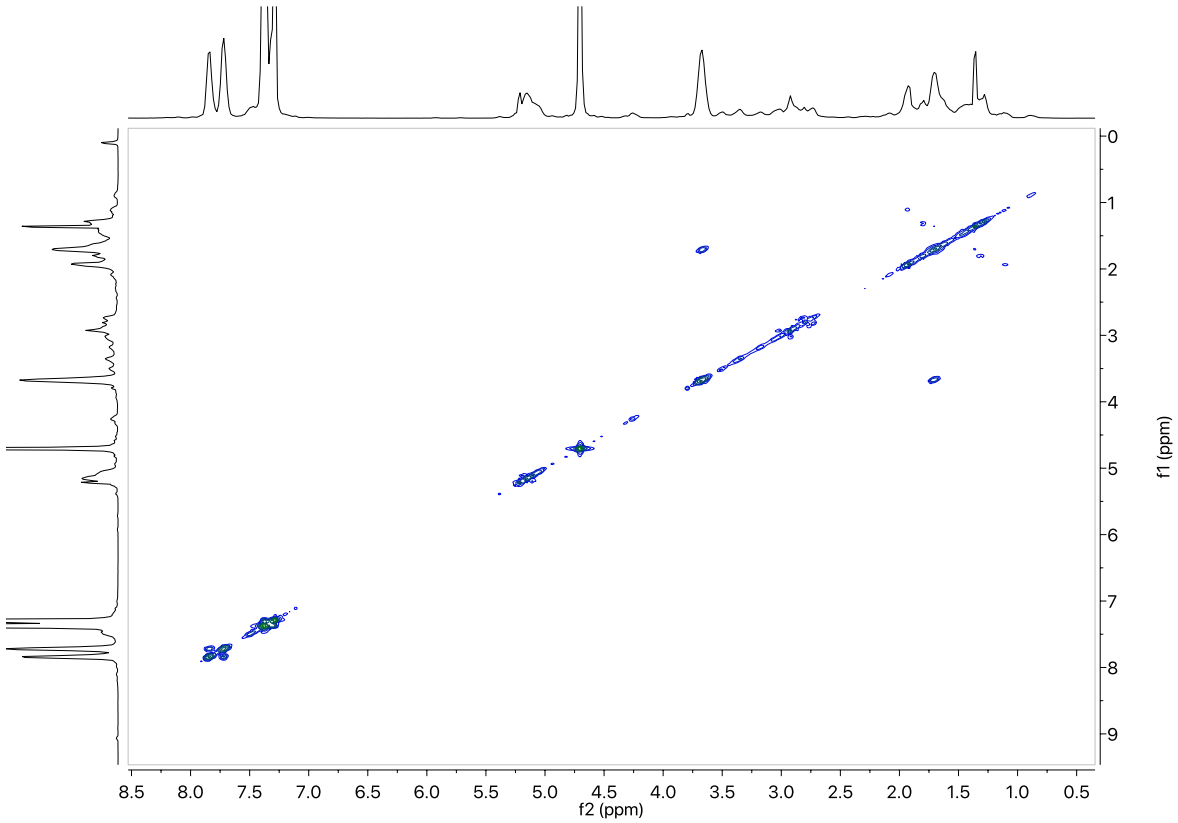

Figure A28: ^{1}H-^{1}H COSY spectrum of **5.**

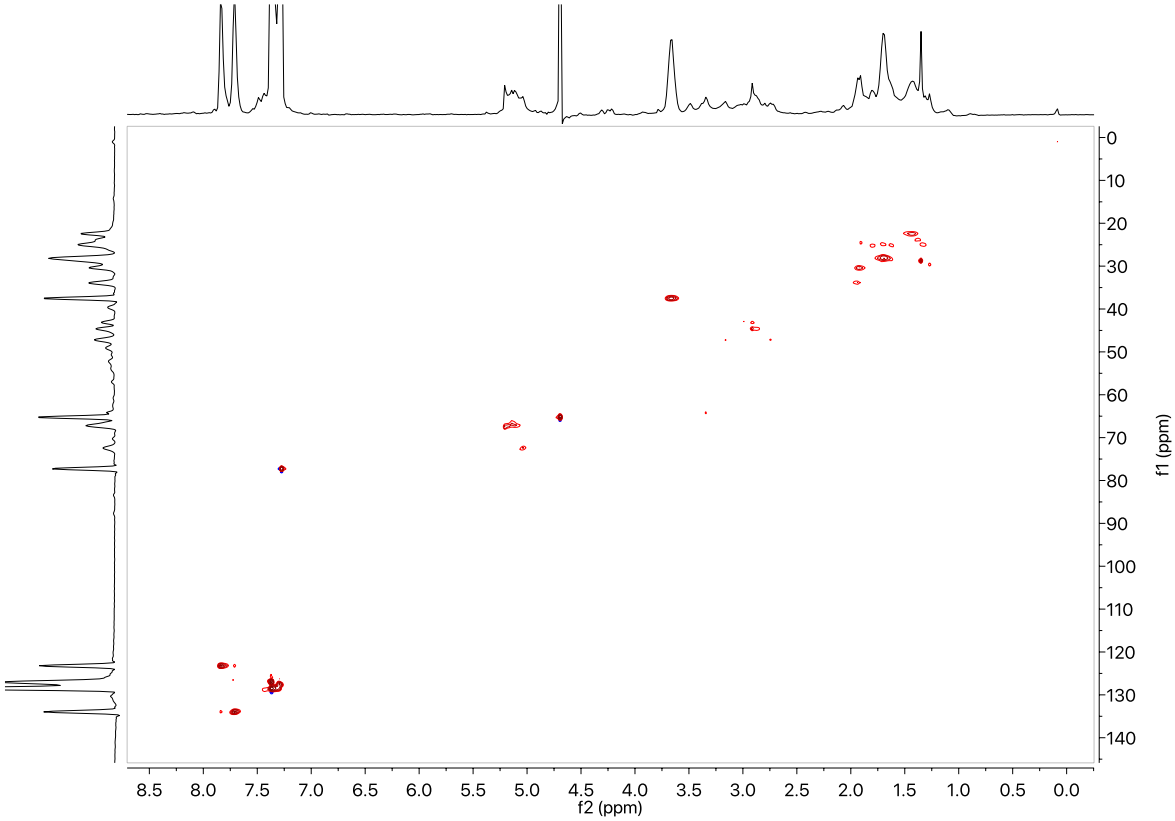

Figure A29: ^{1}H-^{13}C HSQC spectrum of **5.**

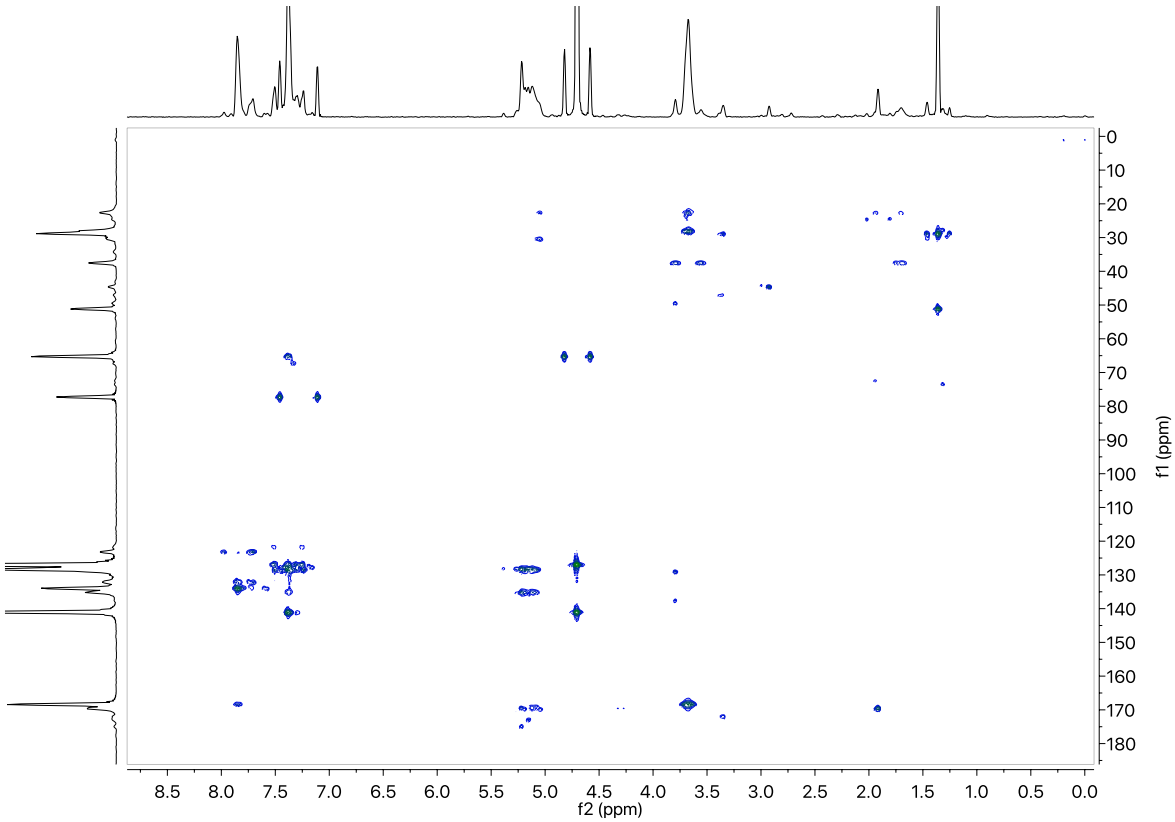

Figure A30: ^{1}H-^{13}C HMBC spectrum of **5.**

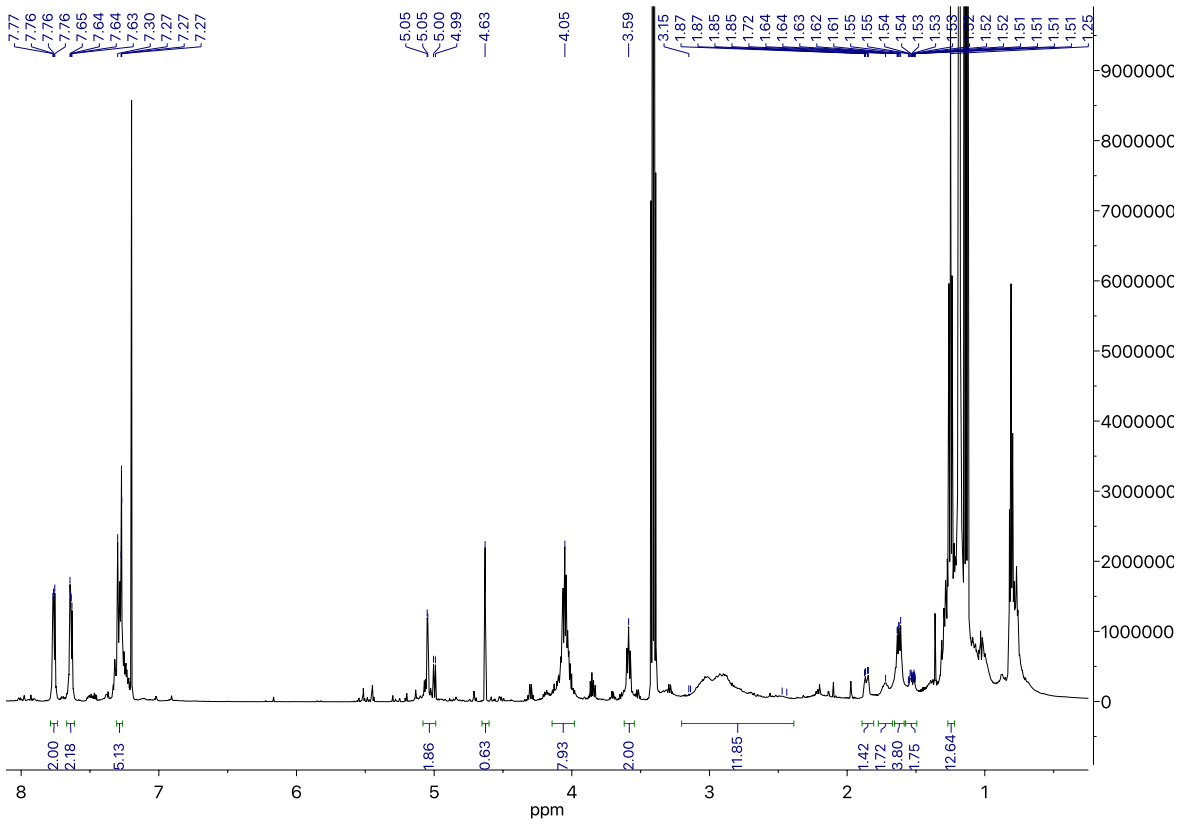

Figure A31: ^{1}H NMR spectrum of **6.**

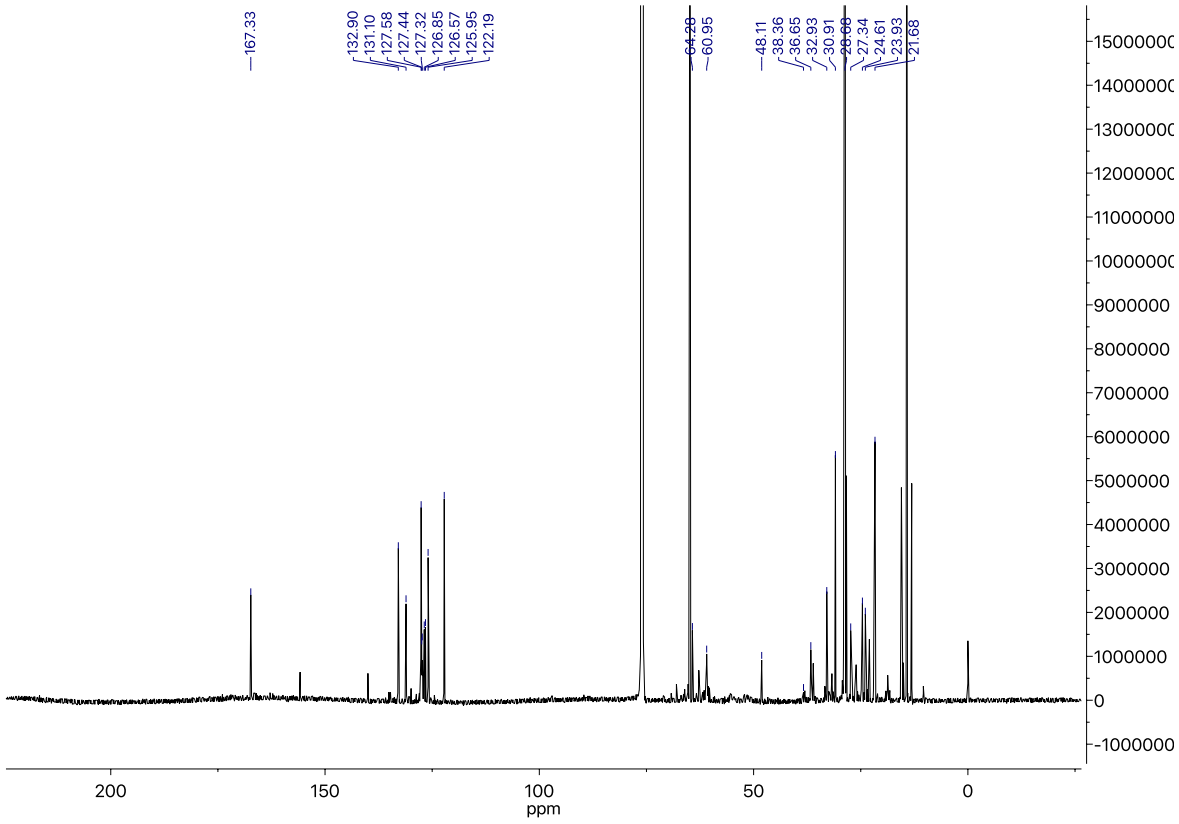

Figure A32: ^{13}C{^{1}H} NMR spectrum of **6.**

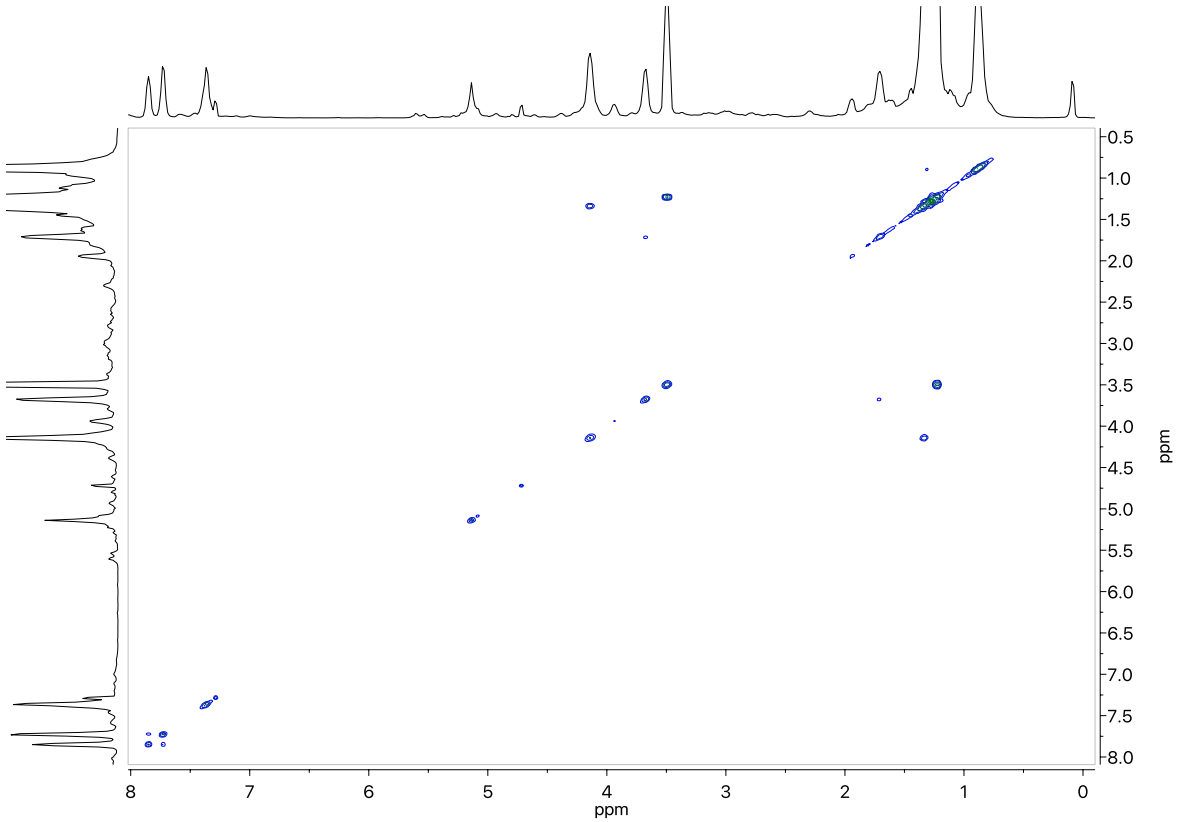

Figure A33: ^{1}H-^{1}H COSY spectrum of **6.**

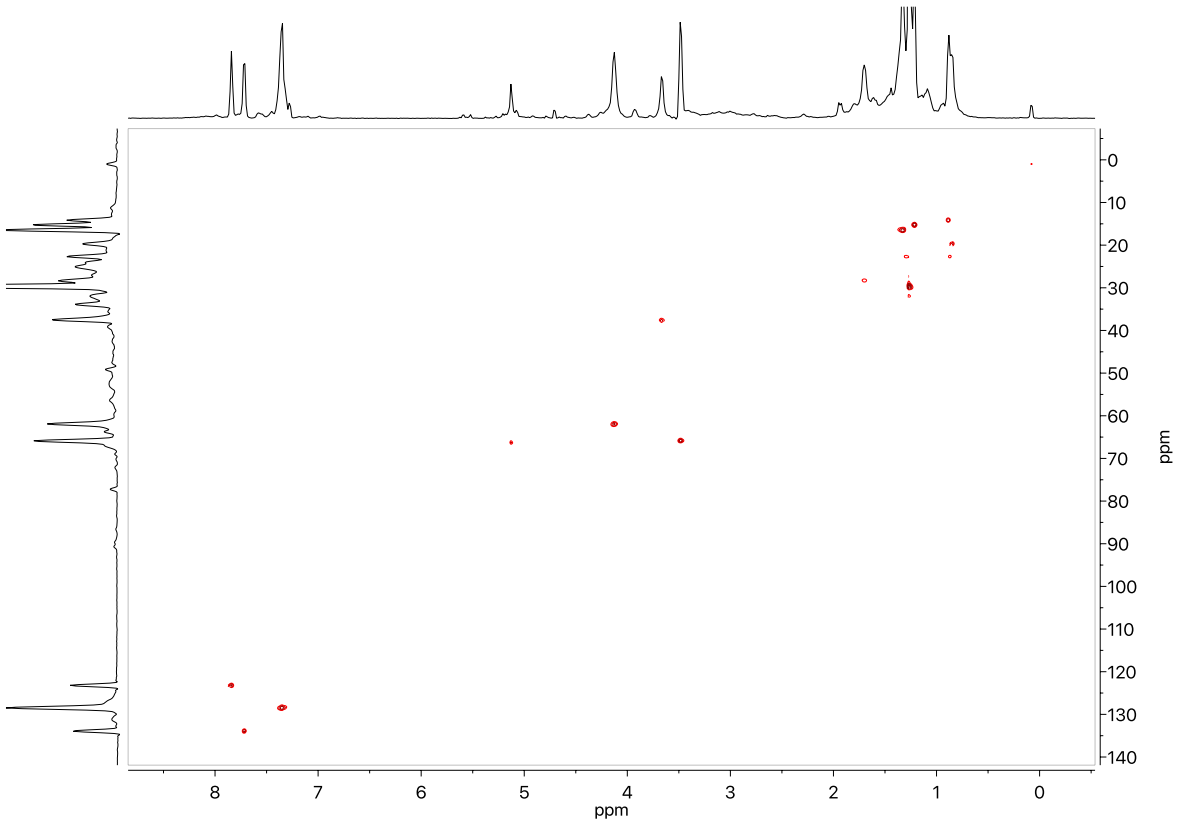

Figure A34: ^{1}H-^{13}C HSQC spectrum of **6.**

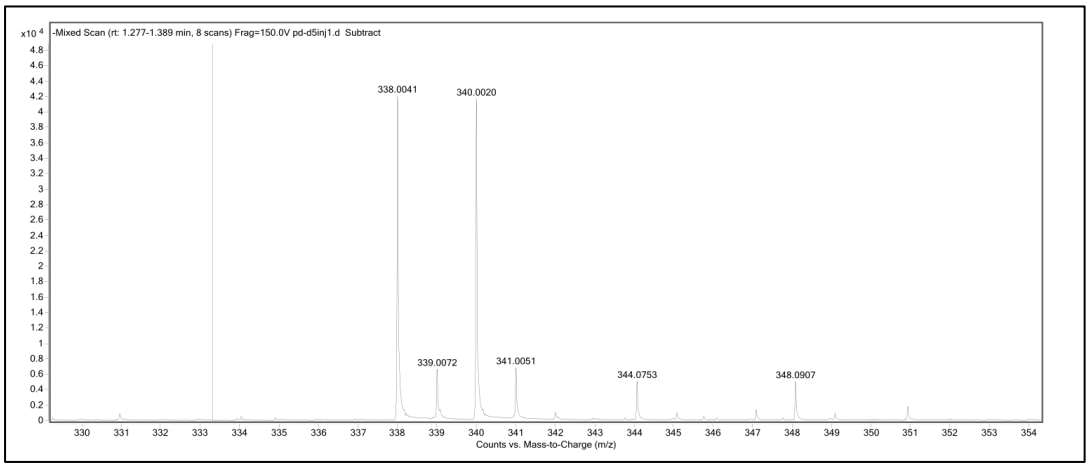

Figure A35: High-resolution ESI-MS of **1**.

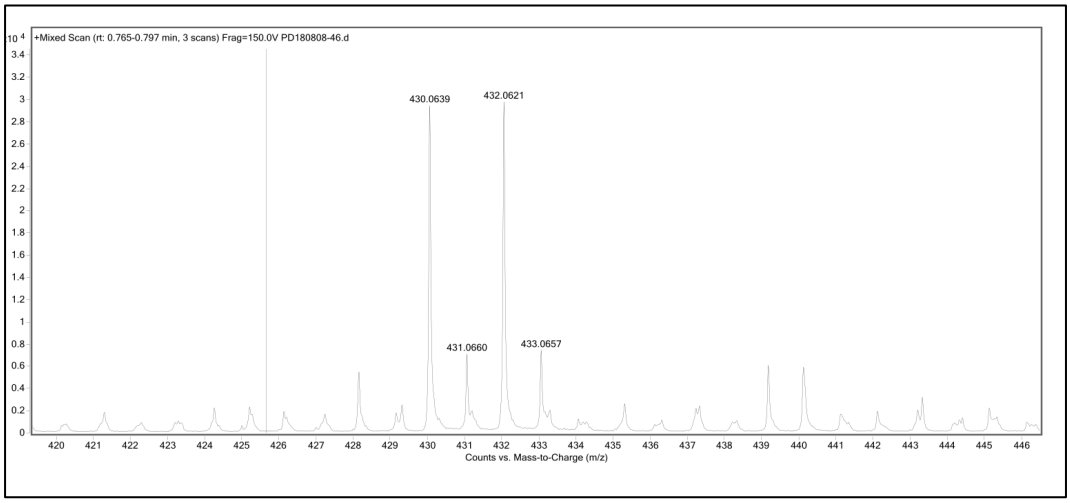

Figure A36: High-resolution ESI-MS of **2**.

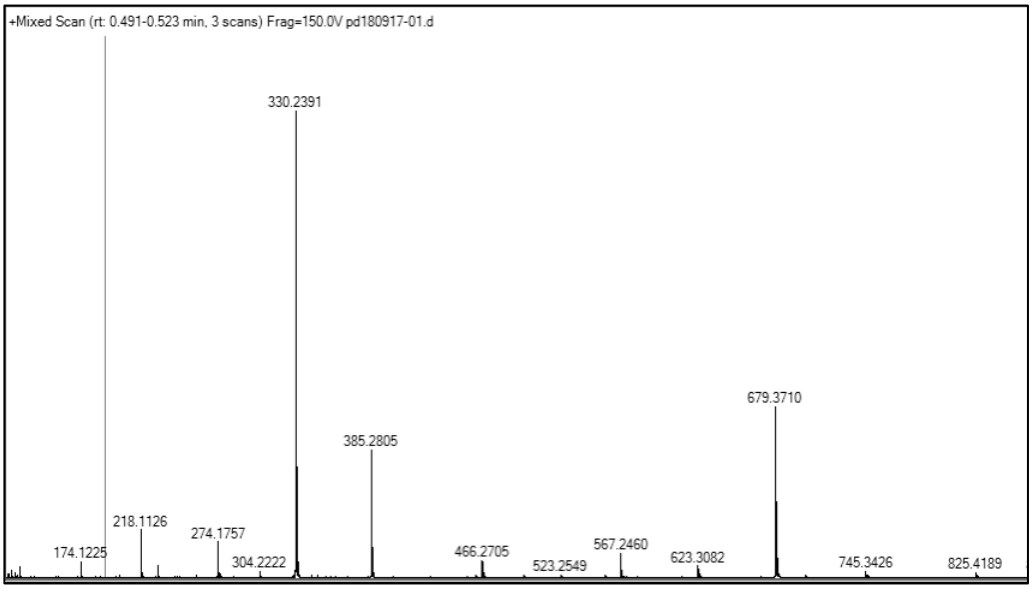

Figure A37: High-resolution ESI-MS of **3**.

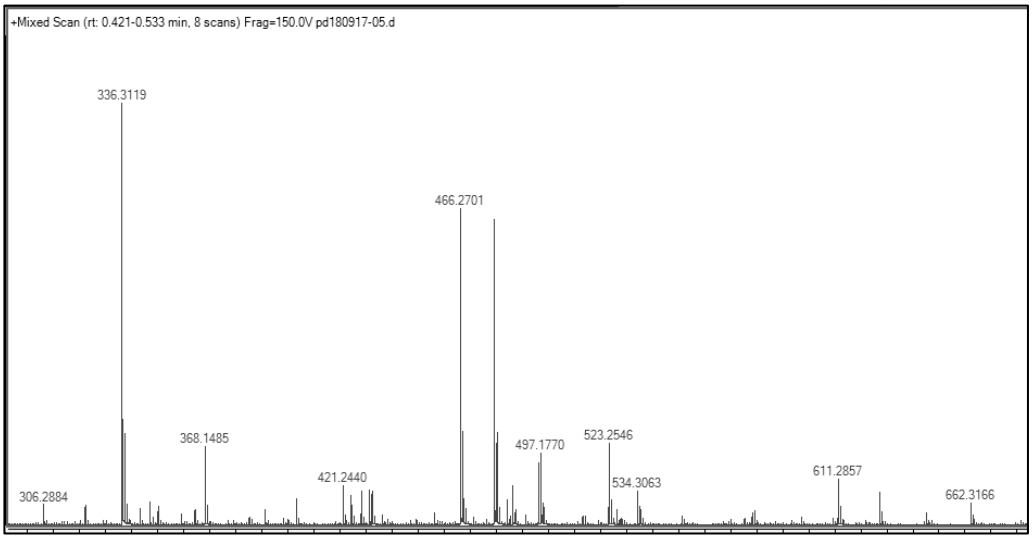

Figure A38: High-resolution ESI-MS of **4**.

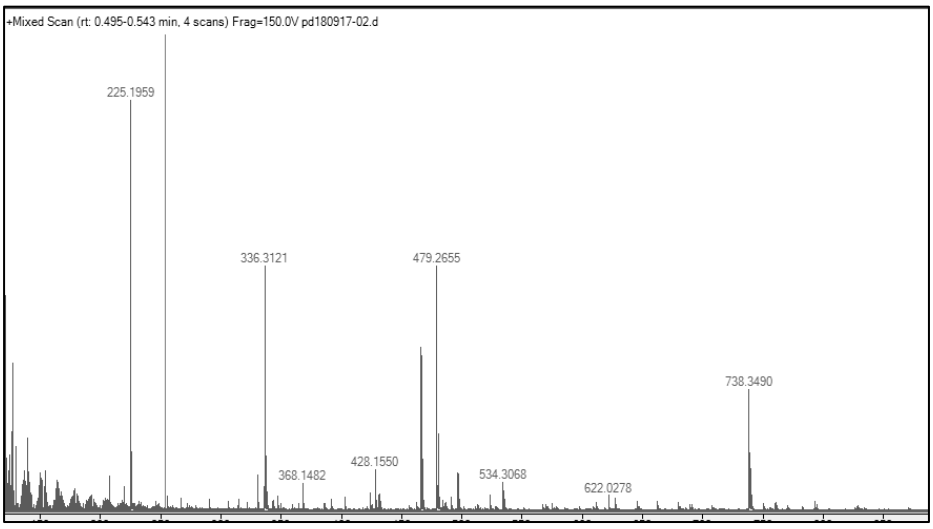

Figure A39: High-resolution ESI-MS of **5**.

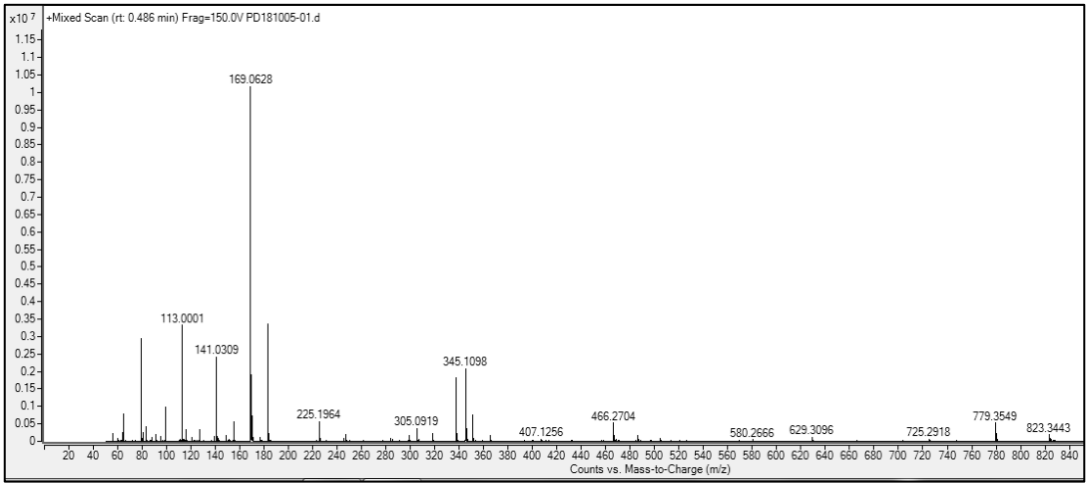

Figure A40: High-resolution ESI-MS of **6**.

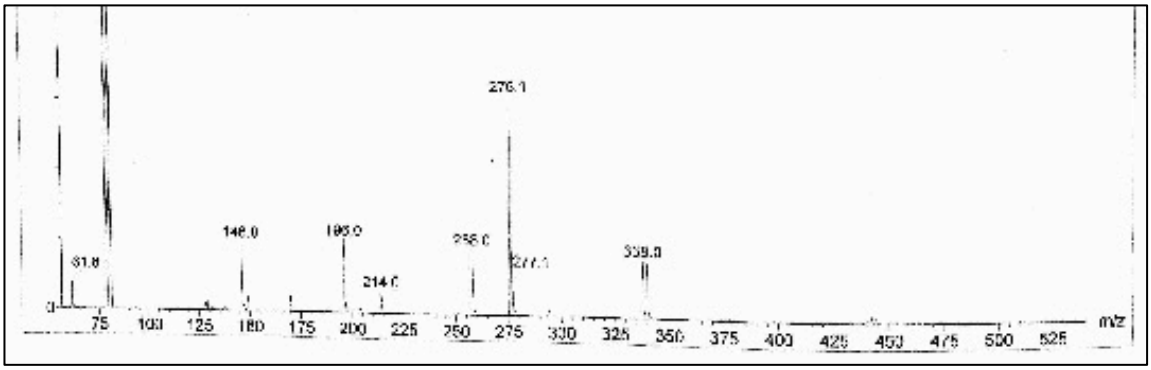

Figure A41: Low-resolution ESI-MS of **1**.

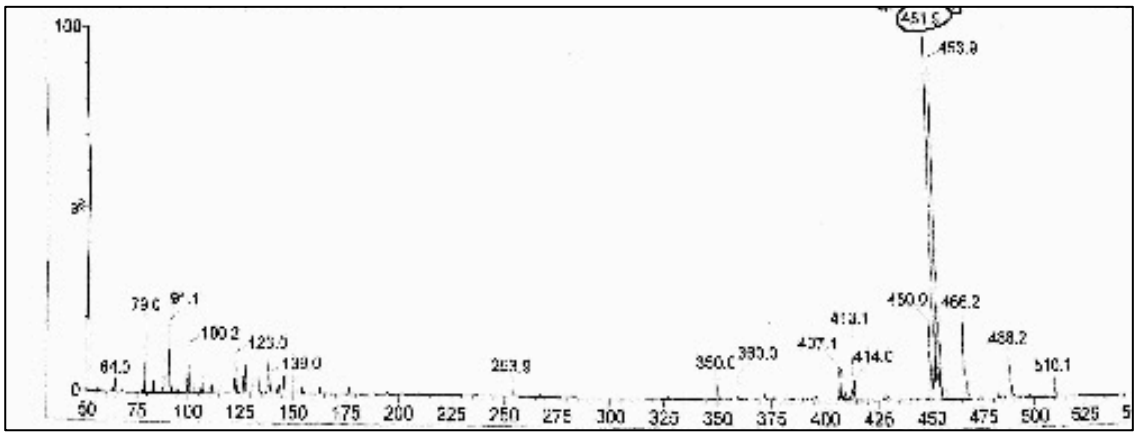

Figure A42: Low-resolution ESI-MS of **2**.

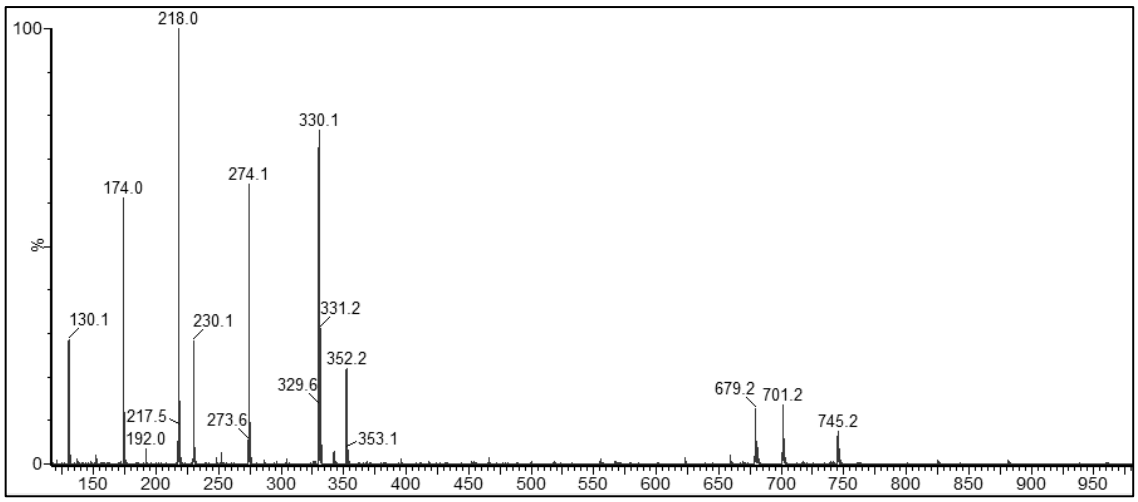

Figure A43: Low-resolution ESI-MS of **3**.

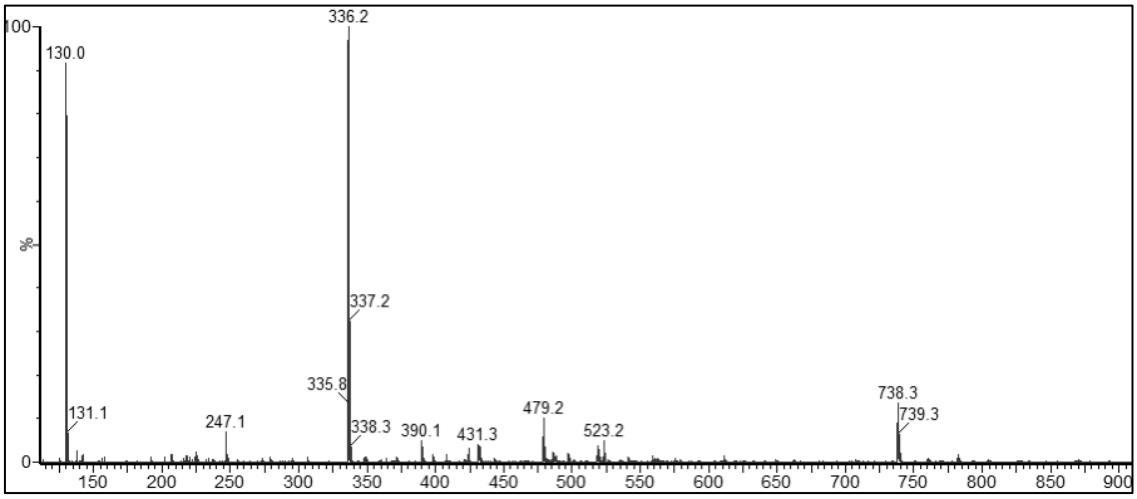

Figure A44: Low-resolution ESI-MS of **4**.

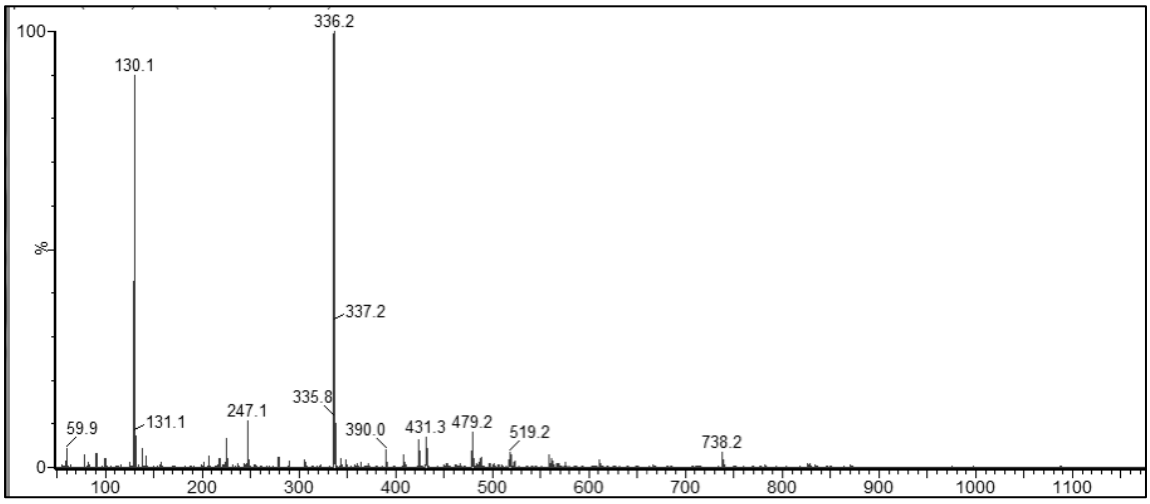

Figure A45: Low-resolution ESI-MS of **5**.

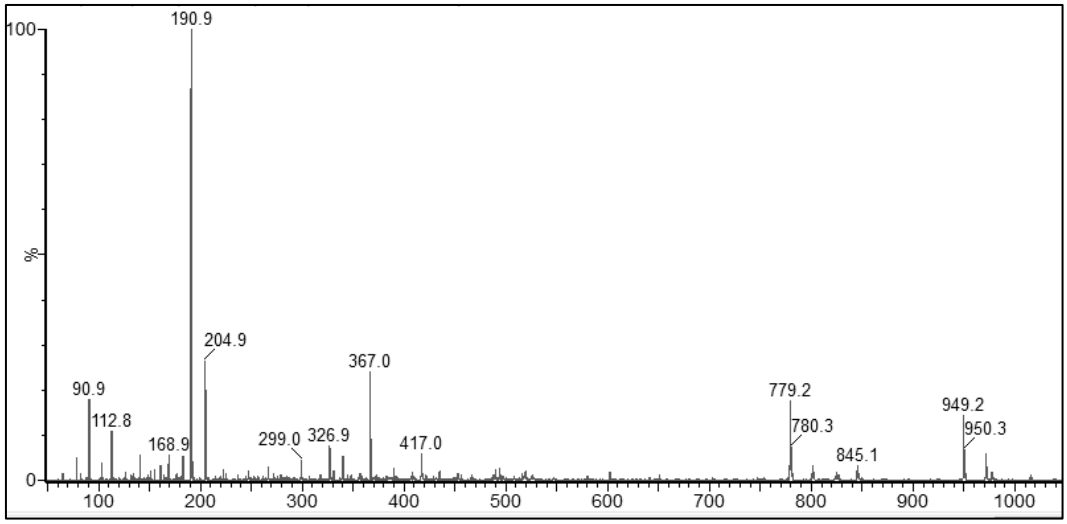

Figure A46: Low-resolution ESI-MS of **6**.

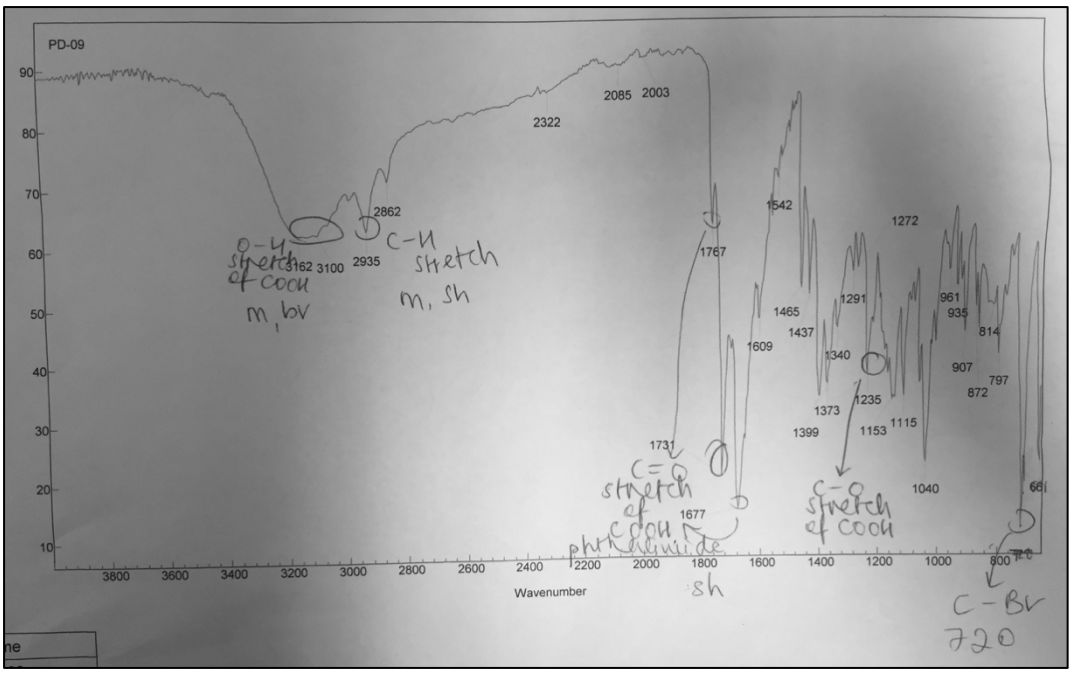

Figure A47: ATR-FTIR spectrum of **1**.

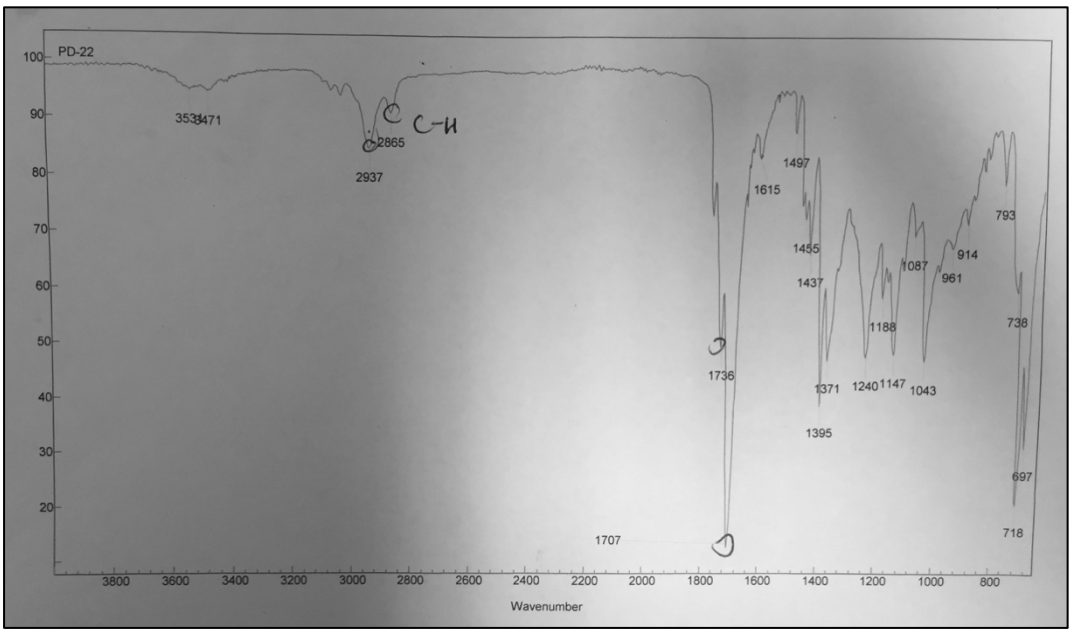

Figure A48: ATR-FTIR spectrum of **2.**

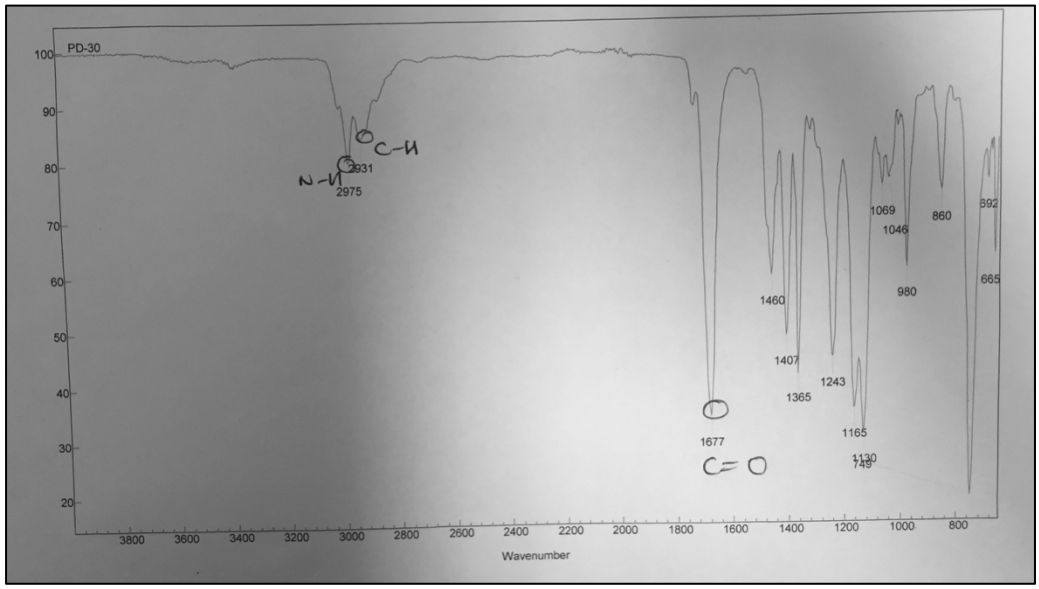

Figure A49: ATR-FTIR spectrum of diBocTACN.

Table A1: Atomic coordinates (x 10^4) and equivalent isotropic displacement parameters (Å^2 x 10^3) for [Ga(NOTP)]. U_{eq} is defined as one-third of the trace of the orthogonalised U_{ij} tensor.

	x	y	z	U_{eq}
Ga(1)	3321(1)	2422(1)	4757(1)	7(1)
P(1)	5864(1)	2457(1)	3799(1)	10(1)
P(2)	3161(1)	4371(1)	5744(1)	10(1)
P(3)	3048(1)	706(1)	6149(1)	9(1)
O(1)	5139(1)	1929(1)	4588(1)	11(1)
O(2)	6413(2)	1699(1)	3087(1)	18(1)
O(3)	7087(1)	3117(1)	4298(1)	16(1)
O(4)	4113(1)	3642(1)	5334(1)	11(1)
O(5)	2829(2)	5224(1)	4924(1)	17(1)
O(6)	3761(1)	4695(1)	6895(1)	14(1)
O(7)	3465(1)	1766(1)	6134(1)	10(1)
O(8)	1595(1)	630(1)	6514(1)	15(1)
O(9)	4205(1)	54(1)	6790(1)	13(1)
N(1)	2932(1)	2880(1)	3087(1)	9(1)
N(2)	1267(1)	3039(1)	4651(1)	9(1)
N(3)	2061(1)	1223(1)	4017(1)	9(1)
C(1)	1968(2)	3733(1)	3009(1)	11(1)
C(2)	738(2)	3537(1)	3575(1)	12(1)
C(3)	304(2)	2220(1)	4754(1)	11(1)
C(4)	485(2)	1416(1)	3975(1)	12(1)
C(5)	2322(2)	1129(1)	2904(1)	11(1)
C(6)	2175(2)	2103(1)	2338(1)	12(1)
C(7)	4384(2)	3145(1)	2911(1)	13(1)
C(8)	1466(2)	3707(1)	5596(1)	11(1)
C(9)	2625(2)	378(1)	4707(1)	12(1)

Table A2: Bond lengths (Å) for [Ga(NOTP)].

Ga(1)-O(1)	1.9106(11)	Ga(1)-N(2)	2.0968(13)
Ga(1)-O(4)	1.9291(11)	Ga(1)-N(3)	2.1300(13)
Ga(1)-O(7)	1.9390(11)	Ga(1)-N(1)	2.1451(13)
P(1)-O(3)	1.4898(13)	P(1)-O(1)	1.5305(12)
P(1)-O(2)	1.5574(13)	P(1)-O(7)	1.8326(17)
P(2)-O(6)	1.4928(12)	P(2)-O(4)	1.5309(12)
P(2)-O(5)	1.5578(13)	P(2)-O(8)	1.8196(17)
P(3)-O(9)	1.4962(12)	P(3)-O(7)	1.5331(12)
P(3)-O(8)	1.5566(13)	P(3)-C(9)	1.8228(17)
N(1)-C(1)	1.487(2)	N(1)-C(7)	1.489(2)
N(1)-C(6)	1.500(2)	N(2)-C(3)	1.487(2)
N(2)-C(8)	1.489(2)	N(2)-C(2)	1.496(2)
N(3)-C(9)	1.484(2)	N(3)-C(5)	1.491(2)
N(3)-C(4)	1.501(2)	C(1)-C(2)	1.532(2)
C(3)-C(4)	1.529(2)	C(5)-C(6)	1.526(2)

Table A3: Bond angles (°) for [Ga(NOTP)].

O(1)-Ga(1)-O(4)	94.83(5)	O(7)-Ga(1)-N(3)	85.94(5)
O(1)-Ga(1)-O(7)	93.69(5)	N(2)-Ga(1)-N(3)	83.53(5)
O(4)-Ga(1)-O(7)	98.29(5)	O(1)-Ga(1)-N(1)	86.43(5)
O(1)-Ga(1)-N(2)	169.79(5)	O(4)-Ga(1)-N(1)	93.62(5)
O(4)-Ga(1)-N(2)	85.86(5)	O(7)-Ga(1)-N(1)	168.03(5)
O(7)-Ga(1)-N(2)	96.30(5)	N(2)-Ga(1)-N(1)	83.36(5)
O(1)-Ga(1)-N(3)	95.07(5)	N(3)-Ga(1)-N(1)	82.13(5)
O(4)-Ga(1)-N(3)	168.95(5)	O(3)-P(1)-O(1)	116.61(7)
O(3)-P(1)-O(2)	109.23(7)	O(1)-P(1)-O(2)	108.42(7)
O(3)-P(1)-C(7)	109.16(7)	O(1)-P(1)-C(7)	104.66(7)
O(2)-P(1)-C(7)	108.44(8)	O(6)-P(2)-O(5)	112.31(7)
O(4)-P(2)-O(5)	108.82(7)	O(6)-P(2)-C(8)	111.47(7)
O(4)-P(2)-C(8)	101.71(7)	O(5)-P(2)-C(8)	107.13(8)
O(9)-P(3)-O(7)	116.01(7)	O(9)-P(3)-O(8)	112.28(7)
O(7)-P(3)-O(8)	108.51(7)	O(9)-P(3)-C(9)	109.67(7)
O(7)-P(3)-C(9)	102.91(7)	O(8)-P(3)-C(9)	106.69(8)
P(1)-O(1)-Ga(1)	117.34(7)	P(2)-O(4)-Ga(1)	120.59(7)
P(3)-O(7)-Ga(1)	120.40(7)	C(1)-N(1)-C(7)	111.30(13)
C(1)-N(1)-C(6)	110.44(12)	C(7)-N(1)-C(6)	113.50(13)
C(1)-N(1)-Ga(1)	104.86(9)	C(7)-N(1)-Ga(1)	106.31(9)
C(6)-N(1)-Ga(1)	110.00(10)	C(3)-N(2)-C(8)	111.73(12)
C(3)-N(2)-C(2)	111.25(12)	C(8)-N(2)-C(2)	112.53(13)
C(3)-N(2)-Ga(1)	104.78(9)	C(8)-N(2)-Ga(1)	105.98(9)
C(2)-N(2)-Ga(1)	110.14(9)	C(9)-N(3)-C(5)	111.27(12)
C(9)-N(3)-C(4)	111.87(12)	C(5)-N(3)-C(4)	112.10(12)
C(9)-N(3)-Ga(1)	106.71(9)	C(5)-N(3)-Ga(1)	106.13(9)
C(4)-N(3)-Ga(1)	108.42(9)	N(1)-C(1)-C(2)	110.45(13)
N(2)-C(2)-C(1)	112.62(13)	N(2)-C(3)-C(4)	109.86(13)
N(3)-C(4)-C(3)	112.16(13)	N(3)-C(5)-C(6)	110.17(13)
N(1)-C(6)-C(5)	112.09(13)	N(1)-C(7)-P(1)	111.74(11)
N(2)-C(8)-P(2)	109.50(10)	N(3)-C(9)-P(3)	110.10(11)

Table A4: Anisotropic displacement parameters ($Å^2$ x 10^3) for [Ga(NOTP)]. The anisotropic displacement factor exponent takes the form: $-2\pi^2(h^2 a^2 U11+ ... + 2hka^* b^2 U_{12})$.

	U_{11}	U_{22}	U_{33}	U_{23}	U_{13}	U_{12}
Ga(1)	7(1)	6(1)	7(1)	0(1)	2(1)	0(1)
P(1)	10(1)	7(1)	13(1)	-1(1)	5(1)	0(1)
P(2)	12(1)	7(1)	9(1)	-1(1)	2(1)	1(1)
P(3)	10(1)	7(1)	10(1)	1(1)	2(1)	-1(1)
O(1)	10(1)	10(1)	12(1)	1(1)	4(1)	2(1)
O(2)	28(1)	7(1)	24(1)	-2(1)	19(1)	-2(1)
O(3)	11(1)	10(1)	26(1)	-2(1)	4(1)	0(1)
O(4)	11(1)	8(1)	14(1)	-3(1)	3(1)	-2(1)
O(5)	28(1)	7(1)	13(1)	0(1)	1(1)	0(1)
O(6)	17(1)	12(1)	10(1)	-2(1)	2(1)	2(1)
O(7)	12(1)	8(1)	8(1)	0(1)	2(1)	-1(1)
O(8)	12(1)	17(1)	15(1)	8(1)	4(1)	0(1)
O(9)	14(1)	8(1)	15(1)	0(1)	0(1)	0(1)
N(1)	9(1)	9(1)	9(1)	0(1)	2(1)	-1(1)
N(2)	9(1)	9(1)	9(1)	0(1)	2(1)	1(1)
N(3)	10(1)	9(1)	9(1)	0(1)	2(1)	0(1)
C(1)	13(1)	10(1)	10(1)	2(1)	1(1)	2(1)
C(2)	11(1)	12(1)	10(1)	2(1)	0(1)	2(1)
C(3)	8(1)	12(1)	15(1)	1(1)	4(1)	-1(1)
C(4)	8(1)	13(1)	15(1)	-2(1)	2(1)	-2(1)
C(5)	14(1)	11(1)	9(1)	-3(1)	3(1)	-1(1)
C(6)	15(1)	12(1)	9(1)	-2(1)	2(1)	-2(1)
C(7)	12(1)	14(1)	13(1)	3(1)	5(1)	-2(1)
C(8)	12(1)	11(1)	11(1)	-2(1)	4(1)	2(1)
C(9)	15(1)	8(1)	12(1)	-1(1)	2(1)	-1(1)

Table A5: Hydrogen coordinates (x 10^4) and isotropic displacement parameters ($Å^2$ x 10^3) for [Ga(NOTP)].

	x	y	z	U_{eq}
H(1A)	1543	3891	2230	14
H(1B)	2550	4289	3359	14
H(2A)	279	4152	3693	14
H(2B)	-18	3137	3090	14
H(3A)	-727	2434	4576	14
H(3B)	560	1980	5516	14
H(4A)	31	825	4169	15
H(4B)	-33	1594	3218	15
H(5A)	1605	676	2463	14
H(5B)	3314	869	2963	14
H(6A)	2596	2066	1694	14
H(6B)	1126	2265	2073	14
H(7A)	4558	3837	3060	15
H(7B)	4382	3027	2137	15
H(8A)	1497	3341	6273	14
H(8B)	632	4158	5477	14
H(9A)	3517	135	4519	14
H(9B)	1884	-138	4563	14
H(2)	6180(30)	1150(20)	3150(20)	43(8)
H(5)	2840(30)	5710(20)	5160(30)	55(10)
H(8)	1610(30)	360(20)	7060(30)	47(9)